UNIVERSITÀ DELLA CALABRIA
Dipartimento di FISICA

UNIVERSITÀ DELLA CALABRIA
FACOLTÁ DI SCIENZE MM. FF. NN.
—
DEPTARTMENT OF PHYSICS
ASTRONOMY AND ASTOPHYSICS, FIS/05 —
PHD IN PHYSICS
CYCLE XXIII

TURBULENCE AND STRUCTURES IN PLASMA ASTROPHYSICS

Prof. GIOVANNI FALCONE, Course Coordinator
Prof. VINCENZO CARBONE, Candidate's Supervisor

Vincenzo Carbone

Ph.D. Candidate: SANDRO DONATO

Sandro Donato

December, 2011

UNIVERSITÀ DELLA CALABRIA
Dipartimento di FISICA

Universitá della Calabria
Facoltá di Scienze MM. FF. NN.
—
Department of Physics
Astronomy and Astophysics, FIS/05 —
PhD in Physics
Cycle XXIII

TURBULENCE AND STRUCTURES IN PLASMA ASTROPHYSICS

Prof. Giovanni Falcone, Course Coordinator
Prof. Vincenzo Carbone, Candidate's Supervisor

Ph.D. Candidate: Sandro Donato

December, 2011

"To our Flower"

Contents

1 General overview of Turbulence **1**
1.1 Fluid Turbulence - Brief history and introduction 1
1.2 Plasma Turbulence 6
1.2.1 Kinetic plasma theory 8
1.2.2 Fluid plasma theories 10
1.2.3 Plasma instabilities and turbulence 13

2 Turbulence in Solar Wind **17**
2.1 The Solar Wind plasma laboratory 17
2.2 In situ plasma turbulence - The STEREO mission and the S/Waves experiment 19
2.2.1 Plasma waves measurements with STEREO 22
2.3 Observations of Langmuir ponderomotive effects 25
2.4 Electrostatic activity in the high–frequency range of solar wind turbulence 29
2.4.1 STEREO WAVES data 32
2.4.2 Hybrid-Vlasov simulations data 33
2.4.3 Conclusions 35

3 Magnetic Reconnection as an element of Turbulence **39**
3.1 The physics of magnetic reconnection 40
3.1.1 Magnetic reconnection : equations and the Sweet–Parker model 42
3.2 Overview on 2D MHD turbulence 45
3.2.1 Local reconnection in turbulence 48
3.2.2 The link between magnetic reconnection and turbulence . . . 52
3.3 Time behavior of reconnection in turbulence 54
3.4 The Hall effect in the reconnection process in turbulence 57
3.4.1 Overview of numerical simulations in HMHD turbulence . . . 57
3.4.2 Reconnection in turbulence: Hall MHD *vs.* MHD 59
3.5 Generalized Sweet–Parker theory for magnetic reconnection 66
3.6 Conclusions 67

Conclusions **71**

Appendices **75**

A Using the STEREO spacecraft as a density probe **77**
A.1 Floating potential of spacecraft and antennas 77
A.2 Equilibrium potential 78
A.3 Charging time scales 79
A.4 Variations of spacecraft potential associated to density fluctuations . 81

B A simple Van der Pol model **83**

Bibliography **87**

Turbulence and structures in plasma Astrophysics

Keywords:
turbulence, non–linear phenomena, plasma waves, magnetic reconnection.

List of Figures

1.1 Examples of turbulent flows 2
1.2 L. da Vinci sketch of "turbolenza" 3
1.3 Reynolds experiment 4

2.1 Solar Wind cartoon 18
2.2 STEREO spacecraft, Sun view 20
2.3 STEREO, instruments view 21
2.4 S/Waves waveforms 22
2.5 Langmuir waves instability scheme 24
2.6 Langmuir nucleation cycle 26
2.7 Langmuir energy ratio *vs* density fluctuations level 28
2.8 Saturation of density fluctuations level 29
2.9 Photoelectron temperature calibration 30
2.10 Magnetic spectra in solar wind 31
2.11 STEREO electrostatic waveform 32
2.12 Oscillation regimes observed in STEREO wavepackets 33
2.13 Hybrid–Vlasov $k-\omega$ spectra 35
2.14 Hybrid–Vlasov waveform 36
2.15 Oscillation regimes observed in Hybrid–Vlasov simulations 37

3.1 Examples of reconnection in Solar system plasma 40
3.2 Frozen–in condition scheme 43
3.3 Frozen–in violation scheme 43
3.4 2D magnetic reconnection scheme 44
3.5 Sweet–Parker model 45
3.6 Power spectra of magnetic fied. 47
3.7 Current shaded contour and magnetic potential line contour 47
3.8 Current density profile 48
3.9 Current density probability density function 49
3.10 magnetic field critical points 50
3.11 Reconnection rate probability distribution function 51
3.12 Aspect ratio of the diffusion regions 52
3.13 Current density and magnetic field profiles 53
3.14 Distibution of typical size of the diffusion regions 53
3.15 Shaded contour of the current density at different times 55
3.16 Probability density function of current densities at different times . . 56
3.17 Aspect ratio of diffusion regions at different times 56
3.18 Power spectra of magnetic fied for different values of the Hall parameter 59
3.19 Current density profiles for different values of the Hall parameter . . 60
3.20 PDF of currents varying the Hall parameter 60

3.21 Magnetic field critical points 61
3.22 Current density bifurcation and magnetic quadrupole 61
3.23 PDF of reconnection rates 63
3.24 Current density and magnetic field profiles in HMHD 64
3.25 Aspect ratio of diffusion regions changing the Hall parameter 64
3.26 Typical dimension of the diffusion regions changing the Hall parameter 65
3.27 Computed reconnection rate *vs* Sweet–parker expected reconnection rate for different times 67
3.28 Computed reconnection rate *vs* Sweet–parker expected reconnection rate for values of Hall parameter 68

A.1 Frequency range of calibration to detect density fluctuations 81
A.2 Density fluctuations as function of solar wind parameters 82

B.1 Oscillation regimes observed in Van der Pol simulations 85

Chapter 1

General overview of Turbulence

The understanding of turbulent behavior is one of the most intriguing, frustrating and important, problem in physics. The problem of turbulence has been studied by many of the greatest physicists and engineers of the 19^{th} and 20^{th} Centuries, and yet we do not understand in complete detail how or why turbulence occurs, nor can we predict turbulent behavior with any degree of reliability, even in very simple flow situations. First of all, there is no consensus on what is the problem of turbulence, neither is there an agreement on what are the goals of turbulence research and theories and what would constitute its solution. Therefore lots of formalisms are avoided, since the methods mostly brought in from linear analysis (such as various decompositions, perturbation methods, etc.) failed, and genuinely nonlinear analytic methods applicable to turbulence mostly do not exist. Anymore, the existing theoretical material is rather complicated and extremely large in scope. Many existing books are overloaded with technical details, the unprepared reader is totally lost in the enormous ocean of existing references. It seems that in turbulence there are more of questions than '"solutions". For those reasons, the subject of turbulence remains and probably will remain as the most exciting one for the mind of researchers in a really enormous variety of fields. It is a fact that most fluid flows are turbulent, and at the same time flow occur, and in many cases represent the dominant physics, on all macroscopic scales throughout the known universe, from the interior of biological cells, to circulatory and respiratory systems of living creatures, to countless technological devices and household appliances of modern society, to geophysical and astrophysical phenomena including planetary interiors, oceans and atmospheres and stellar physics, and finally to galactic and even supergalactic scales (in Fig. 1.1 two examples of turbulent flows). Thus, study of turbulence is motivated both by its inherent intellectual challenge and by the practical utility of a thorough understanding of its nature.

Trying to give a definition (even if there is not a precise definition), we can say that turbulence is a state of a physical system with many interacting degrees of freedom deviated far from equilibrium. This state looks irregular and chaotic both in time and in space.

1.1 Fluid Turbulence - Brief history and introduction

We experience turbulence everyday, in fact, wherever fluids are set into motion, and the velocity is high enough, turbulence tends to develop. The boundary layers and the wakes around and after bluff bodies such as cars, aeroplanes and buildings are

Figure 1.1: Turbulence in terrestrial (left) and jovian atmosphere (right)

turbulent. Also the flow and combustion in engines, both in piston engines and gas turbines and combustors, are highly turbulent. Air movements in rooms are also turbulent, at least along the walls where wall-jets are formed. Hence, when we compute fluid flow it will most likely be turbulent. It is interesting to recognize the fact that, when we take a picture of a turbulent flow at a given time, we see the presence of a lot of different turbulent structures of all sizes which are actively present during the motion. The presence of these structures was well recognized long time ago (XV-th century) by L. da Vinci, that termed such phenomena *"turbolenza"* and in Fig. 1.2 it can be seen the beautiful pictures of *vortices* observed and reproduced by him (figure from (11)). When we look at a flow at two different times, we can observe that the general aspect of the flow has not changed appreciably, say vortices are present all the time but the flow in each single point of the fluid looks different. We recognize that the gross features of the flow are reproducible but details are not predictable.

Turbulence became an experimental science since O. Reynolds who, at the end of XIX-th century (5), observed and investigated experimentally the transition from laminar to turbulent flow. He noticed that the flow inside a pipe becomes turbulent every time a single parameter, a combination of the viscosity coefficient η, a characteristic velocity U , and length L, would increase. This parameter $Re = UL/\eta$ is now called the *Reynolds number* that completely characterizes flow behavior in this situation. At lower Re (Fig. 1.3(a))the flow is regular (that is the motion is laminar), but when Re increases beyond a certain threshold, the flow becomes turbulent (Fig. 1.3(c)). As Re increases, the transition from a laminar to a turbulent state occurs over a range of values of Re with different characteristics and depending on the details of the experiment. In the limit $Re \to \infty$ the turbulence is said to be in a fully developed turbulent state. Fig. 1.3 provides the original sketch of three flow regimes identified in the Reynolds experiments as Re is varied.

The analytical description of turbulence was born with the Navier–Stokes (NS) equations, which are now almost universally believed to embody the physics of all

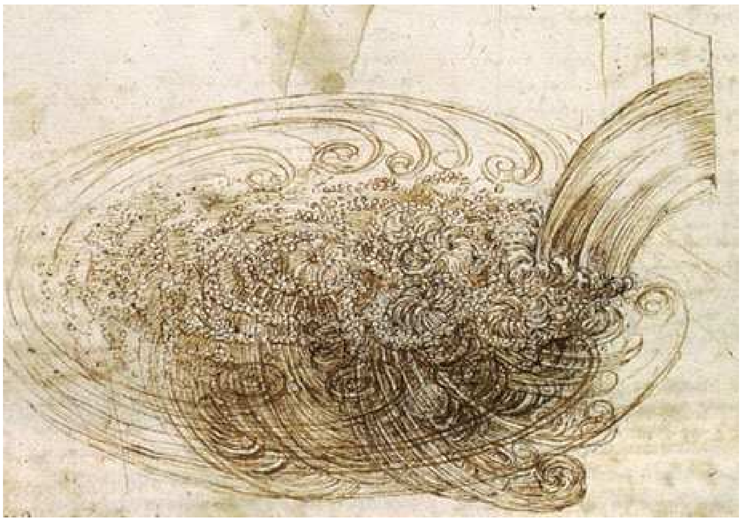

Figure 1.2: L. da Vinci sketch of “turbolenza“

fluid flows, including turbulent ones. They are nothing but the momentum equation based on Newton’s second law, which relates the acceleration of a fluid particle to the resulting volume and body forces acting on it. These equations have been introduced by L. Euler, however, the main contribution by C. Navier was to add a friction forcing term due to the interactions between fluid layers which move with different speed. This term results to be proportional to the viscosity coefficients η and ξ and to the variation of speed. By defining the velocity field $u(r,t)$ the kinetic pressure p and the density ρ, the equations describing a fluid flow are the continuity equation to describe the conservation of mass

$$\frac{\partial \rho}{\partial t} + (\boldsymbol{u} \cdot \nabla)\rho = -\rho(\nabla \cdot \boldsymbol{u}) \tag{1.1}$$

the equation for the conservation of momentum

$$\rho\frac{\partial \boldsymbol{u}}{\partial t} + (\boldsymbol{u} \cdot \nabla)\boldsymbol{u} = -\nabla P + \eta\nabla^2\boldsymbol{u} + (\eta + \frac{\xi}{3})\nabla(\nabla \cdot \boldsymbol{u}) \tag{1.2}$$

and an equation for the conservation of energy

$$\rho T\left[\frac{\partial s}{\partial t} + (\boldsymbol{u} \cdot \nabla)s\right] = \nabla(\chi\nabla T) + \frac{\eta}{2}\left(\frac{\partial u_i}{\partial x_k} + \frac{\partial u_k}{\partial x_i} + \frac{2}{3}\delta_{ik}\nabla \cdot \boldsymbol{u}\right)^2 + \xi(\nabla \cdot \boldsymbol{u})^2 \tag{1.3}$$

where s is the entropy per mass unit, T is the temperature, and χ is the coefficient of thermoconduction. An equation of state closes the system of fluid equations.

These equations are nonlinear and difficult to solve. As is well known, there are few exact solutions, and all of these have been obtained at the expense of introducing simplifying, often physically unrealistic, assumptions. Thus, little progress in the understanding of turbulence can be obtained via analytical solutions to these

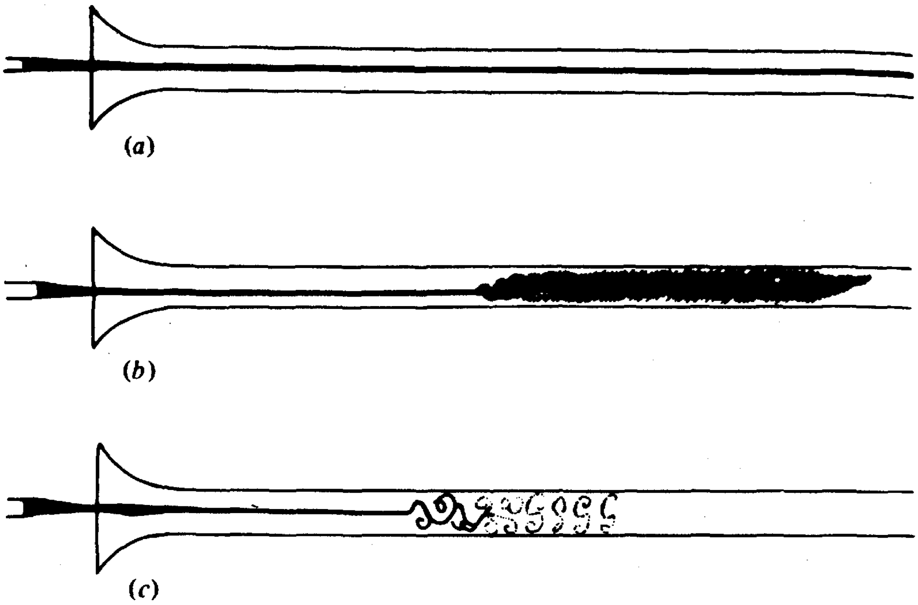

Figure 1.3: The original pictures by O. Reynolds which show the transition to a turbulent state of a flow in a pipe, as the Reynolds number increases from top to bottom

equations, and as a consequence early descriptions of turbulence were based mainly on experimental observations. The above equations considerably simplify if we consider the tractable incompressible fluid, where ρ = const., so that we obtain from the the Navier–Stokes momentum equation

$$\frac{\partial \boldsymbol{u}}{\partial t} + (\boldsymbol{u} \cdot \nabla)\boldsymbol{u} = -\left(\frac{\nabla p}{\rho}\right) + \nu \nabla^2 \boldsymbol{u} \tag{1.4}$$

where the coefficient $\nu = \eta/\rho$ is the kinematic viscosity. The incompressibility of the flow translates in a condition on the velocity field, namely the field is divergence–free, i.e., $\nabla \cdot \boldsymbol{u} = 0$. The non–linear term in equations represents the convective derivative. Of course, we can add on the right hand side of this equation all external forces, which eventually act on the fluid parcel. It is usual to describe the NS equations in a dimensionless form, to this purpose there can be defined: the velocity scale U and the length scale L to define dimensionless independent variables, namely $\mathbf{r} = \mathbf{r}^{'} L$ (from which $\nabla = \nabla^{'}/L$) and $t = t^{'}(L/U)$, and dependent variables $\boldsymbol{u} = \boldsymbol{u}^{'} U$ and $p = p^{'} U^2 \rho$. Then, using these variables in Eq.(1.4), we obtain

$$\frac{\partial \boldsymbol{u}^{'}}{\partial t^{'}} + (\boldsymbol{u}^{'} \cdot \nabla^{'})\boldsymbol{u}^{'} = -(\nabla p^{'}) + Re^{-1} \nabla^{'2} \boldsymbol{u}^{'} \tag{1.5}$$

The Reynolds number $Re = UL/\nu$ is evidently the only parameter of the fluid flow. This defines a Reynolds number similarity for fluid flows, namely fluids with the same value of the Reynolds number behaves in the same way. Looking at Eq.(1.4) it can be realized that the Reynolds number represents a measure of the relative strength between the non–linear convective term $(\boldsymbol{u} \cdot \nabla)\boldsymbol{u}$ and the viscous term $\nu\nabla^2\boldsymbol{u}$. The higher Re, the more important the non–linear term is in the dynamics of the flow. Turbulence is a genuine result of the non–linear dynamics of fluid flows. When Re is small the motion of the elements of fluid is dominated by diffusive effect, while when Re is large there are the convective effects to dominate the dynamics. It can be recognized that the effects have different characteristic times, precisely the *convective time* $\tau_L \sim |(\boldsymbol{u}\cdot\nabla)|^{-1} \sim L/U$ and the *diffusive time* $\tau_D \sim |\nu\nabla^2|^{-1} \sim L^2/\nu$. The Reynolds number can also be defined as the ratio of the two times

$$Re = \frac{\tau_d}{\tau_l}. \tag{1.6}$$

From the above definitions of characteristic times it can be extracted the rate of energy injected (for mass unit), $\epsilon_L \sim u_L^2/\tau_L \sim u_L^3/L$, and the rate of dissipated energy, $\epsilon_D \sim u_L^2/\tau_D \sim u_L^2\nu/L^2$, and finally we can note that

$$Re \sim \frac{\epsilon_L}{\epsilon_D}, \tag{1.7}$$

at scale L the injection energy rate is Re times the dissipation rate. To be dissipated, energy must be transferred to small scale, this statement introduce the concept of *energy cascade*. Another important characteristic of the NS equations is that they possess scaling properties (11), this means that there exist a class of solutions which are invariant under scaling transformations. In particular, in the inviscid case, the introduction of a lenght scale ℓ, for which the resulting scaling transformations are $\ell \to \lambda\ell^{'}$ and $\boldsymbol{u} \to \lambda\boldsymbol{u}^{'}$, leaves invariate the NS equations for any scaling exponent h (I refer the reader to the lecture of (109) for more informations). When the viscid term is taken into account, a characteristic length scale is introduced, say the dissipative scale ℓ_D. From a phenomenological point of view, this is the scale where dissipative effects start to be experienced by the flow. Of course, since ν is in general very low, we expect that ℓ_D is very small. At this point, if it is considered a complete separation of scales, at very large Re, between the injection scale, L, and the dissipative one, ℓ_D, and the regime is stationary, the energy injection rate must be balanced by the energy dissipation rate and must also be the same as the energy transfer rate ϵ measured at any scale ℓ within the inertial range $\ell_D \ll \ell \ll L$.
When the scaling invariance holds, all the statistical properties of the field depend on the lenght scale ℓ, the mean energy dissipation rate ϵ and the viscosity ν, and with some assumptions and some math, it can be shown that in the inertial range

$$E(k) \sim \epsilon^{2/3}k^{-5/3} \tag{1.8}$$

that represent the *Kolmogorov spectrum* largely observed in all experimental investigation in turbulence. The above consideration, about the scaling invariance and the energy transfer in the inertial range, are the main results of the $K41$ theory of A.N.Kolmogorov (12)–(11) and, historically, they represented a great step in the understanding of the phenomenology of the turbulence and, as some scientists affirm, perhaps the only serious result that we know about turbulence. Throughout the 1940's there were numerous additional contributions to the study of turbulence; I mention only a few selected ones here. For the most part, this decade produced a consolidation of earlier statistical work. Works of (16), (17), (18), (19) and (20) are among the most often cited, with those of (21; 22) involving experiments.

In the last fifty years, new interesting insights in the theory of turbulence derive from the point of view which considers a turbulent flow as a complex system, a sort of benchmark for the theory of dynamical systems. The theory of chaos received the fundamental impulse just through the theory of turbulence developed by Ruelle and Takens (6) who, criticizing the old theory of Landau and Lifshitz (7), were able to put the numerical investigation by Lorenz (8) in a mathematical framework. Gollub and Swinney (10) set up accurate experiments on rotating fluids confirming the point of view of Ruelle and Takens (6) who showed that a strange attractor in the phase space of the system is the best model for the birth of turbulence. This gave a strong impulse to the investigation of the phenomenology of turbulence from the point of view of dynamical systems (9).

To close this section I present a list of physical attributes of turbulence, that for the most part summarizes the preceding discussions, and which are essentially always mentioned in descriptions of turbulent flow. In particular, a turbulent flow can be expected to exhibit all of the following features:

1. disorganized, chaotic, seemingly random behavior;
2. nonrepeatability (i.e., sensitivity to initial conditions);
3. extremely large range of length and time scales (but such that the smallest scales are still sufficiently large to satisfy the continuum hypothesis);
4. enhanced diffusion (mixing) and dissipation (both of which are mediated by viscosity at molecular scales);
5. three dimensionality, time dependence and rotationality (hence, potential flow cannot be turbulent because it is by definition irrotational);
6. intermittency in both space and time.

1.2 Plasma Turbulence

Turbulence is not only a prerogative of classical fluids, but manifest itself also in electrically conducting fluids. The most natural conducting fluid is a ionized gas, called *plasma*, that is a system of charged particles whose dynamics is dominated by collective effect, i.e. each particle feels the average electromagnetic fields generated by the distribution and the motion of the other particles of the system. In other words, ”plasma“ is used in physics to designate the high temperature ionized gaseous state with charge neutrality and collective interaction between the charged particles and waves. By an ”ionized“ gas it is meant that there are significant numbers of free (unbound) electrons and electrically charged ions in addition to the neutral atoms and molecules normally present in a gas.

Most of the matter that we can observe directly is in the plasma state and the universe abounds with plasma turbulence. Research on plasmas is an active scientific area, motivated by energy research, astrophysics and technology. In space physics and in astrophysics (23; 24; 25), numerous data from measurements have been heavily analyzed and reviewed (27; 28). In nuclear fusion research, studies of confinement of turbulent plasmas have lead to a new era, namely that of the international thermonuclear (fusion) (14) experimental reactor, as ITER. In addition, plasmas play important roles in the development of new materials with special industrial applications.

The plasmas that we encounter in research are often far from thermodynamic equilibrium: hence various dynamical behaviours and structures are generated because of that deviation. Turbulence plays a key role in producing and defining those observable structures. Common to these turbulent systems is the presence of an inertial range, an extent of scales through which energy cascades from the large scales at which the turbulence is stirred to the small scales at which dissipative mechanisms convert the turbulent energy into heat. Plasmas are nearly always found to be magnetized and turbulent, and in particular, the turbulent motions are accompained by magnetic field fluctuations.

Turbulence in plasmas has several characteristic features. The first is that the fluctuation level becomes high through the instabilities driven by the inhomogeneity. The turbulent level and spectrum are greatly influenced by the spatial inhomogeneity and plasma configuration. Inhomogeneities exist for plasma parameters (e.g., density and temperature) as well as for the fields (magnetic field and radial electric field). These inhomogeneities couple together to drive and/or suppress instabilities and turbulent fluctuations. In particular, the anisotropy along and perpendicular to strong magnetic fields induces various shapes in fluctuations: fluctuations often have a very long correlation length along the magnetic field lines and are quasi–two–dimensional. In addition, the mobilities of electrons and ions clearly differ. The inhomogeneities, the anisotropy due to a strong magnetic field, and the difference in ion and electron mobilities, all have a strong influence on the linear properties of the plasma waves as well as on the turbulent transport in plasmas. Theoretical methods developed for fluid turbulence are helpful for the study of these phenomena. In the quest to understand anomalous transports in confined plasmas, investigation of turbulent fluctuations has been a central theme. In particular, after the discovery of high-confinement (H) modes in tokamaks (15), it was widely recognized that the plasma profiles vary and that the changes between them occur as sudden transitions. One of the keys to understanding the structural formation and transitions in plasmas is to study the mutual interactions among plasma inhomogeneities, electric-field structures and fluctuations.

Before presenting a more detailed description of the plasma turbulence, it is useful to go one step back to briefly describe the theoretical approach to plasma physics. The theoretical description of a plasma is extremely difficult, more specifically, the distributions and motions of the particles generate fields that, in turn, are responsible for those distributions and motions and, considering the huge number of particles ($N \sim N_A$), this means solve exactly a set of N_A equations of motion coupled with Maxwell's equations. The last consideration obliged physicists to find a good compromise between rigor, mathematical tractability and common sense, to finally elaborate some theoretical schemes. There are basically three levels of description in plasma physics: the *exact microscopic* description (or *orbit theory*), *kinetic theory*, and the *macroscopic* or *fluid* description. In a microscopic description, one imagines to direct study of the particle motion, that is writing down Newton's law, $\mathbf{F} = m\mathbf{a}$, for something like 10^{23} particles and solving for all 10^{23} interacting trajectories, that it is still unimaginable today, even by the most advanced computers. Nonetheless, the microscopic description is useful as a formal starting point from which to derive soluble, practical descriptions. In the following two subsection, it will be described in more detail the kinetic and fluid plasma theories and their turbulent ”implication“, emphasizing the role of the *magnetohydrodynamic* approximation and turbulence.

1.2.1 Kinetic plasma theory

The microscopic theory passed to kinetic theory by the application of statistical, probability concepts. The kinetic theory represent, probably, the best possible trade-off between completeness of information and mathematical simplicity. Since one is not interested in all the microscopic particle data, one considers statistical ensembles of systems. In order to describe the properties of a plasma, it is necessary to define a distribution function that indicates particle number density in the phase space whose ordinates are the particle positions and velocities. What just said means that all the relevant informations are contained in the particle distribution function (PDF), $f_\alpha(\mathbf{r}, \mathbf{u}, t)$, for species α defined such that $f_\alpha(\mathbf{r}, \mathbf{u}, t) d\mathbf{r} d\mathbf{u} = dN(\mathbf{r}, \mathbf{u}, t)$ is the number of particles in the element of volume $dV = d\mathbf{r}d\mathbf{u}$ in phase space ($\mathbf{r}$ and $\mathbf{u}$ represent, respectively, the position and velocity vectors that define the particles positions in phase space). By averaging out the microscopic information in the exact theory, one obtains statistical kinetic equations that describe the evolution of particle distribution function in space and time. If the collision between particles cannot be neglected, some suitable physical model has to be adopted (different models give rise to different kinetic equations, like the *Boltzmann equation* or the *Fokker-Plank-Landau equation*), while, if the collision can be neglected (for example when the plasma is rarified), the kinetic equation can be reduced to a simplest form, called the *Vlasov equation* (or the *collisionless plasma kinetic equation*). The nominal condition for neglecting the collisional effects is that the frequency of the relevant physical process(es) be much larger than the collision frequency: $d/dt \sim -i\omega \gg \nu_L$, in which ν_L is the Lorentz collision frequency and ω represents whichever of the various fundamental frequencies (e.g., ω_p , plasma; kc_S , ion acoustic; ω_c , gyrofrequency; ω_D , drift) are relevant for a particular plasma application.

As already said, the kinetic equation has to be coupled with Maxwell's equations and this give rise to a nonlinear integro-differential system, that for the Vlasov approximation assumes the following form :

$$\frac{\partial f_\alpha}{\partial t} + \frac{\partial f_\alpha}{\partial \mathbf{r}} + \frac{q_\alpha}{m_\alpha}(\mathbf{E} + \mathbf{u} \times \mathbf{B}) \cdot \frac{\partial f_\alpha}{\partial \mathbf{u}} = 0 \tag{1.9}$$

$$\nabla \times \boldsymbol{E} = -\frac{\partial \boldsymbol{B}}{\partial t}; \quad \nabla \times \boldsymbol{B} = \mu_0 \boldsymbol{j} + \frac{1}{c^2}\frac{\partial \boldsymbol{E}}{\partial t}$$

$$\nabla \cdot \boldsymbol{E} = \frac{\rho}{\epsilon_0}; \quad \nabla \cdot \boldsymbol{B} = 0$$

$$\begin{aligned} \rho &= \sum_\alpha q_\alpha n_\alpha = \sum_\alpha q_\alpha \int f_\alpha d^3\boldsymbol{u} \\ \mathbf{j} &= \sum_\alpha q_\alpha n_\alpha U_\alpha = \sum_\alpha q_\alpha \int f_\alpha \mathbf{u} d^3\boldsymbol{u} \end{aligned} \tag{1.10}$$

The above set of equations (6-dimensional in phase space), completed with the equations for the charge and the current density Eq. (1.10), are the fundamental set of equations that provide a complete kinetic description of a plasma and describe phenomena in which collisions are not important, keeping track of the (statistically averaged) particle distribution function. Plasma waves are the most important phenomena covered by the Vlasov–Maxwell equations. In the Vlasov model the distribution function f is constant along the particle orbit in phase space, the entropy is conserved and, because the Vlasov equation has no discrete particle correlation (Coulomb collision) effects in it, it is completely reversible (in time) and its solutions follow the collisionless single particle orbits in the six-dimensional phase space. Although the above properties and considerations, exact solutions of the Vlasov–Maxwell system, unfortunately, can be found only in very particular cases. All the kinetic theories present some lack, in particular it is still too complicated to deal with realistic cases and it is complicated to direct compare results with observation data (particle distribution functions are very difficult to measure and the only exception is the case of solar wind that permit in situ measurement). In plasma theories some physically relevant parameters (density, flow velocity, temperature), directly comparable with the observations, can be obtained from the moments of the particle distribution function integrating low order powers of the velocity $\mathbf{u}$ times the distribution function f over velocity space in the laboratory frame: $\int d^3u \mathbf{u}^j f(\mathbf{r}, \mathbf{u}, t)$, $j = 0, 1, 2$. The integrals are all finite because the distribution function must fall off sufficiently rapidly with speed so that these low order, physical moments (such as the energy in the species) are finite. That is, we cannot have large numbers of particles at arbitrarily high energy because then the energy in the species would be unrealistically large or divergent. Fluid moment equations are derived by taking velocity–space moments of the relevant kinetic equation.

1.2.2 Fluid plasma theories

Just as the velocity moments of the distribution function give important macroscopic variables, so the velocity moments of the plasma kinetic equation give the equations that describe the time evolution of these macroscopic parameters. Because these equations are identical with the continuum hydrodynamic equations, the theories using the low–order moments are called *fluid theories*. Fluid theories provide the equations that determine the dynamics of the moments of the PDF, but, since there are an infinite number of moments, physician are in principle led from a single kinetic equation to an infinite system of coupled equations, in fact, it is important to recognize that while each fluid moment of the kinetic equation is an exact equation, the fluid moment equations represent a hierarchy of equations which, without further specification, is not a complete (closed) set of equations. The sequence must be terminated by some reasonable procedure, so it is necessary to find a way to truncate to a small number of consistent equations, and usually this is effected by setting the third velocity moment of f to zero. This is known as the **closure** problem that underlies fluid model and that does not have a unique solution.
In fluid theories all information on velocity distribution is lost, but the quantities appearing in those theories have direct physical meaning in configuration space and are therefore directly comparable with measurable physical parameters. There are three main approaches in the fluid description of a plasma: *multifluid models*, *single fluid models* and *magnetohydrodynamics*, but I will concentrate on the last one, thus it will only be a brief presentation of the other two approaches.

Multifluid models are used whenever the interaction between different species in the plasman are weak, so that each species evolves almost indipendently of the others, with coupling through the electromagnetic fields and collision. Since there are at least two species of particles in a plasma, there are at least two sets of fluid equations (ions and electrons). When collision and viscosity can be neglected, the complete set of equation (continuity, eq. of motion and eq. of state) for the two–fluid model assume the form:

$$\frac{\partial n_\alpha}{\partial t} + \nabla \cdot (n_\alpha \boldsymbol{u}_\alpha) = 0 \tag{1.11}$$

$$m_\alpha n_\alpha \left[\frac{\partial \boldsymbol{u}_\alpha}{\partial t} + (\boldsymbol{u}_\alpha \cdot \nabla)\boldsymbol{u}_\alpha \right] = q_\alpha n_\alpha (\boldsymbol{E} + \boldsymbol{u}_\alpha \times \boldsymbol{B}) - \nabla p_\alpha \tag{1.12}$$

$$p_\alpha = C_\alpha n_\alpha^{\gamma_\alpha} \tag{1.13}$$

for species α=i,e and supplemented by Maxwell's equations for the electric and magnetic fields. Charge and current densities are defined, respectevely, as $\sigma = n_i q_i + n_e q_e$ and $\boldsymbol{j} = n_i q_i \boldsymbol{u}_i + n_e q_e \boldsymbol{u}_e$, while p_α is the scalar pressure, C is a constant and γ_α is the ratio between specific heats. These two sets of equations provide 16 independent equations for the 16 unknowns n_i, n_e, p_i, p_e, $\boldsymbol{u}_i$, $\boldsymbol{u}_e$, $\boldsymbol{E}$ and $\boldsymbol{B}$.

Single fluid models replace the entire set of equations for the different fluids with just one set of equation for an *equivalent* fluid.

Finally, *Magnetohydrodynamics* is a particular regime of single fluid models, specifically it is a combination of a one-fluid (hydrodynamic-type plus Lorentz force effects) model for the plasma and the Maxwell equations for the electromagnetic fields. Magnetohydrodynamics (MHD, hereafter) is the name given to the non–relativistic single fluid model of a magnetized, small gyroradius plasma. The MHD description is derived by adding appropriately the two–fluid equations to obtain a "one-fluid" description and then making suitable approximations. It can be distinguished two level of MHD description: *ideal* and *resistive* MHD. In the *ideal* MHD description one has to obtain density, momentum and equation of state equations that govern the macroscopic behavior of a magnetized plasma on fast time scales where dissipative processes are negligible and entropy is conserved. Thus, ideal MHD processes are isentropic. In the *resistive* MHD there is an extention of the time scale beyond the electron collision time scale ($\sim 1/\nu_e$) by adding to ideal MHD the irreversible, dissipative effects due to the electrical resistivity in the plasma. The MHD scheme achieves a considerable simplification of the single–fluid equations. The plasma variables, that is the total mass density of plasma ρ , the flow velocity of plasma $\mathbf{u}$, the plasma pressure p and the current density $\mathbf{j}$ are defined as follows:

$$\rho = m_e n_e + m_i n_i \simeq m_i n_i \tag{1.14}$$

$$\boldsymbol{u} = \frac{m_e n_e \boldsymbol{u}_e + m_i n_i \boldsymbol{u}_i}{\rho} \simeq \boldsymbol{u}_i \tag{1.15}$$

$$p = p_e + p_i = 2nk_B T \tag{1.16}$$

$$\boldsymbol{j} = -n_e e(\boldsymbol{u}_e - \boldsymbol{u}_i) \tag{1.17}$$

A one–fluid mass density (continuity) equation for the plasma is obtained by multiplying the electron and ion density equations by their respective masses to yield $\partial\rho/\partial t + \nabla \cdot \rho\boldsymbol{u} = 0$. Multiplying the density equations by their respective charges (q_α) and summing over species yields the charge continuity equation $\partial\rho_q/\partial t + \nabla \cdot \boldsymbol{j}$ $= 0$. In MHD the plasma is presumed to be quasineutral because we are interested in plasma behavior on time scales long compared to the plasma period ($\omega \ll \omega_p$) and length scales long compared to the Debye shielding distance ($\lambda_D/\delta x \sim k\lambda_D \ll 1$). In the MHD model the charge continuity equation simplifies to $\nabla \cdot \boldsymbol{j} = 0$, since MHD plasmas are quasineutral and have no net charge density ($\rho_q = 0$), for this reason the Gauss' law Maxwell equation $\nabla \cdot \boldsymbol{E} = \rho_q/\epsilon_0$ cannot be used to determine the electric field in the plasma. Rather, since a plasma is a highly polarizable medium, in MHD the electric field $\boldsymbol{E}$ is determined self–consistently from Ohm's law ($\boldsymbol{E} = \boldsymbol{j}/\sigma - \boldsymbol{u} \times \boldsymbol{B}$), Ampere's law ($\nabla \times \boldsymbol{B} = \mu_0 \boldsymbol{j}$) and the charge continuity equation ($\nabla \cdot \boldsymbol{j} = 0$).
The complete set of "one–fluid" equations (continuity, momentum, energy and induction) reads:

$$\partial\rho/\partial t + \nabla\cdot\rho\boldsymbol{u} = 0 \tag{1.18}$$

$$\rho\frac{\partial \boldsymbol{u}}{\partial t} + (\boldsymbol{u}\cdot\nabla)\boldsymbol{u} = -\nabla P + \frac{1}{\mu_0}(\nabla\times\boldsymbol{B})\times\boldsymbol{B} + \\ + \boldsymbol{F}_{ext} + \left[\rho\nu\left(\nabla^2\boldsymbol{u} + \frac{1}{3}\nabla(\nabla\cdot\boldsymbol{u}\right)\right] \tag{1.19}$$

$$\rho\left(\frac{\partial w}{\partial t} + (\boldsymbol{u}\cdot\nabla)w\right)p\nabla\cdot\boldsymbol{u} = \left[\frac{\boldsymbol{j}^2}{\sigma} - \nabla\cdot\boldsymbol{Q} - L_{rad} + H\right] \tag{1.20}$$

$$\frac{\partial \boldsymbol{B}}{\partial t} = \nabla\times(\boldsymbol{u}\times\boldsymbol{B}) + \eta\nabla^2\boldsymbol{B} \tag{1.21}$$

where σ is the conductivity of the medium, $w = p/\rho(\gamma-1)$ is the internal energy, $\mathbf{Q}$ is the heat flux vector, $\boldsymbol{F_{ext}}$ represent the sum of external forces, while H and L_{rad} are the heat source term and the radiation loss term. The terms in square brackets are the ”non–ideal“ terms.

The continuity equation describes changes in mass density due to advection and compressibility by the mass flow velocity $\boldsymbol{u}$. The charge continuity equation is the quasineutral ($\rho_q \simeq 0$) form of the general charge continuity equation that results from adding equations for the charge densities of the electron and ion species in the plasma. The momentum equation, which is also known as the equation of motion, provides the force density balance for a fluid element that is analogous to $m\boldsymbol{a} = \boldsymbol{F}$ for a particle. The MHD Ohm's law is just the basic laboratory frame Ohm's law $\boldsymbol{E} = \eta\boldsymbol{j}$ for a fluid moving with plasma mass flow velocity $\boldsymbol{u}$: $\boldsymbol{E'} = \boldsymbol{E} + \boldsymbol{u}\times\boldsymbol{B}$. The equation of motion (1.19) and the equation of magnetic diffusion (1.21) are fundamental equations of magnetohydrodynamics. It is important to note that in (1.21) the ratio of the first term to the second term of the right-hand side (in order of magnitude) defined by

$$\frac{|\nabla\times(\boldsymbol{u}\times\boldsymbol{B})|}{|\eta\nabla^2\boldsymbol{B}|} \approx \frac{U_0L_0}{\eta} = R_m \tag{1.22}$$

is called the *magnetic Reynolds number*, where L_0 and U_0 are typical size and velocity of the considered system. Magnetic Reynolds number is equal to the ratio of magnetic diffusion time $\tau_R = \mu_0 L^2/\eta$ to Alfvèn transit time $\tau_H = L/u_A$ (it is assumed that $u \approx u_A = \boldsymbol{B}_0/\sqrt{4\pi\rho}$, the Alfvèn speed related to the large-scale L_0 and mean magnetic field $\boldsymbol{B}_0$), that is, $R_m = \tau_R/\tau_H$. When $R_m \gg 1$, the magnetic field in a plasma changes according to diffusion equation. When $R_m \ll 1$, it can be shown that the lines of magnetic force are frozen in the plasma.

The usual approximations of MHD are to use the assumption of incompressible fluid ($\nabla\cdot\boldsymbol{u} = 0$), adiabatic fluid ($d/dt\ (p\rho^{-\gamma}) = 0$) and isothermal fluid ($d/dt\ (p/\rho) = 0$). All the MHD description is certainly invalid if the frequency is too high or the wavelenght is too short and implies a certain ordering of lenght an time scales in the dynamics of the plasma. Another limitations stay in the neglecting of charge separation that, as already said, restrict the MHD equations to wavelenght $\lambda \gg \lambda_D$

and implies that electrons and ions move together; the last consideration adds another restriction to the time scale of MHD dynamics, $T \gg \omega_{ci}^{-1}$, because motions as rapid as cyclotron motions will affect the ions differently from the electrons. Again, the assumption of scalar pressure, on a collisionless time scale, in a magnetic field, it is not clear because it is not known what time and space scales are required to justify the assumption. Even the last consideration, the MHD model describes a very wide range of phenomena in small gyroradius, magnetized plasmas, macroscopic plasma equilibrium and instabilities, Alfvèn waves, magnetic field diffusion. It is the fundamental, lowest order model used in analyzing magnetized plasmas.

1.2.2.1 Criteria for the right choice of Plasma description

In the last two section I briefly and roughly introduced the main aspect of the kinetic and MHD plasma description and their limitations. At this point, one may ask which kind of plasma descriptions has to be taken into account for describing various types of plasma processes in magnetized plasmas.
The fastest, finest scale processes require kinetic descriptions, but then over longer time and length scales more fluidlike, macroscopic models become appropriate. In a magnetized plasma there are many more relevant parameters, and their relative magnitudes and consequences can vary from one application to another. MHD depend on the assumption that the plasma is strongly collisional , so that the time scale of collisions is shorter than the other characteristic times in the system, and the particle distributions are Maxwellian. This is usually not the case in fusion, space and astrophysical plasmas. When this is not the case, or we are interested in smaller spatial scales, it may be necessary to use a kinetic model which properly accounts for the non-Maxwellian shape of the distribution function. However, because MHD is relatively simple and captures many of the important properties of plasma dynamics it is often qualitatively accurate and is almost invariably the first model tried.

1.2.3 Plasma instabilities and turbulence

So far, I introduced the main aspect of plasma turbulence without any detail. Now, after the general overview on the two main description of the plasma physics, I can briefly talk about how a plasma becomes unstable and turbulent and present the main characteristic of *kinetic* and *MHD turbulence*.

A plasma could be considered always instable, this comes from the fact that a plasma is a system with a enormous number of degrees of freedom. The last affirmation implies that there exist a great number of ways to lost the equilibrium, so that it is estremely easy to found some unstable degree of freedom. An instability is a process in which a small perturbation in a plasma equilibrium state grows larger in time (note that instabilities develop at different rates and timescales). In a practical sense, an instability often represent the ability of a plasma to escape from a configuration of fields that would otherwise contain a single charged particle indefinitely. The study of instabilities has a central role in plasma physics. On one hand, the understanding of the mechanism underlying the development of instabilities is fundamental to controlling them, on the other hand the observation of configuration lasting longer than expected clearly proves that there are in nature ways to control at least the fastest instabilities. The objective of much plasma research has been dedicated to device configurations for the confinement of a high-temperature plasma where instabilities tend to deassemble the confinement. In many of this kind of plasma experiments an equilibrium state is never estabilished, because the lenght of time required to produce the plasma is already comparable with an instability growth time. A given equilibrium may be unstable in a variety of ways, and a given instability may be common to several plasma equilibria.

1.2.3.1 Kinetic plasma turbulence

Kinetic plasma instabilities are driven by the velocity anisotropy of plasma particles residing in a temperature anisotropy, or in a bulk relative motion of a counter streaming plasma or a beam-plasma system. The excitations can be electromagnetic or electrostatic in nature and can release different forms of free energy stored in anisotropic plasmas. These instabilities are widely invoked in various fields of astrophysics and laboratory plasmas. Thus, the so called magnetic instabilities of the Weibel-type can explain the generation of magnetic field seeds and the acceleration of plasma particles in different astrophysical sources (e.g., active galactic nuclei, gamma-ray bursts, Galactic micro quasar systems, and Crab-like supernova remnants) where the nonthermal radiation originates, as well as the origin of the interplanetary magnetic field fluctuations, which are enhanced along the thresholds of plasma instabilities in the solar wind. Furthermore, plasma beams built in accelerators (e.g., in fusion plasma experiments) are subject to a variety of plasma waves and instabilities, which are presently widely investigated to prevent their development in order to stabilize the plasma system. At a scale larger than the particle mean free path, the plasma is stirred by some external mechanism, driving an assortment of MHD Alfven, fast, slow, and entropy mode fluctuations in the plasma. At this driving scale, a turbulent cascade develops nonlinearly to transfer the fluctuation energy to smaller scales. The compressive modes become damped as the cascade reaches scales of order or smaller than the collisional mean free path, but the Alfvenic cascade continues undamped down to the scale of the ion Larmor radius. At this kinetic scale, the electromagnetic fluctuations may be damped collisionlessly by the Landau resonance with the ions. In the absence of collisions, this process conserves the free energy removed from the electromagnetic fluctuations that generates nonthermal structure in velocity space of the ion distribution function. The remaining electromagnetic fluctuation energy continues to cascade below the scale of the ion Larmor radius as a kinetic Alfven wave cascade. Upon reaching the scale of the electron Larmor radius, the electromagnetic fluctuations of the kinetic Alfven wave cascade are completely damped via the Landau resonance with the electrons; again, a generalized energy is conserved in this process, leading to the creation of nonthermal structure in velocity space of the electrons. But the damping of the electromagnetic fluctuations and consequent generation of structure in velocity space does not correspond to heating. The thermalization of the turbulent energy by collisions is ultimately achieved thanks to a cascade to small scales in velocity space of the particle distribution functions (an entropy cascade). The entropy cascade drives the distribution function structure in velocity space to scales small enough that even weak collisions are sufficient to smooth out that structure towards the Maxwellian, causing entropy to increase, and this is the final step in the conversion of the energy of the turbulent fluctuations to thermal energy of the plasma particles. The entire process described above is one of the possible numerical model to describe, in a kinetic generalization, the familiar cascade of energy in a fluid turbulent system.

1.2.3.2 MHD plasma turbulence

A plasma flow becomes unstable when the gradient of velocity, pressure, or magnetic field exceed a certain treshold, which occurs when the convective transport of momentum, heat, or magnetic flux is more efficent than the corresponding diffusive transport by viscosity, thermal conduction, or resistivity. In the macroscopic description of plasma dynamics, there are three main types of instabilities which play a fundamental role : the *Kelvin–Helmholtz* instability driven by a velocity shear; the *Rayleight–Taylor* instability caused by the buoyancy force in a stratified system; and *current–driven MHD* instabilities in a magnetized plasma, in particular the *tearing* instability. Additionally, the presence of magnetic fields, rotation, or stable stratification may exert a stabilizing influence on a otherwise unstable fluid. In many systems several instability mechanisms may become active.

Many dynamical processes observed in plasma fluids can be attributed to the effect of some instability of a stationary system. After the onset of instability the structure of the flow is very complex and irregular and, most importantly, the further behaviour is impredicable. Instabilities may give rise to rather coherent dynamics such as the kinking of a plasma column, but more often, especially at high Reynolds number, turbulence will be generated. MHD turbulence is characterized by nonlinear interactions among fluctuations of the magnetic field and flow velocity over a range of spatial and temporal scales. MHD turbulence occurs almost inevitably in plasmas in motion and is therefore a widespread phenomenon in astrophysics, for instance in the solar system, where we encounter turbulent magnetic fields in the convection zone and in the solar wind, and in accretion discs, where MHD turbulence is responsible for the angular momentum transport. It plays an important role in plasma heating, the transport of energetic particles, and radiative transfer and is ubiquitous in space and astrophysical plasmas.

By following similar equations one may apply, and generalize, the formalism developed in hydrodinamic turbulence, but in the MHD turbulence the physics is more complex than the fluid case. There are two coupled vector fields, velocity $\boldsymbol{u}$ and magnetic $\boldsymbol{B}$, and two dissipative parameters, viscosity and resistivity. In addition, we have mean magnetic field $\boldsymbol{B}_0$ which cannot be transformed away. The mean magnetic field makes the turbulence anisotropic, further complicating the problem.

Exact solutions given initial and boundary conditions will not be very useful even when they were available, this because field variables are typically random both in space and time. However statistical averages and probability distribution functions are reproducible in experiments under steady state, and they shed important light on the dynamics of turbulence. For this reason many researchers study turbulence statistically. The idea is to use the tools of statistical physics for understanding turbulence. The statistical description of turbulent flow starts by dividing the field variables into mean and fluctuating parts. Then there are computed averages of various functions of fluctuating fields. Unfortunately, only systems at equilibrium or near equilibrium have been understood reasonably well, and a good understanding of nonequilibrium systems is still lacking. In the recent era of research, availability of powerful computers and sophisticated theoretical tools have helped us understand several aspects of MHD turbulence. Numerical simulations have provided many important data and clues for understanding the dynamics of turbulence. They have motivated new models, and have verified or rejected existing models. In that sense, they have become another type of experiment. Because of large values of dissipative parameters, MHD turbulence requires large length and velocity scales. This make terrestrial experiments on MHD turbulence impossible. However, astrophysical plasmas are typically turbulent because of large Reynolds number, say non–linear effects strongly prevails over dissipative effects. Taking advantage of this fact, large amount of solar-wind in-situ data have been collected by spacecrafts. These data have been very useful in understanding the physics of MHD turbulence. Solar wind data favors Kolmogorov's $k^{-5/3}$ spectrum and also shows that MHD turbulence exhibits intermittency.

To close this part of the thesis, I will show, as in the fluid case, an exact relationship in the MHD turbulence. So far, I have been discussing about the inertial range of fluid turbulence. In this regard, a very important result on turbulence, due to Kolmogorov (12), was the so called "4/5–law". Under the hypothesis of homogeneity, isotropy, and, in the limit of infinite Reynolds number, assuming that the turbulent flow has a finite nonzero mean dissipation energy rate ϵ (11), the third-order velocity structure function behaves linearly with ℓ, namely

$$S_\ell^{(3)} = -\frac{4}{5}\epsilon\ell \tag{1.23}$$

Following a similar approach developed by Yaglom (20), Politano and Pouquet (29), derived an exact relation, from MHD equations, for the third-order correlator involving Elsässer variables (30):

$$Y_\ell^{\pm} = \langle[\delta z_\ell^{\pm}]^2 \delta z_\ell^{\mp}\rangle = -\frac{4}{3}\epsilon^{\pm}\ell \tag{1.24}$$

Both Equations (Eq. 1.23, 1.24) might be used, as a formal definition of inertial range. Since they are exact relationships derived from Navier–Stokes and MHD equations under usual hypotheses, they represent a kind of "zeroth-order" conditions on experimental and theoretical analysis of the inertial range properties of turbulence.

CHAPTER 2

Turbulence in Solar Wind

Analytical results are impossible in turbulence research, apart for the *4/5–law*, because of complex nature of turbulence. Therefore, experiments and numerical simulations play very important role in turbulence research. In fluid turbulence, engineers have been able to obtain necessary information from experiments (e.g., wind tunnels), and successfully design complex machines like aeroplanes, spacecraft, etc. Unfortunately, terrestrial experiments exhibiting MHD turbulence are typically impossible because of large value of resistivity and viscosity of plasmas. For a typical laboratory setup magnetic Reynolds numbers result far from turbulent regime. On the other hand, astrophysical plasmas have large length and velocity scales, and are typically turbulent. They are a natural testbed for MHD turbulence theories. We have been able to make large set of measurements on nearest astrophysical plasma, the solar wind, using spacecrafts. The data obtained from these measurements have provided many interesting clues in understanding the physics of MHD turbulence.

2.1 The Solar Wind plasma laboratory

Our Sun lose mass by a continuous radial flow called *Solar Wind*. In the solar corona the plasma is at very high temperature, and because it is not gravitationally bound, it expands (as wonderfully sketched in Fig. 2.1) into interplanetary space in the form of a supersonic plasma flow that extend itself radially up to distance beyond the planetary system until it is slowed down by the termination shock. It forms a bubble structure that extend in the space and it is called heliosphere. The solar wind plasma consist principally of fully ionized atomic particles, electrons and ions (the ion component is composed by a 96% of hydrogen and a small contribution of helium and heavier nuclei).

The solar wind is structured and variable, it varies in density, speed, and temperature, and in the strength and orientation of the magnetic field embedded in its flow. The density of the wind decreases approximately as r^{-2} . The mean magnetic field is largely polar in north–south direction, but spirals out in the equatorial plane. Typical Sound speed ($C_s \approx k_B T/m_p$) is of the order of several hundred km/s. The density fluctuation $\delta\rho/\rho \approx (u/C_s)^2 \approx 0.01$, hence solar wind can be treated as incompressible fluid. The solar wind is also collisionless, in fact his mean free path is very large (for example it is about $\lambda_{mfp} \sim 10^{11}$ at 1 AU, i.e. of the order of the length scale of the system itself). The collision frequency is then typically $\nu \sim 10^{-5}$ Hz, much smaller that the other typical frequencies. Since collisions are very unlikely on the typical length scale and time scales of interest, the plasma

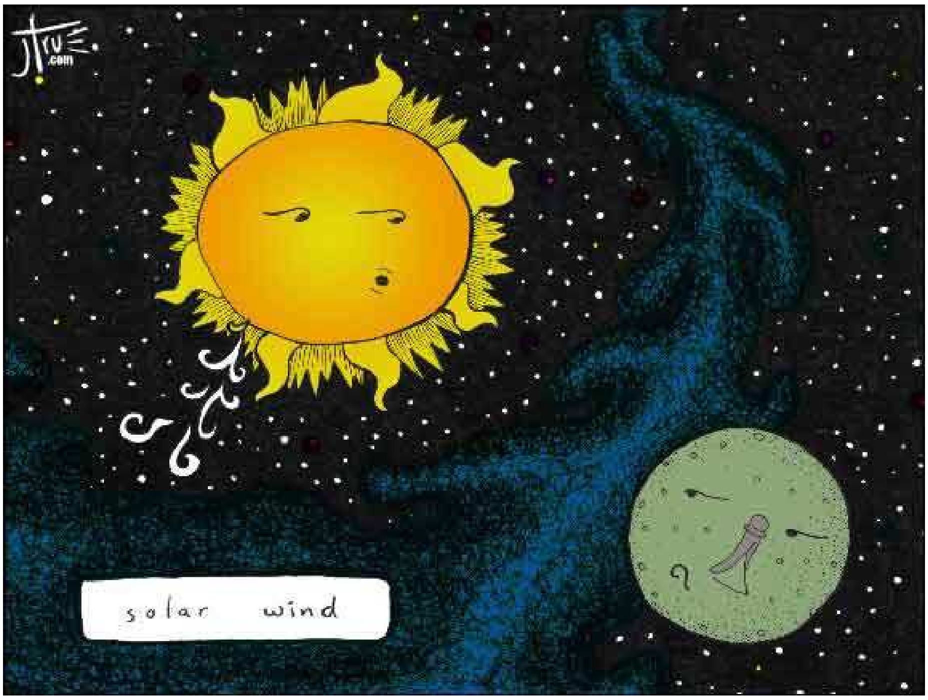

Figure 2.1: A cartoon of the propagation of the Solar Wind in the interplanetary space.

components are usually far from their equilibrium, exhibiting different anisotropies and suprathermal components. The basic physics of the solar wind is described by a one–fluid hydrodynamic model in which it is assumed that there is a stationary radial flow driven only by pressure and gravity. In view of the collisionless character of the plasma, a fluid approach might appear inappropriate, but, on the large global scales, kinetic effects are indeed negligible.

Again, the solar wind is far from steady but carries fluctuations of substantial amplitudes. Such fluctuations are seen in all variables, namely velocity, magnetic field, density, and temperature. The $\boldsymbol{u}$ and $\boldsymbol{B}$ fluctuations are highly correlated at all scales and almost undoubtedly Alfvénic. Instabilities in the solar wind driven by sheared flows, shocks, beams, or anisotropries give rise to a continous driving of the turbulence, which would otherwise decay following one or the other of the selective decay routes. Solar wind turbulence comes mainly in two forms, either with a high velocity-magnetic field correlation, corresponding to outgoing Alfvènic fluctuations, or as essentially uncorrelated fully developed turbulence exhibiting a Kolmogorov spectrum. The solar wind provides an almost ideal laboratory for studying high-Reynolds number MHD turbulence that is free to evolve unconstrained and unperturbed by in situ diagnostics, satellite-mounted magnetometers, probes and particle detectors. Measurements performed by spacecrafts represent a unique chance to investigate a wide range of scales of low–frequency turbulence in a magnetized medium.

In the first part of this thesis work it will be treated two aspect of solar wind turbulence : i) nonlinear coupling between electron and ion dynamics as wave-particle interaction in the context of weak plasma turbulence, and ii) the electrostatic activity at high frequencies, that can results from nonlinear saturation of the wave–particle interaction process, as one of the physical mechanisms that replace the energy dissipation in a collisionless turbulent plasma. To realise those goals it was done a sistematic study of in–situ measurements of electric waveforms obtained by the WAVES experiment on board of STEREO spacecraft. In the rest of the chapter it will be first introduced the tools used for those studies, that is the S/WAVES instruments onboard the STEREO spacecrafts (Sec. 2.2), then it will be described the nonlinear wave–particle coupling as the generation of density fluctuations through a ponderomotive force caused by the high amplitude oscillation of localized packet of Langmuir waves (Sec. 2.3), and, finally, a sistematic comparison of observational datasets with numerical results of hybrid-Vlasov simulations to conjecture that high–frequency activity in solar wind should be a consequence of the nonlinear saturation of the wave-particle interaction process (Sec. 2.4).

2.2 In situ plasma turbulence - The STEREO mission and the S/Waves experiment

The Solar TErrestrial RElations Observatory is a NASA mission (31; 32) that consist of two identical spacecraft (one ahead of Earth in its orbit, the other trailing behind), both in heliocentric orbit in the ecliptic plane at nearly 1 Astronomical Unit. The main objective of the mission is to provide the first–ever stereoscopic measurements to study the Sun and the nature of its coronal mass ejections, as sketched in Fig. 2.2.

The main goals of the mission are:

1. understand the causes and mechanisms triggering coronal mass ejections;
2. characterize the propagation of coronal mass ejections through the heliosphere;
3. discover the mechanisms and sites of energetic particle acceleration in the low corona and the interplanetary medium;
4. and develop a 3-D, time–dependent model of the magnetic topology, temperature, density and velocity structure of the ambient solar wind.

To realize those purposes, the STEREO observatory carries four complementary scientific instruments (in Fig. 2.3an overview one satellite with the various instrument):

1. the Sun-Earth Connection Coronal and Heliospheric Investigation (**SECCHI**) (34): study the 3-D evolution of CME's from birth at the Sun's surface through the corona and interplanetary medium to its eventual impact at Earth;

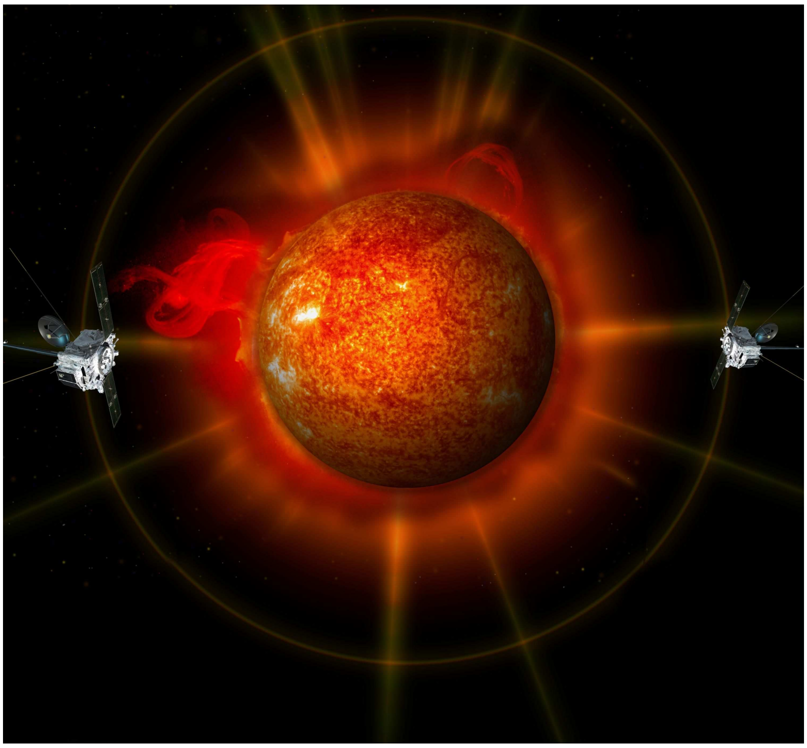

Figure 2.2: Artist's illustration of the twin STEREO satellites on opposites sides of the Sun.

2. the STEREO/WAVES (**S/WAVES**) (35; 36): that is an interplanetary radio burst tracker that traces the generation and evolution of traveling radio disturbances from the Sun to the orbit of Earth;

3. the In situ Measurements of PArticles and CME Transients (**IMPACT**) (37; 38) : sample the 3-D distribution and provide plasma characteristics of solar energetic particles and the local vector magnetic field;

4. the PLAsma and SupraThermal Ion Composition (**PLASTIC**) (39): provide plasma characteristics of protons, alpha particles and heavy ions. This experiment will provide key diagnostic measurements of the form of mass and charge state composition of heavy ions and characterize the CME plasma from ambient coronal plasma.

To the purposes of this thesis, it was made use of data obtained by the S/WAVES experiment. It consists of (i) three radio receivers (fixed, high and low frequency receivers) that track electromagnetic disturbances through the heliosphere and (ii) a Time Domain Sampler (TDS, hereafter) that measures in situ electric waveforms. S/WAVES use three mutually orthogonal wire antenna, each one 6 meters long, with an effective length of about 1 meter, to measure the electric field. The TDS makes rapid samples of waveforms and is intended primarily for the study of Langmuir waves, waves at the plasma frequency and the precursors of type II and III radio

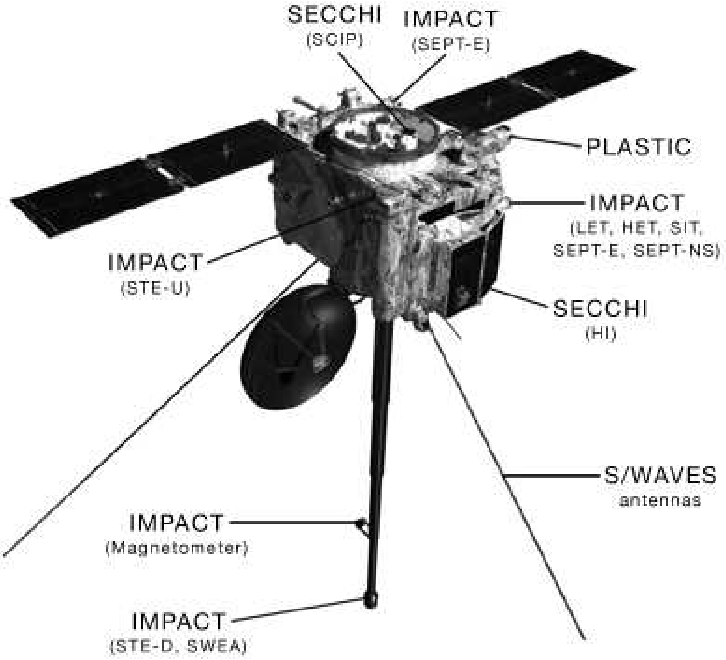

Figure 2.3: Illustration of a spacecraft in its deployed configuration. The SECCHI instruments always point at the Sun, while SWAVES antennas are in the wake of the satellite.

bursts. Other wave modes, such as ion acoustic waves, can also be studied. The TDS works like a modern digital oscilloscope. It samples the voltage on the S/WAVES antennas quickly and continuously. When the sampled amplitude exceeds a commandable threshold, a triggering system takes a snapshot with the largest part of the signal at the center of the time series. The TDS should aquire events in two different ways: with three orthogonal antennas monopole channels (the measured signal is the difference between the antenna potential and the spacecraft potential that is usually considered constant) as well as a pseudo–dipole channel obtained by taking the difference of two monopoles. The selected analog signal is first filtered with a commandable bank of low pass filters to avoid aliasing and then digitized. Since the S/WAVES A/D converter is accurately linear, artificial nonlinear artifacts are not introduced so that studies of nonlinear effects on the waveforms are possible. The instrument is set to work primarily using two different sampling rates of about $\Delta t = 4\ \mu s$ and $\Delta t = 8\ \mu s$ registering up to 16384 samples for each event (in Table 2.1 are showed all the available sampling times of the TDS instrument).

In the frequency domain, the electric field waveforms cover a maximum range that goes from 15 Hz to 125 kHz, enabling, in principle, the detection of signatures from below the electron cyclotron frequency (typically 100 Hz in the solar wind) to above the plasma frequency (10–20 kHz).

	Sample speed (#/s)	Δt (μs)	Pass band filter (kHz)	Total duration(μs)
I	250,000	4	0.1–108	66
II	125,000	8	0.1–54	131
III	31,250	31	0.1–13.5	524
IV	7812	128	0.1–3.38	2,097

Table 2.1: Table of parameters of the runs. The second column is the resolution of the simulation, third column the Reynolds numbers, fourth column reports the dissipative scale of the system and the last column shows the Hall parameter.

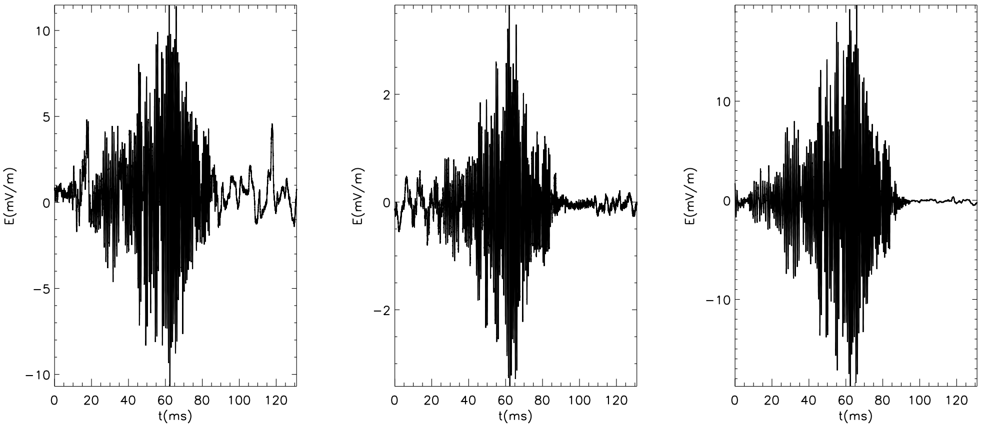

Figure 2.4: Example of TDS electric waveform along the three spacecraft coordinates.

The measured voltage on the three antennas, in monopole mode, is converted into an electric field, and projected in the spacecraft coordinates, using the set of parameters called w/base caps (Graz) (35), in order to take into account the effective length and direction of the STEREO antennas. In its final orbit the spacecraft coordinates (X,Y,Z) are defined as follows: the X–component is sunward along the radial direction, the Z–component is normal to the ecliptic plane, southward for STEREO A and northward for STEREO B, and the Y–component complete the direct orthogonal frame(in Fig. 2.4 an example of electric waveforms along the three antennas in the new reference frame).

2.2.1 Plasma waves measurements with STEREO

Principally, the S/WAVES system was built to the purpose of understanding the mechanism by which electromagnetic waves, the type II and III solar bursts, are generated: the Sun or a shock wave emits energetic electrons which are formed into a beam, the beam generates Langmuir waves by a bump-on-tail instability, and these Langmuir waves are converted to electromagnetic waves. Additionally, a second objective was to continue studies of the fluctuating electric field at frequencies of the order of the ion cyclotron frequency, which has been shown (40) to exert strong forces on ions and is believed to be the major process determining ion heating and isotropy in the solar wind, and play a major role in determining the distribution function and equation of state of the ions. However, as already pointed out (41), the response of the unbiased S/WAVES antennas to density fluctuations completely dominates the response to electric fields in this important frequency range, that means it is at present not possible to measure electric fields in this frequency and amplitude range. In addition, we need to consider the effect of impacting particles; an electric impulse is associated with each particle impacting the surface, producing an antenna shot noise. The larger the total antenna surface, the more impacted charged particles are collected increasing the shot noise and limiting the signal-to-noise ratio and this is the case of STEREO. The TDS noise level in space condition is thus dominated by the shot noise resulting from impacting charged particle on both the antennas and the spacecraft. It is typically about 0.1 mV. On the S/WAVES 1-meters equivalent length antennas, this noise level enable to observe electric field signals with an amplitude larger than 0.1 mV. The electric field fluctuation δE_S associated to an ion acoustic-like density fluctuation $\delta n/n$, by considering a Boltzmanian equilibrium of the electrons, is of the order $\delta E_S \simeq 10^{-4}$ V m^{-1} . Such electric field fluctuation would produce a voltage $\delta V \simeq 0.1$ mV on the S/WAVES antennas. This voltage is comparable to the level of noise, that is the electric field associated to the ion acoustic mode is too low to be observed by S/WAVES. Instead, the density fluctuations themselves have to be observed.

2.2.1.1 Few physics of Langmuir waves : non–linear dynamics and ponderomotive effect

Langmuir, or electron–plasma, waves are waves in which electrons and ions oscillate out of phase. Electrostatic forces resulting from charge separation provide the restoring force, while electrons provide inertia. In a thermal plasma, the frequency ω_L and wave number k of this high–frequency electrostatic wave satisfy the dispersion relation

$$\omega_L \approx \omega_p(1 + 3k^2\lambda_D^2/2) \tag{2.1}$$

where the plasma frequency ω_p is given by $\omega_p = n_e e^2/m_e\epsilon_0$, n_e is the number density of electrons, $\lambda_D = V_e/\omega_p$ is the electron Debye length, $V_e = (k_B T_e/m_e)^{1/2}$ is the electron thermal velocity, T_e is the electron temperature, and m_e is the electron mass. Langmuir waves are found in space plasma wherever there are electron beams propagating parallel to the magnetic field. They are observed associated with electron beams generated by flares, beam induced by shocks, or in the presence of magnetic depressions (also called magnetic holes). Langmuir waves are usually thought to result from bump–on–tail instabilities induced by beams propagating in the solar wind. Unless the phase velocity is much greater than the electron thermal velocity ($\omega_L/kL \gg v_{th_e}$), the Langmuir wave is damped by the Landau damping (a linear phenomenon that describes the local effect (in velocity space) of the distribution function on the waves).

Study of the Langmuir wave system provides a relatively simple illustration of the relevant effects, a strong basis for study of other collapsing and turbulent systems, and many useful tools with which to do so. Non–linear Langmuir waves are also important in their own right, with numerous applications in the laboratory and nature, including ionospheric modification experiments, planetary radio emissions, relativistic–electron–beam systems, and laser–plasma experiments. Langmuir waves depend on the plasma density through ω_p, hence density fluctuations, such as those associated with ion sound waves, will affect the high frequency waves, causing them to refract into regions of low density and high refractive index. This provides a non–linear mechanism to couple high–frequency waves to ion sound waves. Such nonlinearity (essential to Langmuir collapse and strong turbulence) is described by the Zakharov equations (42). In the framework of the Zakharov model, Langmuir waves evolve through different kinds of wave–wave instabilities (decay instabilities, modulational instabilities) depending on the wavelength and amplitude. Fig. 2.5, extracted from (43), summarizes the electrostatic instabilities of interest in the case of the non–linear evolution of a monochromatic Langmuir wave. The first Zakharov

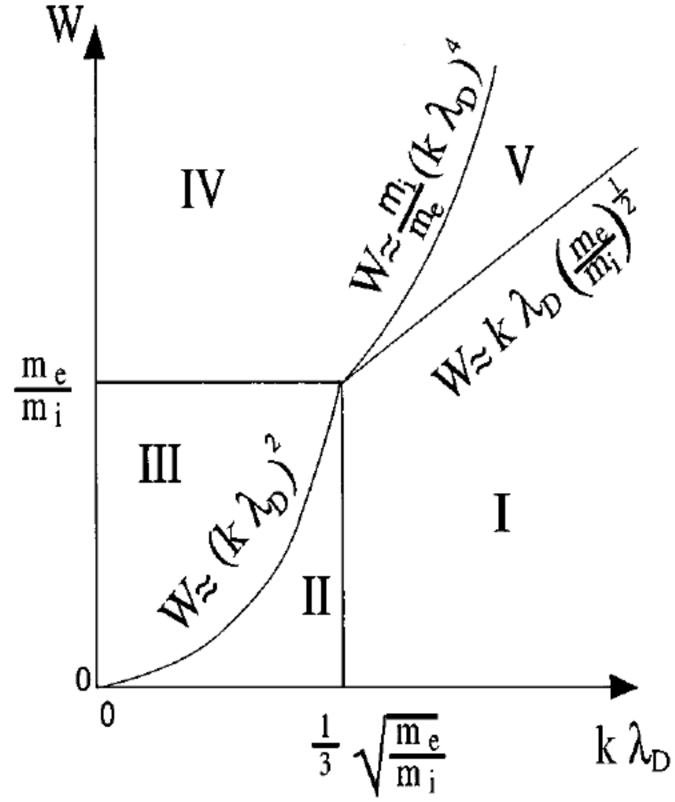

Figure 2.5: Regimes of monochromatic, plane-wave Langmuir instabilities as functions of $k\lambda_D$ and W (the ratio of Langmuir wave energy density to thermal energy density). Approximate boundaries are as labeled. Region I: Electrostatic decay. Region II: Modulational instability. Region III: Subsonic modulational instability. Region IV: Supersonic modulational instability. Region V: Modified decay instability.

equation shows how density fluctuations affect Langmuir waves. To obtain a closed system of equations, the effect of Langmuir waves on density fluctuations is also included. An intense packet of coherent Langmuir waves can produce a density depression via the ponderomotive force. This force comes out when the oscillations of a wave induces an energy density proportional to the square of its amplitude, equivalent to a pressure. When this energy density varies in space, a force proportional to its gradient is exerted on the plasma. It is defined as

$$\boldsymbol{F}_P = \frac{-q^2}{4m_e\omega_p^2}\nabla|\boldsymbol{E}|^2 \tag{2.2}$$

where **E** is the slowly varying electric field amplitude in space. The ponderomotive effect is an essential nonlinear ingredient for the description of modulated, or localized, large–amplitude high–frequency oscillations of the electric field. This force is much stronger for electrons than ions, owing to the inverse dependence on mass in Eq. (2.2). Hence electrons are expelled from the packet, setting up an ambipolar field, which then drags ions out to maintain quasineutrality. Localized Langmuir wave packets with large enough amplitude can for instance dig ion cavities via this ponderomotive force. As time progresses, the initial wave packet narrows and becomes more intense, i.e., it collapses. The corresponding density well also deepens and narrows as the ponderomotive force becomes stronger, as shown schematically in Fig. 2.6 (extracted from (44)). The relative density fluctuation $\delta n/n$ nonlinearly generated by high frequency oscillations of the electric field through this ponderomotive force is expected to saturate at a level comparable to the electric to thermal energy ratio associated to the Langmuir wave:

$$\delta n/n \simeq W_L = \epsilon_0 \boldsymbol{E}^2/nk_BT. \tag{2.3}$$

2.3 Observations of Langmuir ponderomotive effects

The above phenomena is known to physicists and studied since the 70's, but space observational evidence were lacking because it is difficult to simultaneously observe electric field and plasma density variations at comparable spatial scales. In the following, I will describe a method, developed in collaboration with P. Henry, C. Briand and N. Vernet–Meyer at the observatory of Meudon–Paris, that allows such simultaneous observations and recently published on Physics of Plasma review (45). Using waveforms observations from the STEREO/WAVES experiment, we identified for the first time signature of such nonlinear coupling in the solar wind. To our knowledge, this was the first direct quantitative study of density fluctuations nonlinearly coupled to finite amplitude Langmuir waves in space, based on simultaneous observations of electric field and density fluctuations. In Sec. 2.2.1 it was briefly introduced that at low frequencies the response of the TDS results dominated by density fluctuations. This effect is identified observing that, from 100 Hz to few kHz,

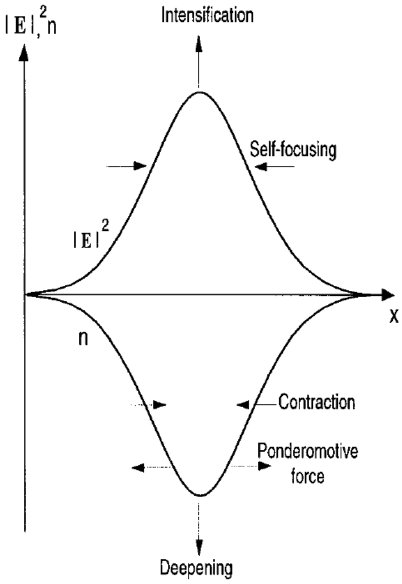

Figure 2.6: Schematic of a collapsing Langmuir wave packet and its associated density well, indicating the self-focusing and intensification of the packet and the deepening and contraction of the density well caused by the ponderomotive force.

the signal recorded by the TDS is often identical on the three monopole antenna channels. Following (41), we recall that this is not a manifestation of waveforms polirized along the bisectrix of the antennas, because that direction is related to the spacecraft geometry and is usually different from any solar wind speed or magnetic field directions, but it comes from the fact that the signal results dominated by local density fluctuations in which the spacecraft is embedded, inducing quasistatic changes in the spacecraft charging. The origin of this local density fluctuation has to be found in the electrical charging of a conducting body due to the lost and collection of charged particles as interaction with the ambient plasma (46). In particular, its electric potential permanently adjusts to the variations of the ambient plasma to ensure the currents balance. At 1 Astronomic Unit (AU) the balance is given between the outgoing photoelectron current and the incoming solar wind electron current. The complete discussion about the current balance, the calibration of the antennas and the way to measure the density fluctuations from the spacecraft potential was left in the appendix A and also in (45). From the discussion, it emerges that, in a quasi–static equilibrium, the level of density fluctuations, as a function of the spacecraft body potential, results approximatively equal to:

$$\delta n/n \simeq -\left(\frac{e}{k_B T_{ph}} + \frac{e}{k_B T_e} + \frac{1}{1+\frac{e\Phi_{SC}}{k_B T_e}}\right)\delta\Phi_{sc} \tag{2.4}$$

where T_{ph} is the temperature of the photoelectrons escaping the spacecraft and T_e the solar wind electron temperature. The value of T_{ph} was evaluated by various author (46; 47; 48; 49) in the range $T_{ph} \simeq [1-4]\times 10^4$ K, while the ambient electron temperature is a order of magnitude greater ($T_e \simeq [1-2] \times 10^5$ K, and this means that density fluctuations are mainly determined by the first term in Eq. (2.4) (details in A). We can now express the variation of the scapecraft potential in function of the level of density fluctuations crossing the spacecraft as :

$$\delta\Phi_{sc} \simeq -\left(\frac{k_B T_{ph}}{e}\right)\delta n/n. \tag{2.5}$$

Following the preceding discussion about the ponderomotive effect, we expect that, if density fluctuations can be measured in this way, then we should be able to observe a strong correlation between the level of density fluctuations and the level of Langmuir electric energy W_L. From the calculations and the discussion about the antennas and spacecraft calibration it comes out that S/WAVES antennas enable to measure simultaneously (i) electric field and (ii) density fluctuations. The electric field is measured through the high frequency variations of the antenna potential Φ_A, while density fluctuations are measured through the low frequency oscillations of the spacecraft potential Φ_{sc}. To verify the effective non–linear coupling mediated by the ponderomotive effect, we identified among the TDS events (data spanning from November 2006 to December 2009.) those that contained (i) the signature of Langmuir oscillation and (ii) the signature of density fluctuations. Langmuir oscillations were selected by considering the waveforms with a localized frequency peak above 5 kHz, while density fluctuations were isolated by considering waveforms whose low frequency part ($<$ 5 kHz) was identical on the three monopole antennas (we recall that the frequency range of detection of density fluctuations is [100 Hz – 1 kHz], while Langmuir waves are observed at the electron plasma frequency that is typically 10–20 kHz in the solar wind at 1 AU). After the selection of the events, for each one the high frequency part of the voltage fluctuations measured on the three antennas is converted into an electric field E_L, associated to Langmuir waves, and projected in the spacecraft coordinates to take into account the effective length and direction of the STEREO antennas. The electric energy is normalized to the electron kinetic energy to evaluate W_L in Eq. (2.3), with the density n estimated from the Langmuir frequency and the choice $T_e \simeq 10^5$ K. Finally, the voltage fluctuations observed identically on the three monopoles in the low frequency part are converted into relative density fluctuations $\delta n/n$ via Eq. (2.5), assuming a photoelectron temperature $T_{ph} = 3$ eV. As example, Fig. 2.7 shows a case in which the Langmuir energy is large enough ($W_L \simeq 10^{-2}$) to generate density fluctuations by ponderomotive effects. As expected from the non–linear theory, the level of density fluctuations is of the order of W_L (the electric–to–thermal energy ratio).

2.3.0.2 Langmuir ponderomotive effects in S/WAVES data

As said above, we choose TDS events form November 2006 to December 2009, but at the very beginning of the STEREO mission (11/2006 – 02/2007) the two satellites were inside the Earth enviroment, in particular they were immersed in the Earth electron foreshock region, a region where Langmuir waves are known to be intense,

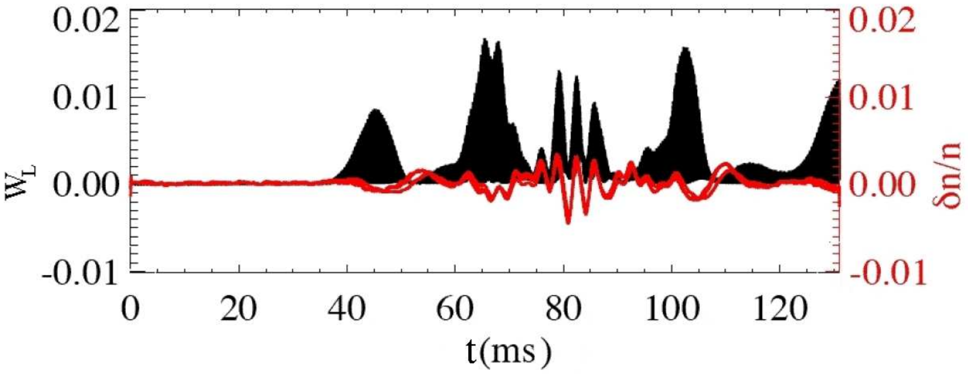

Figure 2.7: TDS waveform in which Langmuir waves, plotted here in term of W_L(t) (black), and density fluctuations $\delta n/n$(t) (red) are observed.

so we separeted the treatment of data in two parts. For each waveform in which both Langmuir waves and density fluctuations are simultaneously observed, we consider (i) the maximum density fluctuation $(\delta n/n)_{max}$ during the whole waveform event and (ii) the maximum normalized Langmuir electric energy $W_{L,max}$ observed during the same waveform event. Results (each single point represent a single measured waveforms) are diplayed in Fig. 2.8. The figure shows the maximum density fluctuation $(\delta n/n)_{max}$ as a function of the maximum normalized Langmuir electric energy $W_{L,max}$. The black dotted lines represent the 3σ detection level to take in account the noise level.

Depending on W_L, two different behaviors are observed. For low energy Langmuir waves ($W_{L,max} < 10^{-4}$), the level of density fluctuations is independent on the level of Langmuir oscillations, that is the density fluctuations are not affected by the propagation of Langmuir waves (linear regime of Langmuir waves). At higher energies, the nonlinear evolution of Langmuir waves affects the density background until it reaches at saturation a level of density fluctuations $(\delta n/n)_{max} \simeq W_{L,max}$. The blue line of Fig. 2.8 is the expected saturation level of density fluctuations forced by Langmuir ponderomotive effects. The transition between the linear and non–linear domain is observed for a normalized Langmuir electric energy $W_{L,max} \sim 10^{-4}$. This result shows how simultaneous in–situ observations of electric field and density fluctuations give observational evidence for non–linear coupling between Langmuir oscillations and density fluctuations. Non–linear ponderomotive effects are at the basics of weak and strong Langmuir turbulence. Following and developing the illustrated metodology to observe contemporaneously finite amplitude Langmuir oscillations and associated density fluctuations will give new insights in non–linear Langmuir processes occurring in the solar wind. To close the discussion, we justified the choice of the photoelectron temperature $T_{ph} \simeq 3$ eV. Fig. 2.9 show the same points of Fig. 2.8, without the enviromental classification(foreshock region, free solar wind), but here the red dotted lines show the level of $\delta\Phi_{sc}$ corresponding to $\delta n/n)_{max} \simeq W_{L,max}$ for different values of T_{ph}, i.e. $T_{ph} = 1$, 3 and 5 eV, taking

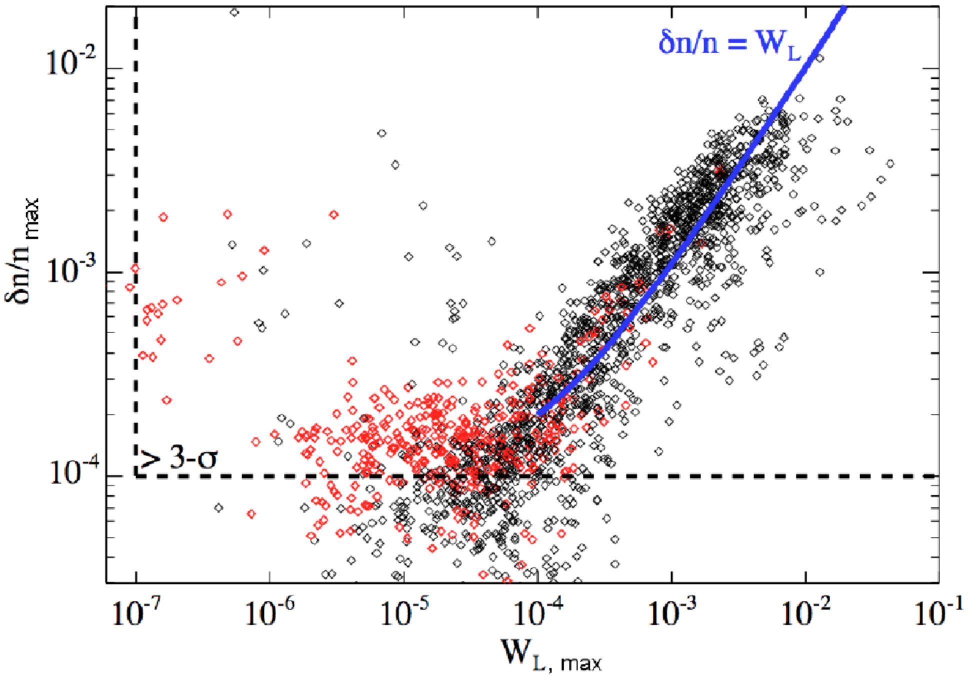

Figure 2.8: Maximum observed density fluctuations $(\delta n/n)_{max}$ vs. maximum Langmuir energy $W_{L,max}$ in the Earth electron foreshock (black diamonds) and in the free solar wind (red diamonds). The blue line represents the expected saturation level of density fluctuations generated by Langmuir ponderomotive effects.

into account the 3σ noise level of the spacecraft potential. The observed level of the spacecraft potential fluctuations is consistent with $T_{ph} = 3 \pm 1$ eV. This value is consistent with previously published values, whereas the linear slope is consistent with the expected saturation level of density fluctuations generated by non–linear Langmuir evolution.

2.4 Electrostatic activity in the high–frequency range of solar wind turbulence

The solar wind plasma, as already said, is usually observed in a physical state of well developed turbulence and represents one of the best natural laboratory for the analysis of the evolution of the turbulent energy cascade, from large MHD length-scales (low frequencies) towards short kinetic wavelengths (high frequency), in the absence of collisional viscosity. While the system dynamics of the solar wind plasma is well established at large wavelengths, thanks to many in situ measurements, key aspects of the physics of turbulence in magnetized plasmas are poorly understood, in particular, the features of the physical evolution at scales of the order of the typical kinetic scales (ion/electron inertial length or gyroradius) are still unclear. The energy of very large–scale fluctuations generated by the Sun is transported down to

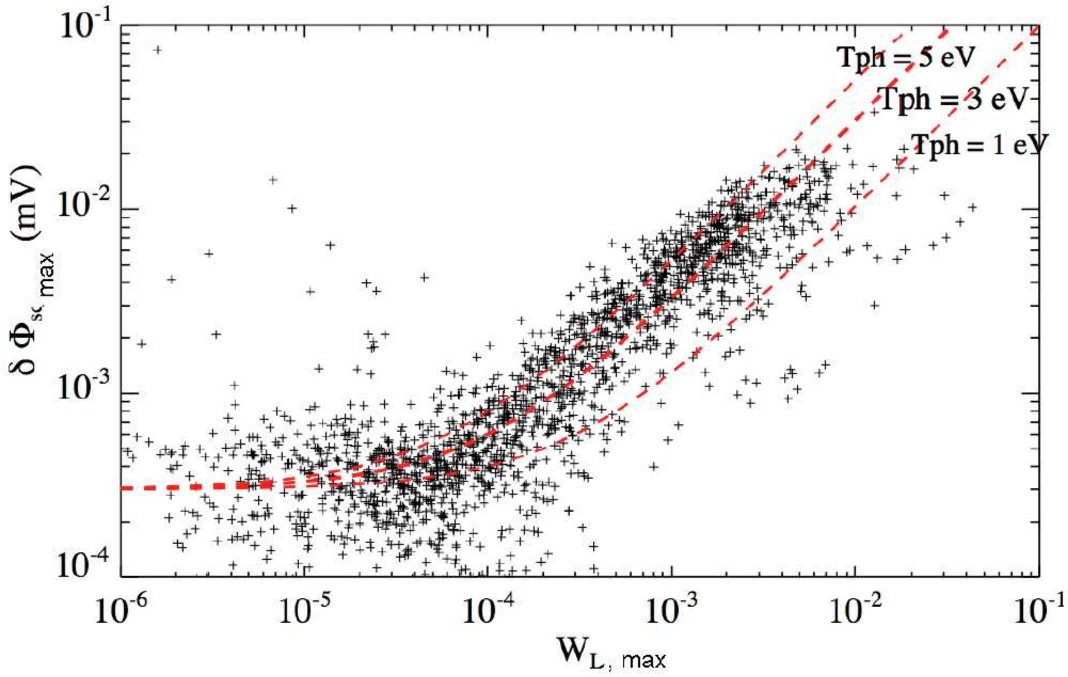

Figure 2.9: Fluctuations of potential $\delta\Phi_{sc,max}$ simultaneous to Langmuir oscillations of normalized energies $W_{L,max}$. The dotted lines show the expected level of density fluctuations generated by Langmuir ponderomotive effects, associated to $\delta\Phi_{sc,max}$ via Eq. (A.10, for different T_{ph}.

small scales, into the kinetic range, by a turbulent cascade (54; 56) , (27; 65; 66). In this classical scenario of magnetohydrodynamic turbulence, fluctuations in the plasma are driven at some large "outer" scale and decay by interacting locally in k space. Eddies at some scale k^{-1} exchange energy with eddies at nearby spatial scales with the resulting net flow of energy to smaller spatial scales (larger k); this cascade of energy occurs over an "inertial subrange" of k–space and it was shown (56) to predict a power spectrum that scales as $k^{-5/3}$ (Fig. 2.10). As the scales of the fluctuations reach the proton kinetic range, the observed properties of the solar wind turbulence start to change (showing the presence of a spectral break at scales of the order of the *ion–cyclotron frequency* f_{ci}, where f_{ci}=0.1 Hz at 1 AU) (57; 55; 58; 59; 40), ions become demagnetized and the plasma can no longer behave as a simple fluid, thus the fluid description breaks down and kinetic representation is needed. At these scales, the turbulent fluctuations can be dissipated and heat the solar wind (60), (61; 62) (64; 67; 68; 63), but the details of this damping process are not known and there are few reported measurements in this regime of k space.

The occurrence of a nonlinear energy cascade and the Kolmogorov's energy spectrum both depend on the existence of a dissipative process working at small scales. In classical turbulence viscosity provides that dissipation, but the collisionless character of the solar wind plasma requires some physical mechanisms that provide the necessary dissipation of energy in absence of collisional viscosity and resistivity. Understanding these mechanisms is a step of crucial importance for understanding the

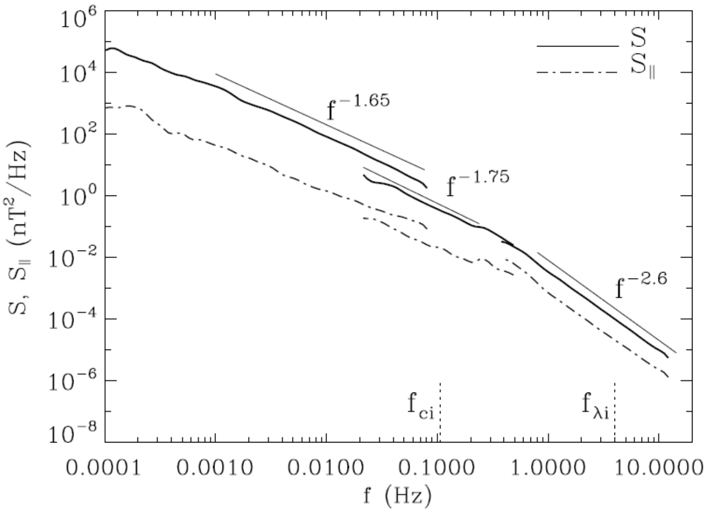

Figure 2.10: Total magnetic field power spectral density S and the spectrum of compressible magnetic fluctuations $S_{||}$ (dash-dotted line) measured by Helios 2 (up to 0.08 Hz) and by Cluster (up to 12.5 Hz) as showed by (138). In the same figure, the straight lines show power-law fits and the vertical dotted lines indicate the ion cyclotron frequency f_{ci} and the Doppler–shifted ion inertial length f_{λ_i} (in the third chapter it will be made use of d_i instead of λ_i to represent the ion inertial lenght).

origin and nature of the solar wind and in the problem of high–frequency turbulence in space plasmas. For those reasons, the study of the short–wavelength (high–frequency) region of the solar wind turbulent cascade represents a subject of recent active interest in space plasma physics. The first analysis of the high–frequency range of the energy spectra in the solar wind (69; 70) revealed a significant level of electrostatic activity at frequencies of the order of few kHz, identified as ion–acoustic fluctuations propagating along the ambient magnetic field (71). Recent observations (59; 73; 74), focused on the analysis of the solar wind data from spacecraft, aiming to investigate how the energy of large–scale Alfvènic fluctuations can be transferred toward short scales and eventually turned into heat, need a better description of the physical processes which allow the energy cascade to make the transition between the fluid–like turbulent behavior at large scales and kinetic effects which happen at very small scales (75; 76). The presence of electrostatic activity beyond f_{ci} has been attributed to Kinetic Alfvèn Waves (KAW) (59; 72) which can eventually be dissipated at frequencies higher than the electroncyclotron frequency $f \geq 100$ Hz (73). However, the picture of the energy cascade is yet controversial, and the role of KAW has been questioned (93; 94). Recently, many authors (77; 78; 79; 80) have used kinetic numerical simulations to reproduce the solar wind phenomenon at short spatial lenght scale, that is, the generation of longitudinal proton–beam velocity distributions associated with the propagation of electrostatic fluctuations. These simulations reproduced the temperature anisotropy in the ion distribution function and indicates the generation of beams of fast ions associated with a strong

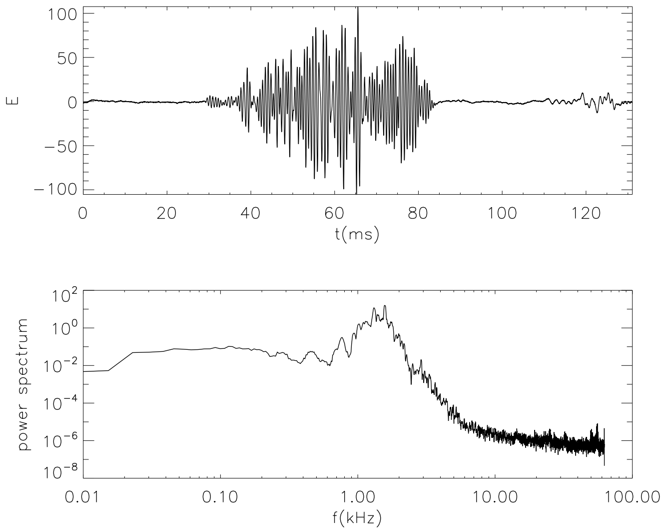

Figure 2.11: An example of the wavepacket observed from S/WAVES onborad STEREO (upper panel), along with the corresponding Fourier spectrum (lower panel). The electric field here is normalized to $E_0 = m_i u_A \Omega_{ci}/e$, m_i being the ion mass, u_A the local Alfvèn speed, Ω_{ci} the local ion–cyclotron frequency and e the electric charge.

electrostatic activity in the short–scale termination of the electric energy spectra at frequencies higher than $f > 10 f_{ci}$. In the following it will presented results coming from a sistematic comparison between high–frequency observations of electric field signals in the solar wind from the STEREO spacecraft with numerical results of hybrid–Vlasov simulations (79; 80; 81). This analysis shows that the high–frequency spectral region, is made by wavepackets of finite extension where fluctuations have sinusoidal, non–sinusoidal and completely irregular waveforms. The systematic comparison of observational datasets with numerical results of the hybrid–Vlasov simulations, shows clear evidences that the observed high–frequency peak is consistent with the excitation of ion–bulk electrostatic fluctuations, resulting from resonant particle trapping associated with velocity distributions of ions that display marked plateaus in the vicinity of the thermal speed, as a consequence of the nonlinear saturation of the wave–particle interaction process.

2.4.1 STEREO WAVES data

We focused on signal detected in the range of frequencies 1 kHz $\leq f \leq$ 5 kHz which are not dominated by local density fluctuations in the low frequency domain (Sect.2.3 and appendix A). We selected and analyzed 3 years data from both STEREO spacecrafts, from 01/2007 to 12/2009, by extracting more than 900 electric wavepakets. In Fig. 2.11 it is reported one of the localized wavepacket of electric activity (top panel) and its associated Fourier power spectrum (lower panel), showing the presence of the electric peak at some few kHz and a broad tail. A carefull analysis of the various

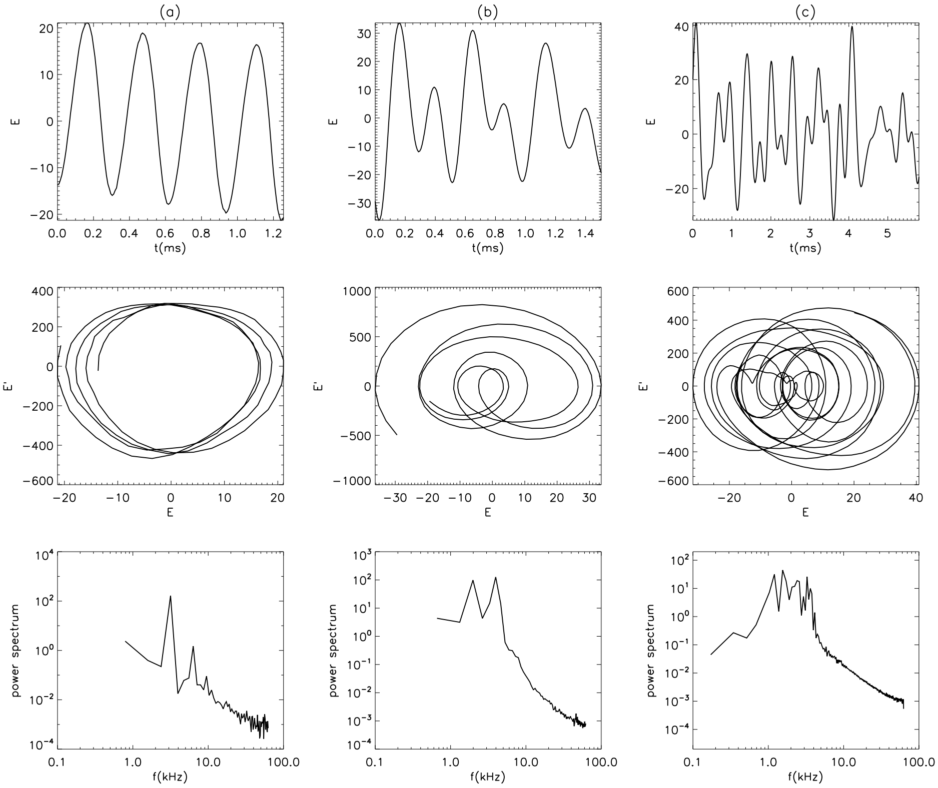

Figure 2.12: The time evolution of the electric field E detected by S/WAVES for three different cases (upper panels). Middle panels report the corresponding phase space dE/dt vs. E, while the lower panels report the Fourier power spectra. The electric field is normalized to $E_0 = m_i u_A \Omega_{ci}/e$.

signals reveals that each wavepacket detected by STEREO is made by a sequence of different waveforms, namely different oscillating behavior of modulated amplitude. We can clearly distinguish periods where the waveform is purely sinusoidal and other periods where it looks periodic but remarkably non-sinusoidal. During the remaining period the waveform is characterized by irregular oscillations, say the amplitude varies stochastically. In Fig. 2.12 three examples of the time behavior of the detected electric field E, along with the relative phase space (E, dE/dt) (middle panels) and the frequency spectra (lower panels) are shown. Of particular interest is the remarkable presence of characteristic periodic non–sinusoidal wavepackets (panels b in Fig. 2.12) which are made by the excitation of secondary harmonics. These oscillations become irregular in time and the high-frequency part of the Fourier spectrum increases (panels c in Fig. 2.12).

2.4.2 Hybrid-Vlasov simulations data

To gain more insight into the origin of the high–frequency electric signals, the wavepackets observed from S/WAVES have been also compared with results of hybrid–Vlasov numerical simulations. The code (78), solves numerically the Vlasov equation for the ion species distribution function $f(\boldsymbol{x}, \boldsymbol{u}, t)$ (electron being treated as a fluid) which in absence of collisions and under the effect of the electric E and magnetic B fields reads:

$$\frac{\partial f}{\partial t} + (\boldsymbol{u} \cdot \nabla) f + \frac{q}{m} \left[\mathbf{E} + \frac{\mathbf{u} \times \mathbf{B}}{c}) \cdot \nabla_{\boldsymbol{u}} f \right] = 0 \tag{2.6}$$

($\nabla_{\boldsymbol{u}}$ being the gradient in the velocity space). The above equation is the same as Eq.1.9, where I removed the subscript α that denoted the species. The Maxwell equations are used to evolve self–consistently the electromagnetic fields. Numerical simulations have been carried out in the 1D–3V phase space (one dimension in physical space and three dimensions in velocity space), discretized using 2048 gridpoints in the physical domain and 51 gridpoints in each direction in the velocity domain. Turbulence is triggered by injecting the energy in Afvènic fluctations at low frequencies (about 10% lower than the ion–cyclotron frequency) and the system evolution is investigated along the energy transfer towards short scales across the ion inertial length. Here we present results obtained using plasma $\beta = 0.5$, amplitude of the pump magnetic field fluctuations $\Delta B/B \simeq 0.5$, and electron to ion temperature ratio $T_e/T_i \simeq$10. However, our results can last even for relatively lower $T_e/T_i \simeq$1 (82) and for lower amplitudes of the pump fluctuations 0.05 $\Delta B/B \simeq 0.2$ (81; 83). The dispersion relation obtained from the numerical signals (Fig. 2.13) shows two branches of acoustic type electrostatic waves. Apart for the usual ion–acoustic waves, the new branch of electrostatic waves, identified as ion–bulk waves (78; 79), present phase velocity close to the ion thermal speed. The excitation of these waves is due to the generation, through resonant interaction of ions with ion-cyclotron waves (86), of diffusive plateaus in the longitudinal velocity distribution. As the result of this process, short wavelength packets are recovered in the electric field component parallel to the ambient magnetic field. The hybrid simulation results in sequences of different wavepackets of finite duration, one of them is reported in Fig. 2.14 along with the corresponding Fourier power spectrum. A comparison with observations shows that they should correspond to a ion–cyclotron frequency of about $\Omega_{ci} \simeq 50 \div 100$ Hz. Even in this case, a careful analysis of each wavepacket shows the presence of signals of small duration which looks similar to what is observed through S/WAVES, as reported in Fig. 2.15. In the example reported here the sinusoidal waveform shows a peak at a frequency of about $\omega \simeq 50\Omega_{ci}$. A comparison with observations results in $\Omega_{ci} \simeq 60$ Hz for solar wind plasma. As reported above for real data, a non–sinusoidal periodic signal is due to two dominant harmonics in the Fourier power spectrum, while the irregular case involves the enhancement of a high–frequency broad spectrum. From the comparison between spacecraft data and numerical results, one notices that the amplitude of the electric fluctuations detected from observations is larger than that recovered in the simulations. These differences can be due to the fact that the numerical model can describe only a limited portion of the complex phenomenology that drive the turbulent cascade in the real solar wind plasma. Due to computer limitations, actual numerical simulations cannot describe frequencies as high as that observed from spacecrafts, and

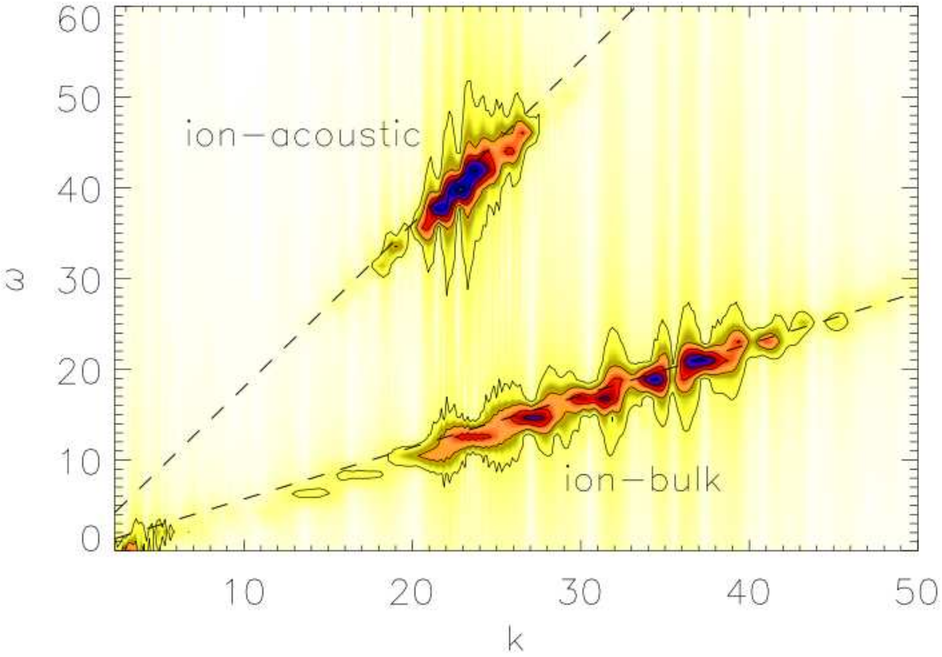

Figure 2.13: $k - \omega$ spectrum of the parallel electric energy for a simulation with T_e/T_i= 10. It can be distinguished two different branches of acoustic waves, the IA waves (upper branch) and the IBk waves (lower branch). The upper dashed line represents the theoretical prediction for the ion–sound speed c_s (3), while the lower dashed line represents the IBk waves phase speed.

the evolution of the electrostatic component of the simulated short–scale spectrum is crucially affected by the numerical dissipation.

Waveforms similar to that found in the solar wind small–scale turbulence of Fig. 2.12 and in hybrid–Vlasov simulations of Fig. 2.15 represent a property of modulated non–linear waves. They can be obtained for example by using a simple model obtained from a two–fluids description of plasma with an external source of ions. This model, which results in a Van der Pol equation (85; 88; 87; 92), describes self–oscillations of plasma with an amplitude that exibits spontaneous exponential growth, resulting from a ion-beam instability, followed by a stabilization due to wave-wave coupling nonlinear saturation. A brief explaination of the model and a some results of the numerical integration of its equations are showed in appendix B

2.4.3 Conclusions

In conclusion, we investigated small–scale turbulence in the interplanetary space which is characterized by an high level of fluctuations. Even if the available instruments onboard spacecrafts do not allow us to access informations at high–frequencies on the particle velocity distributions associated with these fluctuations or on the specific polarization properties of fields, a systematic comparison of the observed peaks

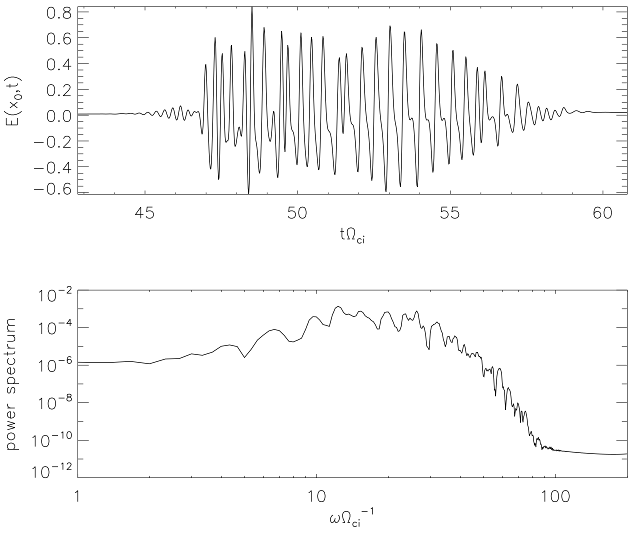

Figure 2.14: An example of the wavepacket of hybrid–Vlasov numerical simulations detected at a given spatial point x0 (upper panel) along with the corresponding Fourier power spectrum (lower panel).The electric field is normalized to $E_0 = m_i u_A \Omega_{ci}/e$.

at few kHz with those obtained in hybrid-Vlasov numerical simulations succeeds in identifying the small–scale wavepackets as due to ion–bulk electrostatic fluctuations, associated with velocity distributions of ions that display marked plateaus in the vicinity of the thermal speed. The small scale electrostatic fluctuations observed in solar wind turbulence represent one of the the way turbulent energy, cascading from large-scales, is finally "dissipated" in a collisionless plasma.

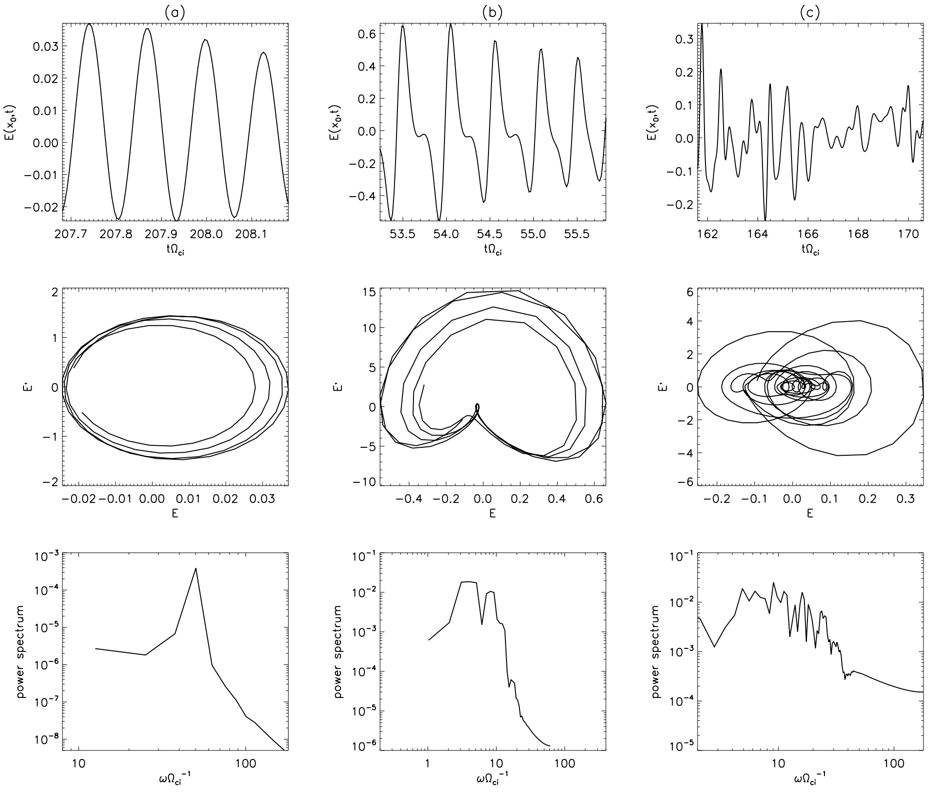

Figure 2.15: The time evolution of the electric field E from hybrid–Vlasov numerical simulations for three different cases (upper panels). Middle panels report the corresponding phase space dE/dt vs. E, while the lower panels report the Fourier power spectra. The electric field is normalized to $E_0 = m_i u_A \Omega_{ci}/e$

CHAPTER 3

Magnetic Reconnection as an element of Turbulence

In the introduction, I reported the fact that most of the Universe is in the state of plasma that is nearly always found to be magnetized and turbulent. The existence of this magnetic fields in the presence of plasma flows inevitably leads to the process of magnetic reconnection, in fact, when twisted or sheared, the megnetic field lines may break and reconnect rapidly, converting magnetic energy into heat, kinetic energy, and fast–particle energy. Magnetic reconnection is a process that occurs in many astrophysical and laboratory plasmas (95; 97; 98). Systems like the solar surface (99), the magnetosphere (96), the solar wind (100; 102; 101), the magnetosheath (103; 104), and laboratory plasmas (105; 106; 108) represent just some of the classical systems in which magnetic reconnection occurs (in Fig. 3.1 two of the most known situation in which magnetic reconnection takes place in space plasma, solar flares and the reconnection in the Earth magnetoshere). Another underlying common feature of the above systems is the presence of turbulence (109), so a simultaneous description of both reconnection and turbulence is needed. In turbulence, magnetic reconnection may behave in a less predictable way. Reconnection in turbulence is a very fascinating topic of research, but only recently a quantitative study of reconnection in turbulence has been presented (120; 121). It was showed that multiple–reconnection events are present in turbulence and their properties depend on the topology of the magnetic field and the local turbulence condition. Again, turbulence provides a kind of unbiased and natural local boundary condition for reconnection, producing much faster reconnection events than one would expect from laminar experiments. Although the combined effects of turbulence and reconnection are likely to be important in a variety of physical systems, the investigations that will be to described in the following are carried out in the limited context of incompressible MHD, for which the turbulence problem, as well as the well–resolved reconnection problem, are already very demanding. First, it will be explained the process of reconnection during turbulent relaxation, following in time the dynamics of 2D MHD turbulence and characterizing the statistical properties of the dynamical system. After this part, it will be shown the statistical study of magnetic reconnection events in two–dimensional turbulence comparing numerical simulations of magnetohydrodynamics (MHD) and Hall magnetohydrodynamics (HMHD). In fact, besides turbulence (124), another ingredient that may accelerate the process of reconnection is the Hall effect (144; 145). In particular, it has been proposed that the Hall effect in reconnection causes a catastrophic release of magnetic energy,

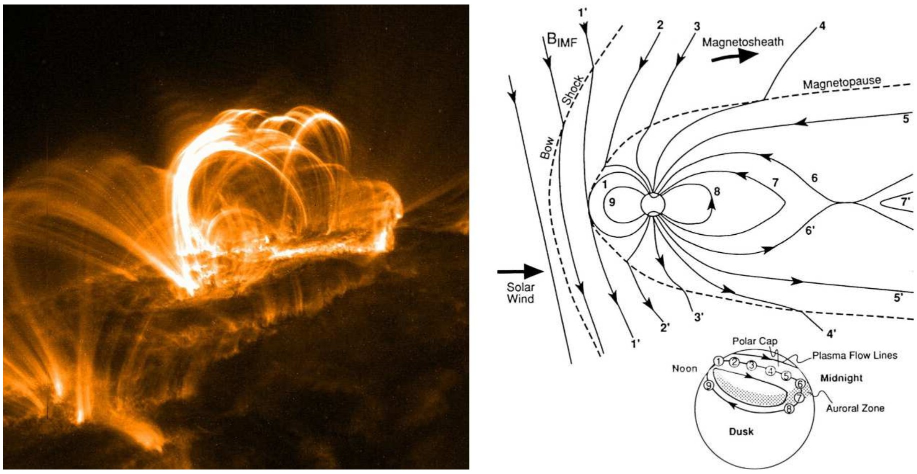

Figure 3.1: Left: Solar flare image as obtained by the TRACE satellite (from apod.nasa.gov). Right: Schematics of magnetic reconnection in the magnetoshepe (from (126))

leading to fast magnetic reconnection onset (125), with reconnection rates faster than the Sweet–Parker expectation. The objective of this work was to combine the above ideas, namely that reconnection is locally enhanced by both turbulence and by the Hall effect, investigating the statistics of magnetic reconnection in 2D Hall magnetohydrodynamic (HMHD) turbulence. Using high resolution pseudo–spectral numerical simulations, it will be compared the statistical properties of reconnection in MHD and HMHD turbulence, by increasing the strength of the Hall effect. In the next sections, there will be the description of the magnetic reconnection from a theoretical point of view (Sect. 3.1), illustrating the main ideas behind the reconnection process and the basic equations, then, in Sect. 3.2, the overview of the main features of 2D MHD simulations in turbulence, the methodology and the statistical analysis of reconnection, establishing a link between length–scales in turbulence and the diffusion region geometry. Then, in Sects. 3.3-3.4, it will be shown results of a MHD simulation in time to show how much turbulence influence the reconnection process and, finally, the results coming from a comparison between the MHD and the HMHD simulations, together with the new features produced by the Hall physics.

3.1 The physics of magnetic reconnection

The idea of magnetic reconnection first originated in the attempts to understand the heating of the solar corona and the origin of the enormous energy observed in solar flares in which it appeared that energy was first slowly built up and stored in the magnetic field, and then suddenly released into thermal and kinetic energy. It was recognized (110; 111) that magnetic X points can serve as locations for plasma heating and acceleration in solar flares. In particular Giovanelli showed that the changing field strengths in the sunspot fields would produce large voltages that were capable of accelerating charged particles to high energies. Some years after, Cowling (112) pointed out that, if a solar flare is due to ohmic dissipation, a current sheet is needed to power it. Then, Dungey (113) showed that such a current sheet can indeed form by the collapse of the magnetic field near the X point and was the first to introduce the concept of brokening and rejoining of the field lines. Some years after the above pioneering works, Parker (115) and Sweet (114) developed an MHD model to describe steady–state reconnection in a current sheet formed at a null point. Their proposal was to apply the model to solar flares, considering a magnetic field with an X–point produced by sources in the photosphere. They showed that the problem was essentially a boundary layer problem, and they estimated the rate of reconnection from a boundary layer analysis. This analysis shows the release of magnetic energy over a period of time several orders of magnitude longer than the observed, so the Sweet–Parker model represent a model for slow reconnection. In 1964, Petschek (116) developed an alternative model where the lenght of the current sheet was many orders of magnitude lower than that in the Sweet–Parker model. For this to happen, the rest of the boundary layer region should consist of slow shocks that could accelerate the matter that did not pass through the diffusive region. In this case, the predicted reconnection rate is close to the rate needed in solar flare. Petschek model was the first model of fast reconnection to be proposed. Since then, a new generation of more general uniform and non–uniform model has been developed. During the past decades, progress in understanding the physics of magnetic reconnection has been made using space and astrophysical observations, theory and numerical simulations, and laboratory experiments. Space and astrophysical observations (96; 100; 102; 103) have provided evidence that magnetic reconnection plays an important role in natural plasmas and generated strong motivations for fundamental research. Theory and numerical simulations provide insights to help in breaking down the complex reconnection phenomena into a set of simpler processes and to gain improved physics understanding of each process, even if, usually, breaking a problem in subsets of smaller problems gives as consequence further complications in understanding the phenomenology. Magnetic fusion experiments provide examples of magnetic reconnection through selforganization of their configurations.

Magnetic reconnection is a process occurring at the boundary between two magnetized plasmas where the *frozen–in* condition for the magnetic field breaks down, more specifically in a region of plasma where the magnetic field changes direction over a finite distance, implying the existence of a current sheet in this region. This current sheet can become unstable, allowing the sheared field lines to effectevely annihilate by cross connecting, which release heat and accelerates the plasma to high velocities. The above violation is described in the framework of Magnetohydrodynamics introduced in the first chapter, that is, the plasma in magnetic reconnection processes is treated as a conductive fluid and no distinction is made between the dynamics of ions and electrons and we will limit to the case of collisionless plasma. This choice is justified by the fact that many of the enviroment in which reconnection occurs are plasmas where the mean–free path for binary collision is much greater than the characteristic scale–lenght of the system.

3.1.1 Magnetic reconnection : equations and the Sweet–Parker model

A magnetic field is viewed as emerging from and embedding in a heavy conducting plasma on two parallel surfaces separated by a substantial length. At one or both ends the field lines are dragged around by a convective motion in the plane, and the highly conducting but more rarefied plasma between the planes responds dynamically. This is usually modeled using magnetohydrodynamics or Reduced magnetohydrodynamics (RMHD). In the MHD approximation, all bulk plasma flow at velocity $\boldsymbol{u} = c\boldsymbol{E} \times \boldsymbol{B}/B^2$ is due to the drift introduced by the $\boldsymbol{E} \times \boldsymbol{B}$ term. From the condition in which there's no distinction between different species dynamics, electrons and ions flow at the same speed and this gives, for the current, $\boldsymbol{j} \ll ne\boldsymbol{u}$. In presence of a finite conductivity σ the equation that govern the magnetic field (the induction equation Eq. (1.21) is given by:

$$\frac{\partial \boldsymbol{B}}{\partial t} = \nabla \times (\boldsymbol{u} \times \boldsymbol{B}) + \frac{1}{\mu_0 \sigma} \nabla^2 \boldsymbol{B} \tag{3.1}$$

where, as said in section 1.2.2, the ratio between the *convective* term and the *diffusive* term (respectevely, first and second term in the right hand side) define the *magnetic Reynolds number*, $R_m = \mu_0 \sigma L_0 U_0$. Recall that the electric field comes from the Ohm's law and it is equal to $\boldsymbol{E} = \boldsymbol{j}/\sigma - \boldsymbol{u} \times \boldsymbol{B}$. The conductivity σ in Eq. (3.1) depends on the rate of collisions, so that, in absence of the latter, σ results infinite and the diffusive term is zero giving the condition of *frozen–in* for the magnetic field in an infinitevely conductive plasma. The mathematical formulation stay in the reduced equation for $\boldsymbol{E}$ and $\boldsymbol{B}$:

$$\boldsymbol{E} = -\boldsymbol{u} \times \boldsymbol{B} \tag{3.2}$$

$$\frac{\partial \boldsymbol{B}}{\partial t} = \nabla \times (\boldsymbol{u} \times \boldsymbol{B}). \tag{3.3}$$

From this condition, the magnetic flux through a closed curve (bounding a surface S) does not change, that is if the curve moves or compress, the magnetic field moves or compress with it (to illustrate this condition we can look at Fig. 3.2). When frozen–in condition apply, all plasma elements and all magnetic flux contained at a given time in a magnetic flux tube will remain inside the same flux tube at all later times :

$$\int_S \boldsymbol{B} \cdot \boldsymbol{dS} = \int_S [\partial \boldsymbol{B}/\partial t - \nabla \times (\boldsymbol{u} \times \boldsymbol{B})] \cdot \boldsymbol{dS} = 0. \tag{3.4}$$

During frozen–in there is a conservation of the local topology of the magnetic field lines for which two elements connected at the same field line, at $t = t_0$ line, will lie on it also at later time though the magnetic field lines are deformed by the plasma flow. In addition, the velocity of magnetic field lines ($\boldsymbol{v} = \boldsymbol{E} \times \boldsymbol{B}/B^2$) is equal to the velocity of plasma elements and any component of the electric field $E_{||}$ parallel to

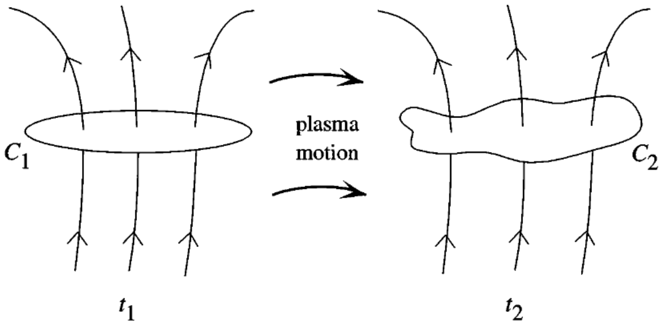

Figure 3.2: Schematics of the frozen–in condition : the flux through C_1 at t_1 equals the flux through C_2 at t_2 (image from (117))

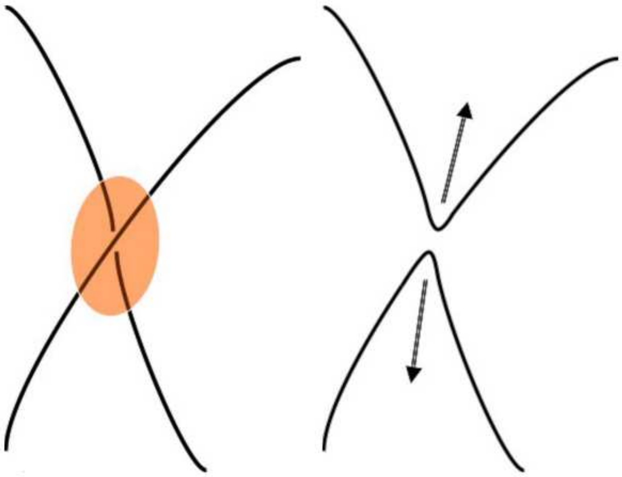

Figure 3.3: Schematics view of 2D magnetic reconnection (image from (107))

the magnetic field direction must vanish. When the magnetic reconnection is going on, in a little region of plasma, namely *diffusion region*, the frozen–in condition is violated and earlier separated magnetic fields lines, with different topoligies, get interconnected at an X–point, where they break and reconnect forming new field lines with a diffwerent topology from the initial ones (in Fig. 3.3 the schematic 2D view of the process). The change of magnetic topology and connectivity of plasma elements is due to the presence of a parallel electric field $E_{||}$ within the diffusion region, and there is also the acceleration of plasma in form of heated reconnection jets due to the transformation of the magnetic energy partially in kinetic energy and partially in thermal energy of the plasma. Magnetic reconnection is a 3D problems, but the 2D steady–state description provides a good physical insight and it is often consistent with the observations. In this picture (represented in Fig. 3.4), the opposite directed magnetic field lines get interconnected in the X–point located in the center of the diffusion region (the shaded region). The line connecting all the

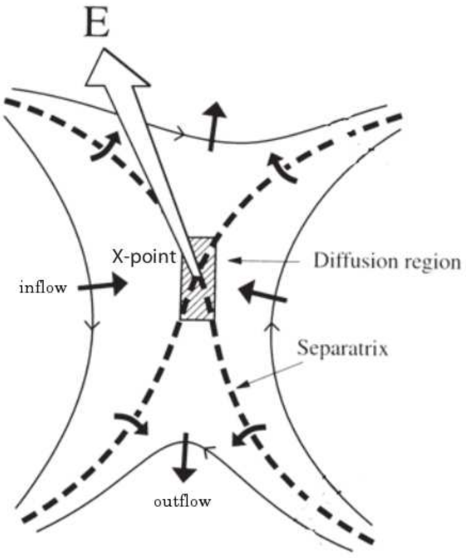

Figure 3.4: Schematics diagram of 2D magnetic reconnection (image adapted from (117))

X–points in the direction out of the reconnection plane is the X–line. The magnetic separatrices are the surfaces separating magnetic fields with different topologies and they intersect in the X–line, while their projection onto the reconnection plane are the magnetic field lines connected to the X–point. Many theoretical models have been proposed to describe the process of magnetic reconnection, but I will present the first one, resulting from the collaboration between Sweet and Parker that, though not always realistic from an observational point of view, illustrate the main properties of magnetic reconnection.

3.1.1.1 Sweet–Parker reconnection model

Parker and Sweet were the first to formulate magnetic reconnection as a local problem in which the inflow of plasma was connected with an outflow from the diffusion region. An example of the Sweet–Parker schematization is represented in Fig. 3.5. Consider two oppositely directed magnetic fields, in a plasma (it is considered in a steady state) with density ρ and conductivity σ, that are carried toward the neutral line at speed $\boldsymbol{u}_{in}$ over a characteristic distance $2L$. At the center of the configuration there is a null point and also a layer of width 2δ in which the field reconnects and is expelled at speed $\boldsymbol{u}_{out}$. The Sweet–Parker theory predicts the reconnection rate ($\boldsymbol{u}_{in}$) and establishes the basic energetics and geometry of the reconnection region based on the following three assumption: (i) The outflow speed is the Alfvèn speed $\boldsymbol{u}_A = \boldsymbol{B}/4\pi\rho$. (ii) Mass is conserved. For an incompressible flow, $\boldsymbol{u}_{in}L = \boldsymbol{u}_A\delta$. (iii) The electric field $\boldsymbol{E}$, given by the resistive MHD form of Ohm's, is perpendicular to the plane of the flow and must be constant in a steady state, i.e. it is inductive everywhere except near the X–point where it is primarily resistive. From the last

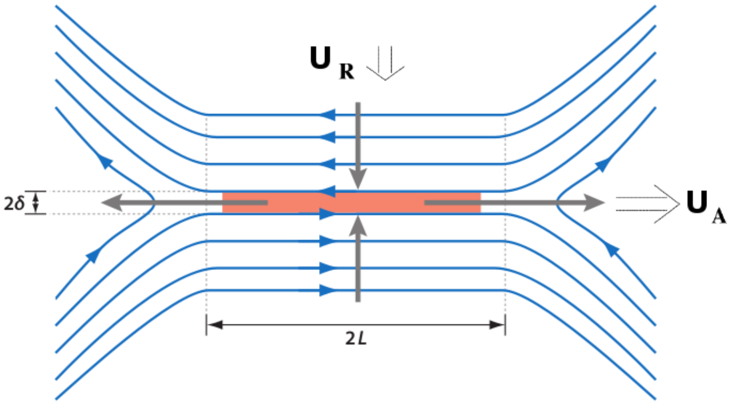

Figure 3.5: Schematization of the Sweet-Parker layer. In a steady state the magnetic diffusion velocity $\eta c/4\pi\delta$ balances the incoming reconnection velocity $\boldsymbol{u}_R$, and the inflowing mass $4\boldsymbol{u}_R L$ balances the outgoing mass $4\delta\boldsymbol{u}_A$.(image adapted from (118))

this statement we have:

$$u_{in}\boldsymbol{B}/c \sim \boldsymbol{j}/\sigma, \tag{3.5}$$

where $\boldsymbol{j} \sim c\boldsymbol{B}/(4\pi\delta)$ comes from the Ohm's law. Introducing the *magnetic diffusivity* $\eta = c^2/(4\pi\sigma)$ we obtain an important results of the model:

$$\frac{\delta}{L} = \frac{\boldsymbol{u}_{in}}{\boldsymbol{u}_A} = S^{-1/2}, \tag{3.6}$$

where S is the Lundquist number that is the same as the magnetic Reynold's number R_m with the velocity taken as the Alfvèn velocity. From the energetic estimation of the Sweet–Parker reconnection it can be showed that the Poynting flux (that represent the inflow rate of electromagnetic energy) into the layer is of the same order as both kinetic energy flux out of the layer and the Ohmic dissipation rate inside the layer, so, roughly speaking, during reconnection magnetic energy is converted half to plasma kinetic energy and half to thermal energy. Problems comes out when the expected reconnection rate is compared with real astrophysical rate of reconnections. Most astrophysical systems have very large S, while in the model, because the size of the reconnection region is equal to the whole size of the diffusion region and all the plasma must go through the diffusion region to be accelerated, reconnection is quite slow (corresponding to low S) and the reconnection rate is often not realistic.

3.2 Overview on 2D MHD turbulence

Recognizing that reconnection is an ongoing and statistical aspect of a turbulent medium, and with modern computers having the resources to study these effects, Servidio et al. (120; 121) introduced a direct quantitative study of the reconnection that occurs in turbulence. The approach was to simulate 2D MHD turbulence in a parameter regime in which there are many magnetic islands with the goal of identifying the basic physical principles at work in the turbulence–reconnection dynamical system. From these conclusions started this reserch works in the context of reconnection in turbulence. In the following, it will be explained the main aspect of the 2D MHD simulated dynamical system, how to identify local reconnection in turbulence with a step–by–step analysis and show the link between magnetic reconnection and turbulence. First of all, it is necessary to introduce the equations of the 2D incompressible MHD. It was chosen a uniform density, $\rho = 1$, and the set of equations, that could be written in terms of the magnetic potential $a(x, y)$ and the stream function $\psi(x, y)$, read:

$$\frac{\partial \omega}{\partial t} = -(\boldsymbol{u} \cdot \nabla)\omega + (\boldsymbol{b} \cdot \nabla)j + R_\nu^{-1}\nabla^2\omega \tag{3.7}$$

$$\frac{\partial a}{\partial t} = (\boldsymbol{u} \cdot \nabla)a + R_\mu^{-1}\nabla^2 a \tag{3.8}$$

where the magnetic field is $\boldsymbol{b} = \nabla a \times \hat{z}$, the velocity $\boldsymbol{u} = \nabla\psi \times \hat{z}$, the current density $j = \nabla^2 a$, and the vorticity $\omega = \nabla^2\psi$. Eqs. (3.7-3.8) are written in Alfvèn units (124) with lengths scaled to L_0 (a typical large scale length such that the box size is set to $2\pi L_0$). Velocities and magnetic fields are normalized to the root mean square Alfvèn speed u_A and time is scaled to L_0/u_A. R_μ and R_ν are the magnetic and kinetic Reynolds numbers, respectively (at scale L_0). Eqs. (3.7-3.8) are solved in a periodic Cartesian geometry using a well tested dealiades (2/3 rule) pseudospectral code (127). It was employed a standard Laplacian dissipation term with constant dissipation coefficients. The latter are chosen to achieve both high Reynolds numbers and to ensure adequate spatial resolution. A detailed discussion of these issues has been given by Wan et al. (129). It will be reported on runs with resolution of 4096^2 with Reynolds numbers $R_\nu = R_\mu = 1700$ evolved using a time integration of the second order Runge-Kutta in double precision. Energy, initially, is concentrated in the shell with $4 \leq k \leq 10$ (the wavenumber k is in unit of $1/L_0$) with mean value $E = (1/2)\langle|\boldsymbol{u}^2| + |\boldsymbol{b}^2|\rangle \simeq 1$ ($< \dots >$ means spatial average), and we choose the same initial value for kinetic and magnetic energy. The statistical analysis was performed at the time in which the turbulence is fully developed, that is the state of the system at which the mean square current density $\langle j^2\rangle$ is very near to its peak value. Computing the omnidirectional power spectra, since turbulence is homogeneous and isotropic, it can be seen in (Fig. 3.6) that appears of a broad inertial range, typical of turbulence. When turbulence is fully developed, coherent structures appear and they can be identified as magnetic islands (or vortices). A typical complex pattern of 2D MHD turbulence is shown in Fig. 3.7 where it is represented a contour plot of the current j, together with the in–plane magnetic field (line contour of a). As it can be seen, the current density j becomes very high in narrow layers between islands. The current results bursty in space (see Fig. 3.8 that represent a zoom into the turbulent field) and this is related to the intermittent nature of the magnetic field (130; 131) and can be interpreted as a consequence of fast and local relaxation processes (119). Both the magnetic and velocity fields in

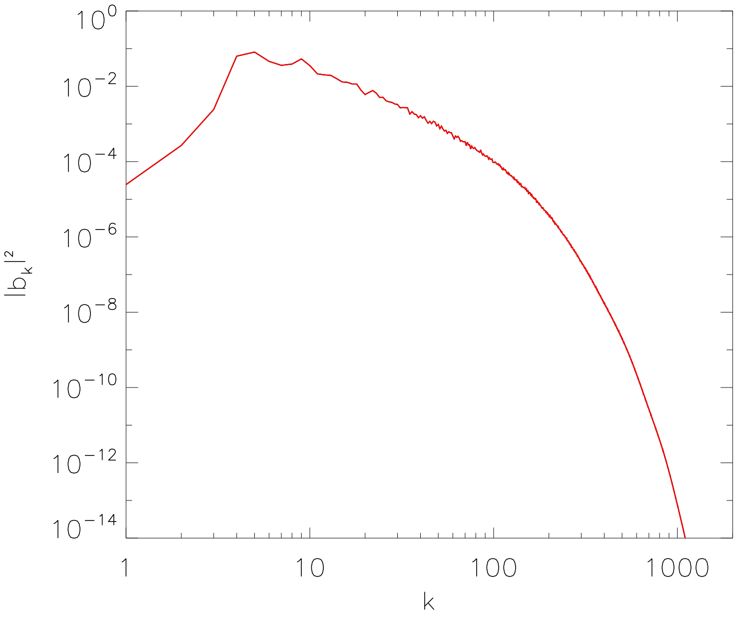

Figure 3.6: Power spectra of magnetic fied.

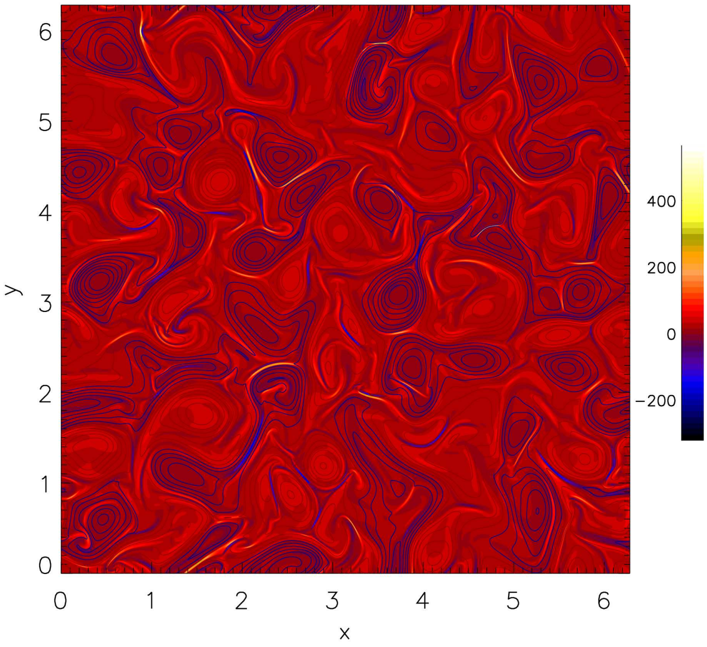

Figure 3.7: Shaded contour of the current j_z togheter with the line contour of the magnetic potential a.

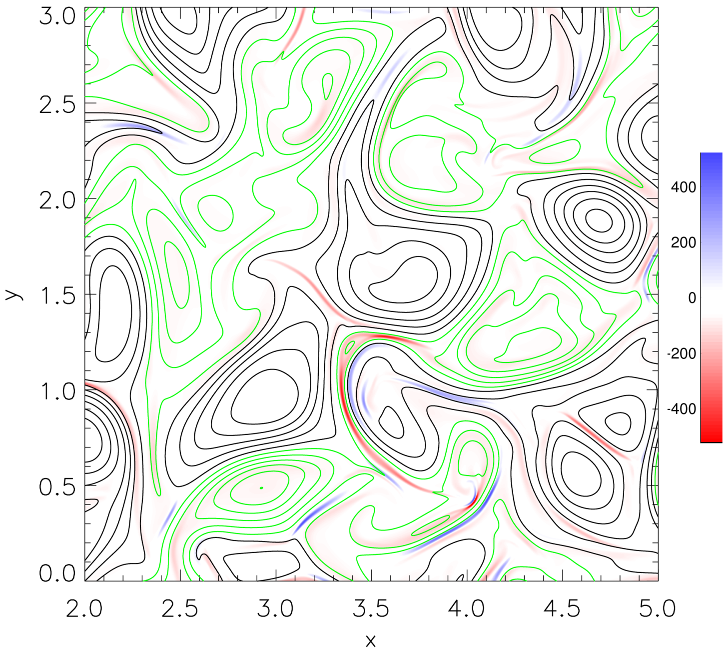

Figure 3.8: Current density profile j_z in a sub-region of the simulation box. The magnetic flux a is also represented as a line contour. As expected in 2D turbulence, strong and narrow peaks of current density are present between magnetic islands.

MHD show a strong tendency to generate increasing levels of phase coherence at smaller scales (128). Between these interacting islands the perpendicular (out-of-plane) component of the current density j_z becomes very high, as it can be seen in Fig. 3.9 and its probability distribution function (PDF) show enhanced tails. The magnetic structures that characterize the turbulent pattern interact non–linearly, merge, stratch, connect, attract and repulse each other. Reconnection is a major elements of this complex interaction.

3.2.1 Local reconnection in turbulence

To understand reconnection in 2D turbulence, we need to examine the topography of $a(x, y)$ and the reconnection rates in detail. In particular we need to identify the neutral points. To this end we examine the Hessian matrix with the second–order partial derivatives of the potential a defined as :

$$H_{i,j}(\boldsymbol{x}) = \frac{\partial^2 a}{\partial x_i \partial x_j}. \tag{3.9}$$

At each neutral point, i.e. where $\nabla a = 0$, we compute the eigenvalues of $H^a_{i,j}$. If both eigenvalues are positive (negative), the point is a local minimum (maximum) of a (an O–point). If the eigenvalues are of mixed sign, it is a saddle point (an X–point).

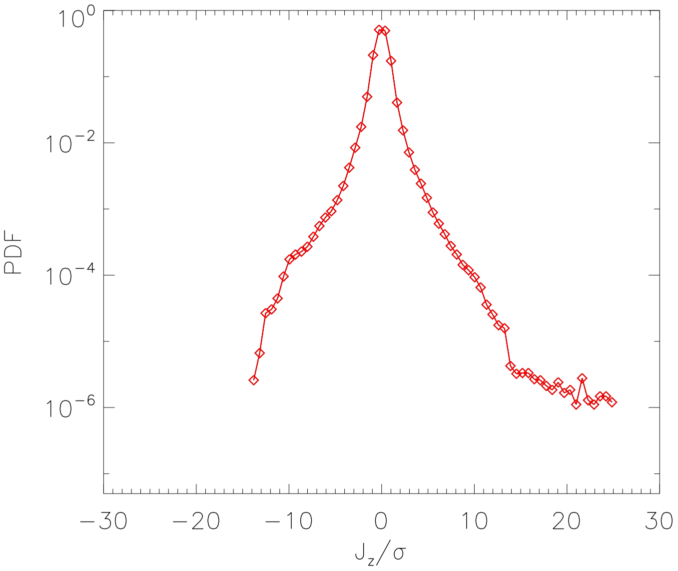

Figure 3.9: PDF of j_z, normalized to its own rms value. The longer tails present are the signature of intense small-scale activity, due to the intermittent nature of the magnetic field.

Because of the complex topology of turbulence, critical points can be very close to each other, they are usually not located on the vertices of a chosen computational grid. This affects the precision of the interpolation technique, producing false critical points. To avoid this inconvenience we make use of a *Fourier zero-padding and interpolation* technique. See Refs. (120; 121) for more details on this analysis. The step–by–step procedure could be summarized as follow:

1. Identify critical points ($\nabla a = 0$) at x^*.

2. Compute the Hessian matrix at x^*.

3. Compute eigenvalues λ_1 and λ_2 of $H^a_{i,j}(x^*)$, with $\lambda_1 > \lambda_2$.

4. Classify the critical points as maximum (both $\lambda_i < 0$, minimum (both $\lambda_i > 0$ and X–points ($\lambda_1\lambda_2 < 0$).

5. Compute eigenvectors at each X–point. The associated unit eigenvectors are $\hat{e}_s$ and $\hat{e}_l$, where coordinate s is associated with the minimum thickness δ of the current sheet, while l with the elongation ℓ. It is important to note that the local geometry of the diffusion region near each X–point is related to the

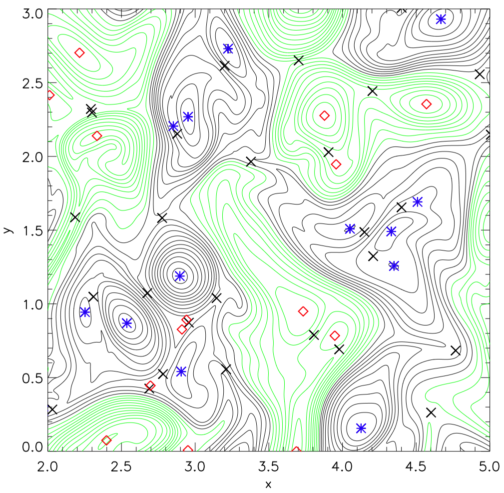

Figure 3.10: Line-contours of of the magnetic potential a in a sub-region of the simulation box. The position of the critical points is reported as well: O-points (blue stars for the maxima and open red diamonds for the minima) and X-points (black $\times$). Magnetic reconnection locally occurs at each X-point.

Hessian eigenvalues, in particular

$$\lambda_1 = \frac{\partial^2 a}{\partial s^2}, \tag{3.10}$$

$$\lambda_2 = \frac{\partial^2 a}{\partial l^2}. \tag{3.11}$$

In Fig. 3.10 an example of a magnetic potential landscape together with its critical points, obtained with the above procedure, is reported for a subregion of the simulation box. From a scaling analysis of the Eqs. for (3.10–3.11), the aspect ratio of the diffusion region can be well approximated by

$$\frac{\ell}{\delta} \simeq \sqrt{\lambda_R} \quad where \quad \lambda_R = |\frac{\lambda_{max}}{\lambda_{min}}|. \tag{3.12}$$

Once we obtained the position of all the critical points, a precise way to measure the reconnection rate of two islands is to compute the electric field at the X–point. This is related to the fact that the magnetic flux in a closed 2D island is computed as the integrated magnetic field normal to any contour connecting the central O–point with any other specified point. Choosing that point to be an X–point bounding the island, we find that the flux in the island is just $a(O - point)a(X - point)$ (132). Flux is always lost at the O–point in a dissipative system, so the time rate of change in the flux due to activity at the X–point is

$$\frac{\partial a}{\partial t} = -E_{\times} = (R_{\mu}^{-1} j)_{\times}, \tag{3.13}$$

where $E_\times$ and $j_\times$ represent, respectively, the electric field and the current measured at the X–point. The expression for the electric field comes from the Ohm's law, $\boldsymbol{E} = -\boldsymbol{u}\times\boldsymbol{b}+R_\mu^{-1}\boldsymbol{j}$, from which we take the z component (note that at the X–point the component $(\boldsymbol{u}\times\boldsymbol{b})_z$ is smaller compared with the current component). The distribution of the evaluated reconnection rates PDF($|E_\times|$) is shown in Fig. 3.11 and it can be seen that it is broad and peaked around zero. The mean value of the distribution is $\simeq 0.05$, but there are strong variation from this value, that is reconnection rates are found in the range $|E_\times| \in [10^{-6}, 0.32]$. The typical reconnection rate in turbulence is found to be far higher than what is expected based on a simple global application of the Sweet–Parker rate $E\times \sim R_\mu^{-1/2}$. In the description of the Sweet–Parker model, I show that the rate of reconnection (I recall that it consider the system is in a steady–state) depends on the aspect ratio (Eq. (3.6), defined in our case by λ_R, so it satisfy the scaling

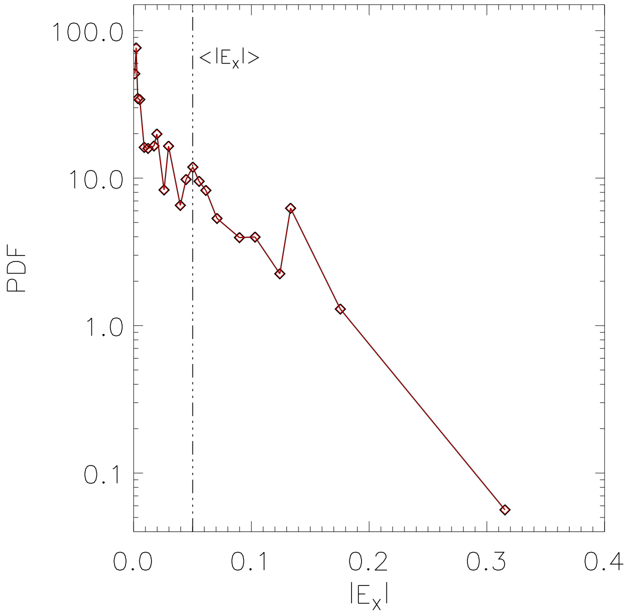

Figure 3.11: Probability distribution function of reconnection rates in turbulence (lin-log scale). Vertical dotted line represents the mean value of the distribution.

$$E_\times \sim \frac{\ell}{\delta} \sim \sqrt{\lambda_R}. \tag{3.14}$$

This trend can be viewed in Fig. 3.12 that is a scatter plot of the reconnection rates against the aspect ratio λ_R. This suggest that locally the reconnection processes depend on the geometry and that therefore are in a quasi steady–state regime. Further details about this analysis on (121).

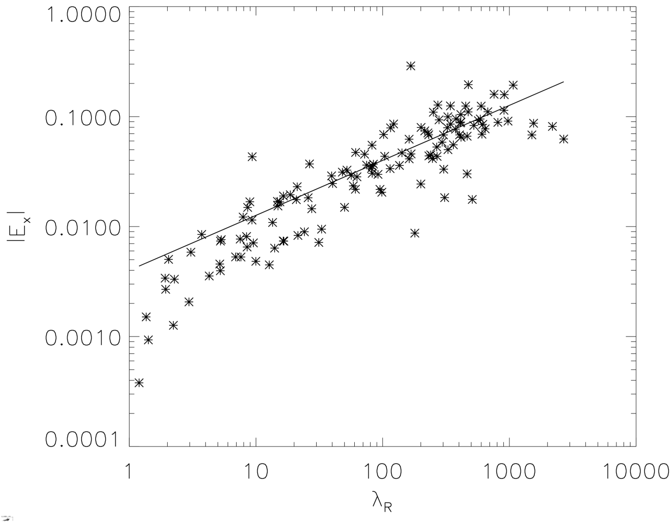

Figure 3.12: The relation between the reconnection rate and the geometry of the reconnection region. The presence of a power-law fit (black solid line) demonstrates that there is a relation between the reconnection rate and the geometry of the diffusion region.

3.2.2 The link between magnetic reconnection and turbulence

To estabilish a link between reconnection and 2D MHD turbulence properties it is necessary to take a closer look at the reconnection sites. Because of the complexity of the geometry we focused only on the X–lines with higher reconnection rates. We needed to find a methodology to quantitatively characterize every reconnection region and extrapolate important information, including δ and ℓ. Since we know the ratio of the eigenvalues (λ_R) obtained from the Hessian matrix analysis, the problem reduces to find just one of these lengths, such as the current sheet thickness δ. The eigenvectors of the Hessian matrix, computed using the above summarized procedure, identify the directions associated with inflow (s) and outflow (l) regions. Once we compute these eigenvectors, it is possible to construct a system of reference for each reconnection region, given by the unit vectors $\{\hat{e}_s, \hat{e}_l\}$ and then evaluate the profiles of δ and for the magnetic field using a fitting procedure. For each X-point the fit has been optimized by an iteration procedure in order to minimize the error of the interpolation. In Fig. 3.13(a) an example of the current density profile along the s–direction is shown. A consequence of the asymmetric nature of turbulent reconnection implies that in most of the cases the current density has a peak not centered precisely on the X-point. Once we have the new reference frame, we call $b_t(s)$ and $b_n(s)$ the tangential and normal component of the magnetic field, respectively, obtained projecting the inplane magnetic field along the direction defined by the eigenvectors:

$$\begin{aligned} \boldsymbol{b}_t &= \hat{e}_l \cdot \boldsymbol{b} \\ \boldsymbol{b}_n &= \hat{e}_s \cdot \boldsymbol{b}. \end{aligned} \tag{3.15}$$

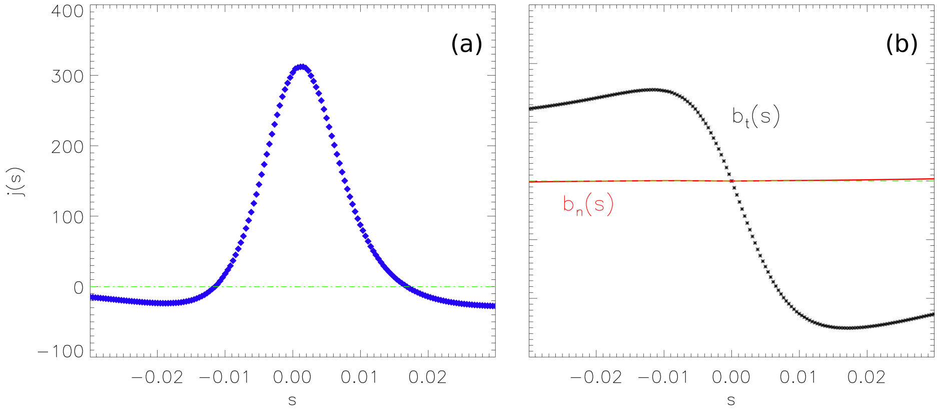

Figure 3.13: Profiles of the current density (a) in the vicinity of a X-point. The X-point is located at s=0. In the panel (b) the tangential (b_t, black) and the normal (b_n, red) components of the magnetic field are shown. Horizontal dashed lines represent zero values.

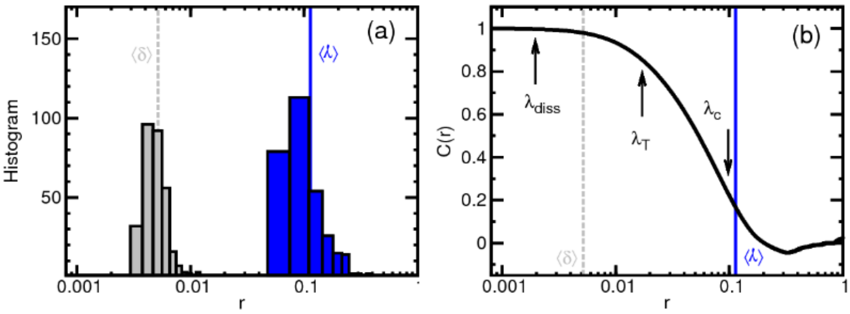

Figure 3.14: (a) histograms of thicknesses (δ, grey bars) and elongations (ℓ, blue bars). (b) the magnetic field autocorrelation function (solid black line) is represented. The arrows (left to right) represent, respectively, dissipation scale λ_{diss}, Taylor microscale λ_T, and correlation length λ_C. Vertical lines are average values $< \delta >$ (dashed grey) and $< \ell >$ (blue solid).

and an example is reported in Fig. 3.13(b). Note that a pile up of the magnetic field, in the upstream region of the reconnection event, is observed (133). Note that, the proces of reconnection in turbulence is often asymmetric (125), so we define δ_1 and δ_2 the left and right part of the current thickness δ ($\delta = \delta_1 + \delta 2$) and two upstream magnetic field b_1 and b_2 (suppriming the subscript t). Then, using the iterating procedure we calculate the lenghts of the diffusion region and the upstream tangential magnetic field. Once obtained, for each strong reconnection event, the dimension of the diffusion region, we evaluate the PDFs of both δ and ℓ, the latter from Eq. (3.14, that are reported in Fig. 3.14(a), showing that they are well separated. To estabilish a link between reconnection geometry and the statistical properties of turbulence, we computed the auto–correlation function of the magnetic field. First, the *correlation lenght*, that represent a measure of the size of the energy containing islands, is defined as

$$\lambda_C = \int_0^* C(\boldsymbol{r}) dr \tag{3.16}$$

where the upper limit is unimportant if the eddies are uncorrelated and the correlation lenght, $C(\boldsymbol{r})$, is expressed as

$$C(\boldsymbol{r}) = \frac{\langle \boldsymbol{b}(x+\boldsymbol{r}) \cdot \boldsymbol{b}(x) \rangle}{\langle b^2 \rangle}. \tag{3.17}$$

In the above equation, $\boldsymbol{r}$ represent the direction of arbitrary displacement for isotropic turbulence in the plane. The auto–correlation function is illustrated in Fig. 3.14(b) as well as $< \delta >$ and $< \ell >$ (reported as vertical lines for comparison). In the plot, indicated by arrows, are also present the *dissipation lenght*, at which turbulence is critically damped, is defined as $\lambda_{diss} = R_\mu^{-1/2} \langle \omega^2 + j^2 \rangle^{-1/4}$, while the *Taylor micro–scale*, the ratio of mean square fluctuations to a measure of the mean square spatial derivatives of fluctuations, is $\lambda_T = \sqrt{\frac{\langle |\boldsymbol{b}^2| \rangle}{\langle j^2 \rangle}}$. From the figure it appears that the average elongation ℓ is strongly related to teh correlation lenght, where the structure function flattens, or, analogously, where $C(\boldsymbol{r} \rightarrow 0$. We found that the values of diffusion layer thickness δ are distributed in the range between the Taylor scale and the dissipation scale, while the length ℓ scales with λ_C . The main features of this ensemble of reconnecting events, including the key length scales, are evidently controlled by the statistical properties of turbulence, setting the range of values of length and thickness of the diffusion regions according to the correlation length and the dissipation scale.

3.3 Time behavior of reconnection in turbulence

In the previous sections I examined the statistics of magnetic reconnection in turbulence, at a given time t^* showing that turbulence is a main ingredient of the magnetic reconnection process. One may ask how the complex pattern of reconnection evolves in time, during the decaying evolution of 2-D MHD turbulence. In the first part of this section, I will answer the above question, showing results from simulation in turbulence for longer times. Once showed these results, I will present in Sect 3.4 a statistically inspection of the role of the Hall effect on the process of reconnection in turbulence.

In analogy with simulations introduced in the previous section, we used a resolution of 4096^2 mesh points, impose random (Gaussian) fluctuations, for both velocity and magnetic fields, in the range $4 < k < 10$, and choose as the final time of the simulation $t = 3.0$. Again, the peak of non–linear activity is reached at $t^* = 0.5$ and all the feature described before are observed. From a macroscopic point of view, during the relaxation process, magnetic islands reconnect, merge, repel, and the system changes its magnetic topology. In Fig. 3.15 the current density is shown for two different times of the simulation. The line–contours of the potential and the position of the X–points are superposed on the same figure. As it can be immediately

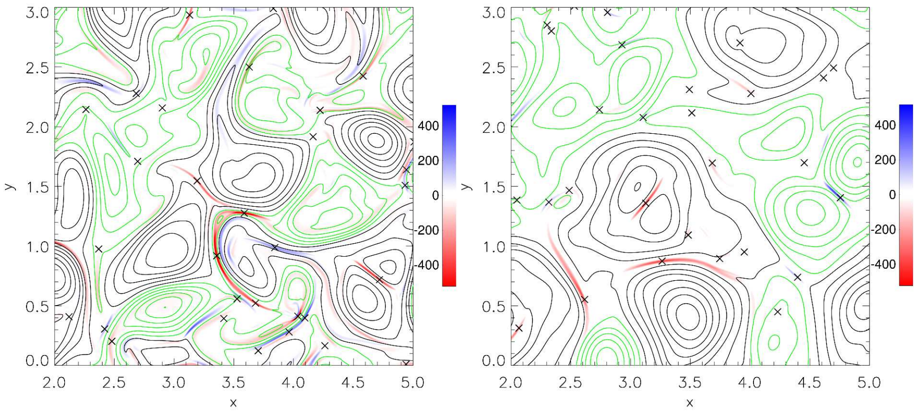

Figure 3.15: Shaded contour of the current density j at different times of the simulations, $t = 0.5$ (left) and $t = 3.0$ (right). Lines contour represent the magnetic potential a, while black crosses indicate the positions of the reconnection events.

noticed, the current sheets reduce both in number and intensity at $t = 3.0$, where the turbulent pattern is characterized essentially by bigger islands. As an example, the number of reconnection sites at $t = 0.5$ is 133, reducing to 114 at the end of the simulation. This process will eventually continue in time until only few X–points survive to the turbulent evolution. Note that is difficult to explore this final stage of the relaxation, since it may occur after thousands of nonlinear times (123). In terms of the reconnection rate, the time behaviour show that these rates are higher when the turbulence activity reach the maximum. This statement results evident looking at Fig. 3.16 where PDFs of reconnection rates (properly normalized to $\delta b_s(t)^2$) at different instants of the simulation are compared, namely at the beginning ($t = 0.0$), at the peak of non–linear activity ($t = 0.5$), at an intermediate time ($t = 1.5$) and at the end of the simulation ($t = 3.0$). This further evidence that fully developed turbulence and fast reconnection events may strongly be related in plasma dynamics. In the preceding section, it was found that the strongest reconnection rates depend on the local geometry of the diffusion region, more precisely the reconnection rate scales with the aspect ratio $\sqrt{\lambda_R} = \ell/\delta$. In Fig. 3.17 it is shown the same scatter plot at different times. At the beginning of the simulation there is no clear scaling, that is related to the fact that initial conditions are Gaussian and there's not coherency in the magnetic field. When the peak of activity is reached ($t > 0.4$) the expectation given by Eq. (3.14) is recovered. At later times, the fastest reconnection events vanish, but the aspect relation is still valid.

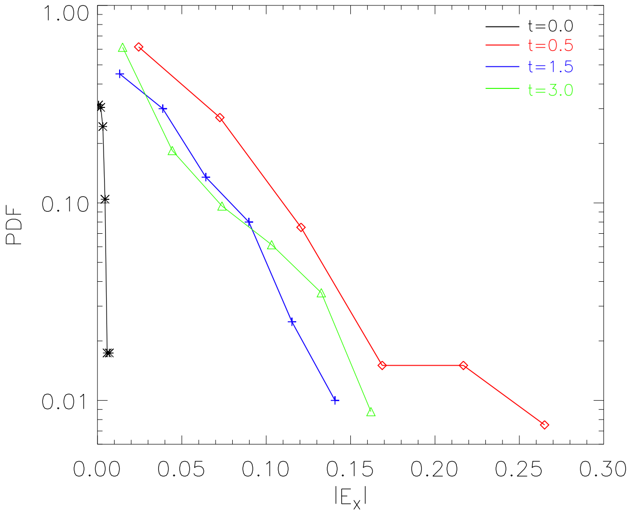

Figure 3.16: Time evolution of the PDF of $|E_\times|$, for $t = 0.0$ (black stars), $t = 0.5$ (red rombus), $t = 1.5$ (blue squares) and $t = 3.0$ (green triangles).

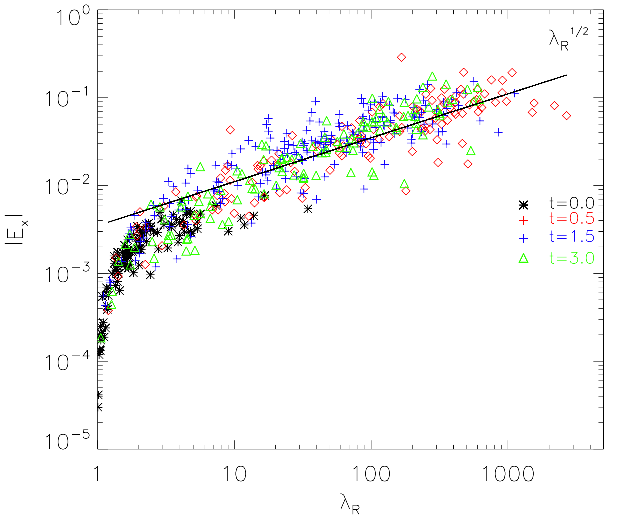

Figure 3.17: Relation between the reconnection rates $|E_\times|$ and the geometry of the reconnection region λ_R, for different times of the simulation. After the peak of non–linear activity is reached, the scaling (solid line) appears.

3.4 The Hall effect in the reconnection process in turbulence

As anticipated in the introduction of the chapter, another important ingredient in the process of magnetic reconnection is the Hall effect. The introduction of the latter in the equations take us in the context of Hall MHD (HMHD hereafter), an extension of the standard MHD where the ion inertia is retained in Ohm's law. In fact, the principal points of distinction between MHD and HMHD lies in the Ohm's law that, with the introduction of the Hall terms, reads :

$$\boldsymbol{E} = -\boldsymbol{u} \times \boldsymbol{b} + \eta \boldsymbol{j} - \frac{(\boldsymbol{j} \times \boldsymbol{b})}{n_e e} \tag{3.18}$$

where n_e is the electron density and e is the electric charge. The last term in the above equation is attributed to the Hall current and cannot exist unless the $\boldsymbol{j} \times \boldsymbol{b}$ force exists. The Hall effect becomes relevant when we intend to describe the plasma dynamics up to length scales shorter than the *ion inertial length* d_i ($d_i = c/\omega_{pi}$, where c is the speed of light and ω_{pi} is the ion plasma frequency) and time scales of the order, or shorter, than the ion cyclotron period ω_{ci}^{-1}. In other words, for large scale phenomena this term is negligible and we recover the standard MHD equations. It is one of the most important manifestations of the velocity difference between electrons and ions when kinetic effects are not taken into account. In the HMHD regime we have field-freezing of the magnetic field to the electron flow, not to the whole bulk velocity flow and, in practical terms, this means that electron motion can be parceled out from the aggregate motion or simplified one–fluid–type motion of standard MHD. Generally, the Hall effect is though to be fundamental for astrophysical plasmas, since it modifies small scale turbulent activity, producing a departure from MHD predictions (134; 135; 136; 137; 93; 138) and, when d_i/L_0 is large enough, changes in the decay rate of the turbulence at moderate Reynolds number (139).. The importance of the Hall effect in astrophysics has been pointed out to understand, for example, the presence of instabilities in protostellar disks (140), the magnetic field evolution in neutron star crusts (141), impulsive magnetic reconnection (142). In the past years, the role of the ion skin depth on reconnection has been matter of several numerical investigations (143; 145; 146). In the following, I will introduce the HMHD incompressible equations and present a global overview of the turbulence properties for all the simulations performed.

3.4.1 Overview of numerical simulations in HMHD turbulence

Analogously to MHD, the equations of incompressible Hall MHD can be written in dimensionless form. In 2.5D (2 dimensions in the physical space for three–dimensional components) the equations read:

$$\frac{\partial \boldsymbol{u}}{\partial t} = -(\boldsymbol{u} \cdot \nabla)\boldsymbol{u} - \nabla P + \boldsymbol{j} \times \boldsymbol{b} + R_\nu^{-1} \nabla^2 \boldsymbol{u}, \tag{3.19}$$

Run	Eqs.	resolution	$R_\mu(R_\nu)$	λ_{diss}	$\epsilon_H(k_H^{-1})$
I	MHD	4096^2	1700	1/196	0
II	HMHD	4096^2	1700	1/195	1/400
III	HMHD	4096^2	1700	1/188	1/100
IV	HMHD	4096^2	1700	1/179	1/50

Table 3.1: Table of parameters of the runs. The second column is the resolution of the simulation, third column the Reynolds numbers, fourth column reports the dissipative scale of the system and the last column shows the Hall parameter.

$$\frac{\partial \boldsymbol{b}}{\partial t} = \nabla \times [(\boldsymbol{u} - \epsilon_H \boldsymbol{j}) \times \boldsymbol{b}] + R_\mu^{-1} \nabla^2 \boldsymbol{b}. \tag{3.20}$$

The fields can be decomposed in perpendicular (in–plane) and parallel (out–of–plane, along z) components, namely $\boldsymbol{b} = (\boldsymbol{b}_\perp, b_z)$ and $\boldsymbol{u} = (\boldsymbol{u}_\perp, u_z)$. For the magnetic field $\boldsymbol{b}_\perp = \nabla a \times \hat{z}$, where a is the magnetic potential. The coefficient $\epsilon_H = d_i/L_0$ is the Hall parameter and is proportional to the amount of dispersive effects present in the system. Note that, for $\epsilon_H \to 0$, Eqs. (3.19)-(3.20) reduce to MHD (see Eqs.(3.7)–(3.8)). Generally speaking the Hall term becomes a significant factor at wavenumbers k such that $kL_0\epsilon_H = kd_i \sim 1$. The above equations are solved with the same algorithm used for the MHD case and same initial conditions. To remark, I used double periodic (x, y) Cartesian geometry, with a box size of $2\pi L_0$, using 4096^2 grid points, and with $R_\mu = R_\nu$=1700. I fix the above parameters for all the simulations reported here and we vary ϵ_H, going from the MHD case ($\epsilon_H = 0$) to the Hall case, choosing $\epsilon_H = 1/400, 1/100, 1/50$. For all the runs, the energy is initially concentrated in the shells with $4 \leq k \leq 10$ (wavenumbers k in units of $1/L_0$) with mean value E=$(1/2)\langle|\mathbf{v}|^2 + |\mathbf{b}|^2\rangle \simeq 1$, where $\langle\dots\rangle$ indicates a volume average. Using the above set of parameters, the dissipation wavenumber is $k_{diss} = R_\mu^{1/2}\langle j^2\rangle^{1/4} \sim 200$. For the HMHD simulations, the Hall wavenumbers are $k_H = \epsilon_H^{-1} = 400, 100, 50$. The maximum resolved wavenumber in all the simulations (allowed by the simulation resolution and the 2/3 rule) is $k_{\max} = 4096/3 \sim 1365$. A summary of the simulations is reported in Table 3.1, where $\lambda_{diss} = 1/k_{diss} = 1/[R_\mu^{1/2}\langle j^2\rangle^{1/4}]$ is the dissipation wavenumber.

Again, I performed the analysis at the time of the peak of non–linear activity that is the same for all the runs performed, namely $t \sim 0.5\tau_A$. One way to quantify the differences between MHD and HMHD turbulence is to compute the power spectra for $\boldsymbol{b}_\perp$ and $\boldsymbol{u}_\perp$ (in-plane components), the former is plotted in Fig. 3.18. We remark that the case with $k_H = 400$ (Run II) shows no appreciable difference from MHD (Run I). This may be due to the fact that the Hall effect becomes significant in this case in the dissipation range, and not in the inertial range, since in this simulation, $k_{diss} < k_H$ (see Table I). In contrast, Runs III and IV clearly differ from the MHD case, for wavenumbers $> k_H$. This difference in the power spectra has been already noticed in previous works, and is generally attributed to the dispersive effects. These effects can break, in fact, the Alfvénic correlations that are typical of MHD (134; 94).

Once again, when the turbulence is fully developed, coherent structures, in the form of magnetic interacting islands, appear. Between these interacting islands the perpendicular (out–of–plane) component of the current density j_z becomes very high, as it can be seen from Fig. 3.19, where a comparison between MHD and HMHD is shown. Another interesting feature seems to be that the current sheets are shorter and thinner. This is reminiscent of the systematic shortening and thinning of current sheets seen in isolated laminar reconnection simulations (143). As I said before, the current density is an important quantity since it captures many of the small scale features in both turbulence and in reconnection. I show in Fig. 3.20 the PDF of j_z (out of plane component), for the runs in Table 3.1. The core of the distributions is very similar for all the simulations, but, in the HMHD cases, the tails are more pronounced. This implies that the Hall effect cause an enhancement of the small scale activity, that is responsible for increasing intermittency in the system. I now examine the quantitative connection between enhanced intermittency and reconnection rates.

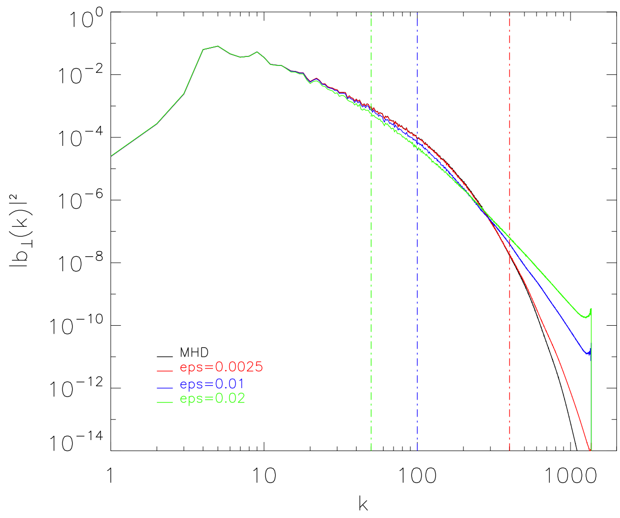

Figure 3.18: Power spectra of the "perpendicular" magnetic energy, for all the Runs reported in Table I. The vertical lines represent the Hall k-vector for Run II, III and IV, that is, respectively, $k_H = 400$ (red dot-dashed), $k_H = 100$ (blue dot-dashed) and $k_H = 50$ (green dot-dashed).

3.4.2 Reconnection in turbulence: Hall MHD *vs.* MHD

As reported in Fig. 3.21, the magnetic potential a reveals a collection of magnetic islands with different size and shape. Very similar patterns are observed for all the runs. Note that the potential a is very similar in both cases since this field is generally large-scale and very smooth. To capture the influence of the Hall physics, one should look at the local structure of the current, shown in Fig. 3.22(left). When Hall effect is significant, a clear bifurcation of current sheets is observed.

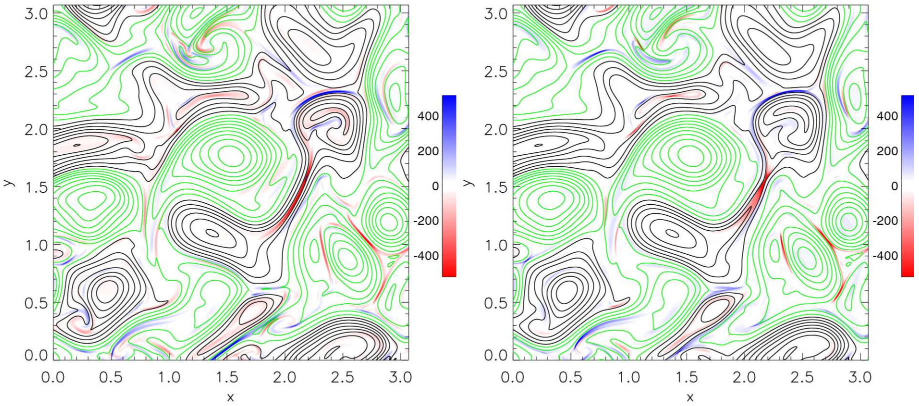

Figure 3.19: Current density profile j_z in a sub-region of the simulation box, for both MHD (left) and HMHD with $\epsilon_H = 1/50$ (right). The magnetic flux a is also represented as a line contour. As expected in 2D turbulence, strong and narrow peaks of current density are present between magnetic islands. As can be seen in Fig. 3.20, current density are higher in HMHD.

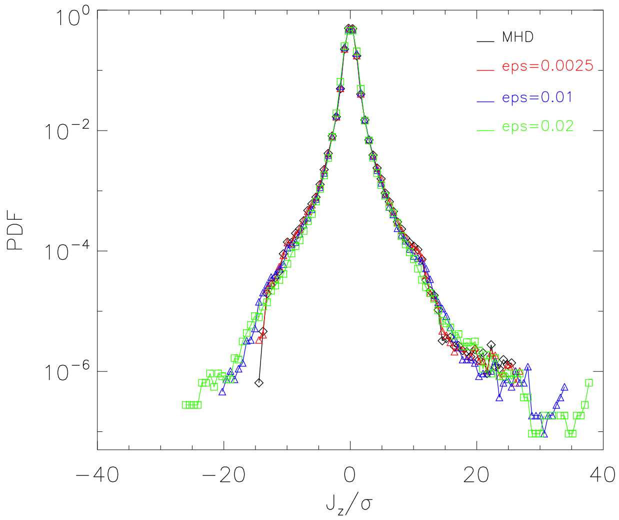

Figure 3.20: PDF of j_z, normalized to its own rms value, for $\epsilon_H = 0$ (black), $1/400$ (red), $1/100$ (blue), and $1/50$ (green). The longer tails present in Run IV may be the signature of more intense small-scale activity, due to stronger dispersive effects.

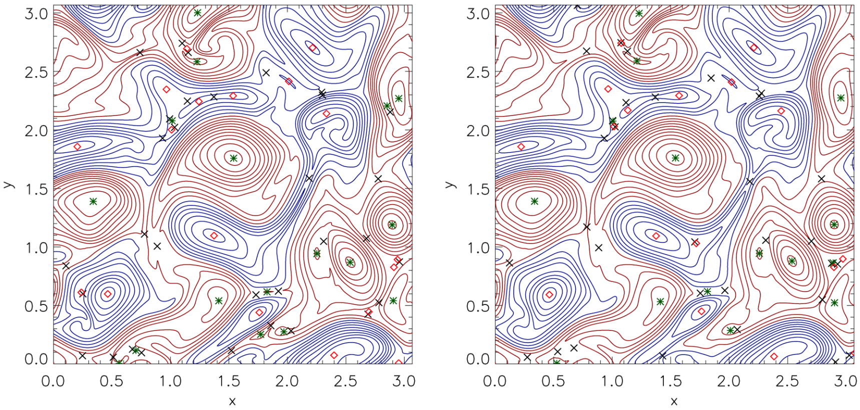

Figure 3.21: Line-contours of of the magnetic potential a for Run I (left) and Run IV (right), in a sub-region of the simulation box. The position of the critical points is reported as well: O-points (green stars for the maxima and open red diamonds for the minima) and X-points (black ×). Magnetic reconnection locally occurs at each X-point.

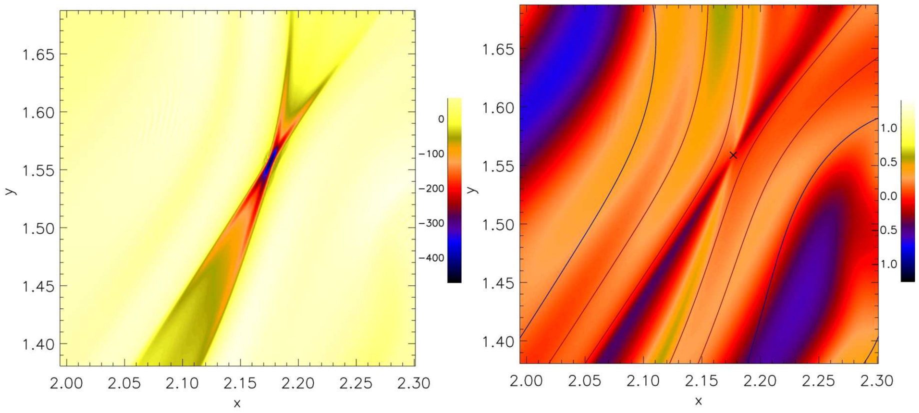

Figure 3.22: (Left) A contour plot of the out-of-plane component of the current j_z in a sub-region of the simulation box for Run IV. It is clearly visible the bifurcation of the sheet and the typical structure of a reconnection region. (Right) A contour plot of the out–of–plane component of the magnetic field b_z, in the same sub-region of the simulation box. The magnetic flux a is also represented as a line contour. A quadrupole in the magnetic field can be identified, revealing the presence of Hall activity.

To further investigate the role of the Hall effect on the process of reconnection in turbulence, I analyzed the out-of-plane magnetic field b_z around some X-points. As expected from theory(147), an out-of-plane magnetic quadrupole forms nearby reconnection sites; this is shown in Fig. 3.22(right). The magnetic field shows four distinctive polarities, organized with respect to the X–point. This effect is thought to be a strong signature of Hall activity during reconnection in astrophysical plasmas (103), and in laboratory plasmas (148; 149) and here we confirm that this is a clear signature of Hall effect in turbulent reconnection. In order to understand quantitatively the Hall effects on reconnection, we analyze the magnetic field topology and reconnection rates. The metodoligy of analysis is the same presented in Sect. 3.2.1 that made use of the Hessian matrix. The number of X-points is ~ 127, and is similar number for all the runs, indicating that the number of X–points does not depends on small-scale features, but rather on initial conditions. Once I have obtained the position of all the critical points, it is possible to measure the reconnection rate of interacting islands as the rate of change of the magnetic flux at each X–point that, I recall, is:

$$\left.\frac{\partial a}{\partial t}\right|_{\times} = -E_{\times} = (R_{\mu}^{-1} j)_{\times}. \tag{3.21}$$

The reconnection rates have been normalized to the mean square fluctuation δb_{rms}^2 (~ 1 for all the runs). Note that Eq. (3.21) gives exactly the reconnection rate for a fully 2D (MHD) case, while, in the HMHD case (2.5D), this expression gives the rate of component-reconnection. The PDFs of $E_{\times}$, for the runs in Table I, are reported in Fig. 3.23. All the distributions show a broad range with strong tails, the averaged lying near $E_{\times} \sim 0.05 - 0.06$ while the full range spans $|E_{\times}| \in [10^{-5}, 0.4]$. The PDF's have been constructed using constant weight m per-bin (variable amplitude PDF), with $m = 6$. The distribution of reconnection rates for the weak Hall case (Run II) is very similar to the MHD results (Run I), as expected from previous discussions. In the stronger Hall case (Run III and IV), instead, higher tails appear in the PDF. Apparently, for higher values of ϵ_H the frequency of occurence of large reconnection rates is substantially increased. The increased frequency of large rates influences the means. As an example, for both Run I and II I obtained the mean value $\langle |E_{\times}| \rangle \simeq 0.05$, while for Run IV $\langle |E_{\times}| \rangle \simeq 0.06$. This analysis confirm that the Hall term plays an important role in turbulence, where magnetic islands simultaneously reconnect in a complex way. In particular, when the Hall parameter is enhanced, being this the ratio between the ion skin depth and the system size, distributions of reconnection rates have higher tails, revealing more frequently occurring explosive (very large) reconnection events than in the MHD case.

As already pointed out in (121) and showed in Sect. 3.2.1, there is a relation between the stronger reconnection rates and the geometry of the reconnection region, in fact these strong reconnecting electric fields satisfy the scaling relation

$$E_{\times} \sim \frac{l}{\delta} = \sqrt{\lambda_R} = \sqrt{\frac{\lambda_{max}}{\lambda_{min}}} \tag{3.22}$$

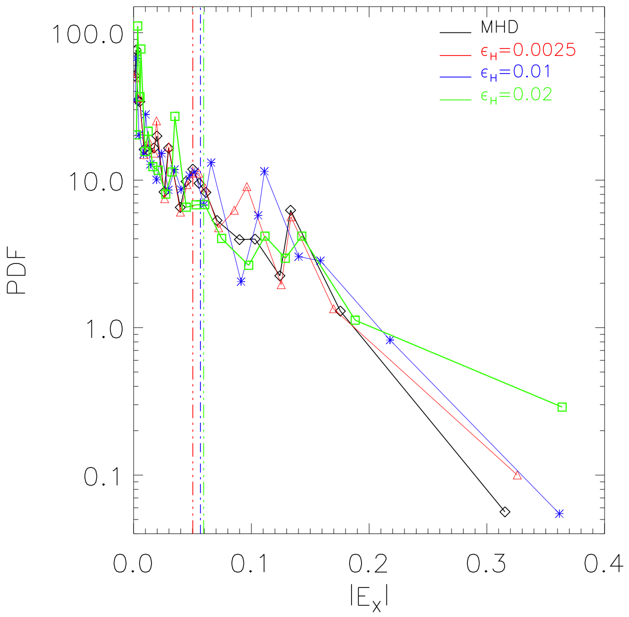

Figure 3.23: PDF of the reconnection rates for $\epsilon_H = 0$ (MHD, black rombus), $\epsilon_H = 1/400$ (red triangles), $\epsilon_H = 1/100$ (blue stars) and $\epsilon_H = 1/50$ (green squares). The vertical dash-dotted line represents the mean value of the distribution $\langle |E_\times| \rangle$ for Run I (black), Run II (same as Run I), Run III (blue) and Run IV (orange).

where, I recall, l and δ are related, respectively, to the elongation and to the minimum thickness of the current sheet, i.e. to the geometry of the reconnecting region, while λ_{max} and λ_{min} are the Hessian eigenvalues evaluated at the X-point. In Fig. 3.25, I reported the reconnection rates, associated to each X-point, as a function of λ_R, for Runs I, III, and IV. All distributions follow the proposed power-law (at least for stronger reconnection events), but in the HMHD case the values are more scattered and are bounded by lower λ_R. I evaluated, for each run, the evolution of $\langle \lambda_R \rangle$ in function of ϵ_H (not shown here), and I observed that, for the strongest Hall effect case $\epsilon_H = 1/50$, the computed value of $\langle \lambda_R \rangle$ is reduced to half the value obtained in the MHD case. Following the methodology adopted in Sect. 3.2.1, to qualitatively characterize every reconnecting region, I extract information about currents, magnetic fields and about the geometry of the diffusion regions. Since I know the ratio of the eigenvalues obtained from the Hessian matrix analysis, the problem reduces to find just one of these lengths, such as the current sheet thickness δ. Again, for each X-point, it was necessary to build a system of reference that has the origin at the X-point and, using the eigenvectors obtained in the Hessian analysis, then to define a local coordinate system based on the unit vectors $\{\hat{e}_s, \hat{e}_\mathrm{t},\}$, where the coordinates s and t are related to δ and l respectively. With respect to this new reference system, the tangential and normal component of the magnetic field are evaluated as $b_t = \hat{e}_t \cdot \mathbf{b}$ and $b_n = \hat{e}_s \cdot \mathbf{b}$, while the current profile is obtained

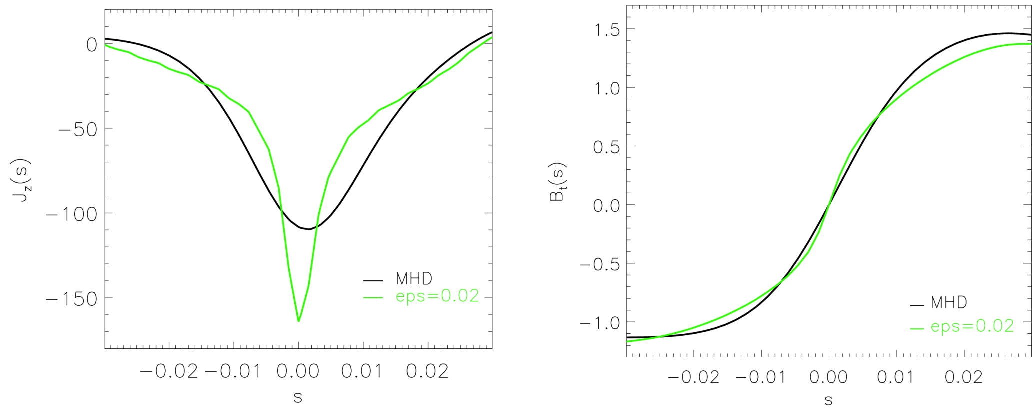

Figure 3.24: Current density $j_z(s)$ (left) and tangential component of the magnetic field b_t (right), in the vicinity of the same X-point, for both MHD (black) and HMHD with $\epsilon_H = 1/50$ (green). s is the direction along $\hat{e}_s$ - the steepest gradient of the Hessian of a. In HMHD current sheets are narrower and more intense.

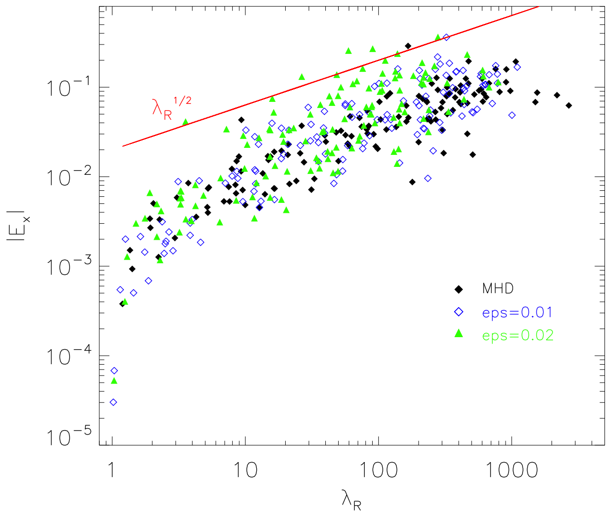

Figure 3.25: The relation between the reconnection rate (the electric field at the X-point) and the geometry of the reconnection region (the ratio of the eigenvalues) for both MHD (black rombus) and HMHD (blue and green). The presence of a power-law fit (red solid line) demonstrates that there is a relation between the reconnection rate and the geometry of the diffusion region.

ϵ_H	$\langle\delta\rangle$	$\langle l\rangle$	$\langle E_\times\rangle$	$\mathrm{MAX}\{E_\times\}$
0	0.014	0.286	0.049	0.315
$1/400$	0.013	0.272	0.050	0.326
$1/100$	0.008	0.172	0.057	0.362
$1/50$	0.005	0.077	0.059	0.364

Table 3.2: Characteristic lengths and reconnection rates for each run. The first column is the Hall parameter, second column the average thickness of reconnection regions, the average length of reconnection sites is reported on column 3, while the average and the maximum reconnection rates are reported on column 4 and 5 respectively.

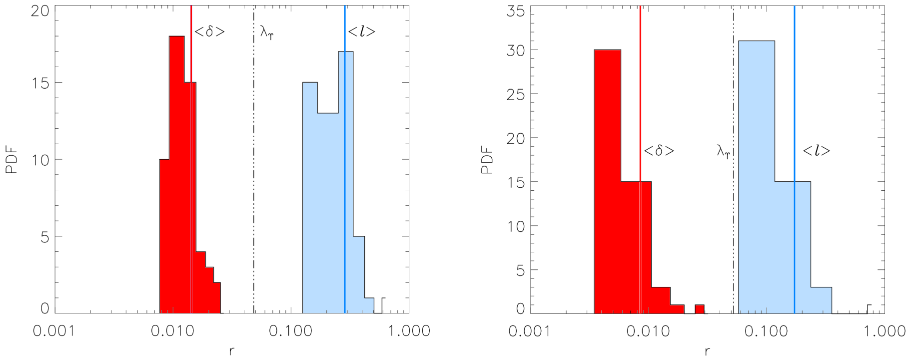

Figure 3.26: Histograms of thicknesses δ, (red bars), and elongations l, (azure bars) for MHD (left) and HMHD with $\epsilon_H = 1/100$ (right). Vertical lines are average values $\langle\delta\rangle$ (red) and $\langle l\rangle$ (azure), the vertical dotted line represent the Taylor microscale λ_T. In HMHD, the reconnection sites seem to have, in average, smaller thickness and elongation.

with an iterating fit procedure along the s coordinate. The above analysis has been performed only for stronger reconnection sites. For the present simulations, this means $|E_\times| > 10^{-2}$ (for all runs), together with the restriction $\lambda_{max}/\lambda_{min} > 150$ (Run I, II, III), and $\lambda_{max}/\lambda_{min} > 90$ for HMHD (Run IV). In Fig. 3.24 we compare results from MHD (Run I) and HMHD (Run IV), showing the current profile and the local magnetic field near a particular X-point. The current density $j_z(s)$ and the projected tangential magnetic field $b_t(s)$ has been interpolated along the direction of $\hat{e}_s$. As already observed in Fig. 3.20, two main features are at work when the Hall effect is not negligible, namely, the thickness δ is reduced with respect the MHD case, and j_z reaches stronger values. This example serves to illustrate this effect, which we confirm statistically through an analysis of the values of δ and l for all the stronger X-point regions. The associated PDFs of δ and l have been computed, for both MHD and HMHD, and the comparison is reported in Fig. 3.26. In the Hall case, in average, the current sheets are both thinner and shorter than in the MHD counterpart. These characteristic average lengths are reported in Table 3.2.

3.5 Generalized Sweet–Parker theory for magnetic reconnection

The turbulent reconnection activity identified in this chapter takes place in an environment in which the symmetric local conditions envisioned in standard laminar models are unlikely. It is therefore appropriate to employ the extension of the standard picture to asymmetric configurations. The Sweet–Parker–type analysis for asymmetric anti–parallel reconnection has been studied in an earlier work by (150). In particular, this analysis allows the reconnecting magnetic field strengths and plasma densities to be different on opposite sides of the dissipation region. Here we will summarize some of their main results. Asymmetric reconnection has also received recent attention in observations (152; 151) and kinetic simulations (153). In the incompressible case and in our notation, the Cassak-Shay (150) asymmetric reconnection rate is given by

$$E_{\times}^{th.} \simeq \sqrt{\frac{b_1^{3/2} b_2^{3/2}}{R_\mu \ell}}. \tag{3.23}$$

being b_1 and b_2 the upstream magnetic fields on each side of the X-point. For this purpose we chose the magnetic fields evaluated at $2\delta_{1,2}$, namely $b_i = b_t(2\delta_i)$. Here we examined whether the observed ensemble of turbulent reconnection events scales as asymmetric "Sweet-Parker" in this sense, with resistivity causing the dissipation. To acquire a broader picture of the scaling, we evaluated Eq. (3.23), first for simulations described in Sects. 3.3 to view in which way the reconnection rates scale in time with respect the expected rates described in the model, and then for HMHD Runs. In Fig. 3.27, the reconnection rates, for different times of the simulation described in Sect. 3.3, are compared with the asymmetric Sweet-Parker prediction given by Eq. (3.23). It is evident that the model nicely describes the process of reconnection in 2D MHD turbulence: during the time relaxation of turbulence, the reconnection events still obey the theory proposed by (150).using several runs (listed in Fig. 3.27). Fig. 3.27 shows that in all the simulations the reconnection rates are consistent with the prediction given by Eq. (3.23). In this scenario turbulence plays a crucial role, determining locally the parameters that control the Sweet-Parker reconnection rate, namely, the lengths and local magnetic field strengths. Apparently, reconnection is an integral part of the turbulent cascade. Fig. 3.28 show the comparison between Run I (MHD), Run III ($\epsilon_H = 1/100$) and Run IV ($\epsilon_H = 1/50$) reconnection rates versus the expectations. Apparently, in the Hall cases the reconnection rates are more broadly distributed, and depart from the MHD behavior. In particular, there appears to be a constant fractional increase in reconnection rate that grows with increasing Hall parameter.

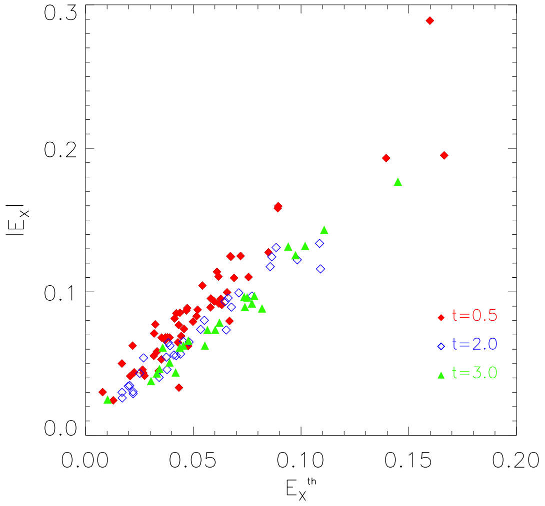

Figure 3.27: (Asymmetric Sweet–Parker prediction at different times of the simulation. This theory accurately describes the dynamics of reconnection in 2D MHD turbulence indicating that the system is reconnecting in a asymmetric Sweet-Parker scenario.

3.6 Conclusions

The nonlinear dynamics of magnetic reconnection in turbulence has been investigated through direct numerical simulations of decaying 2D MHD and HallMHD. In the high resolution simulations, many reconnection events are seen, involving simultaneously many magnetic islands of various size. The reconnection is spontaneous but locally driven by the fields and boundary conditions provided by the turbulence.

Computing the electric field at the X-points, we see that turbulence produces a broad range of reconnection rates, with values in excess of 0.1 to 0.3 in dimensionless global Alfvén units. In addition, the strongest reconnection rates vary in proportion to ℓ/δ, the aspect ratio of the reconnection sites that characterize the geometry of the diffusion regions. This scaling appears superficially to differ greatly from classical laminar theories (114; 115), but taking into account the nearby magnetic field produced by the turbulence, a generalized form of Sweet-Parker scaling (150) is restored. These results explain how rapid reconnection occurs in MHD turbulence in association with the most intermittent non–Gaussian current structures, and also how turbulence generates a very large number of reconnection sites that have very small rates. Reconnection, like other transport processes, is greatly affected by turbulence (154) and reconnection rates, like other turbulence parameters, have a broad distribution of values. In contrast to laminar reconnection models that provide a single predicted reconnection rate for the system, turbulent resistive MHD gives rise to a broad range of reconnection rates that depend on local turbulence parameters. Many potential reconnection sites are present, but only a few are se-

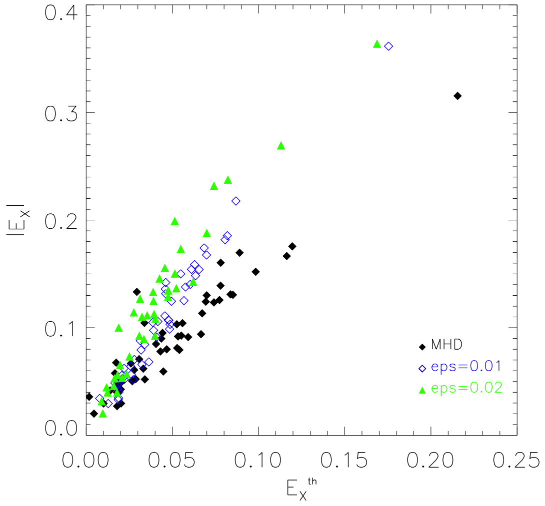

Figure 3.28: Computed reconnection rates vs expectation from Eq. (3.23), for Run I (black diamonds), Run III (open blue diamonds), and Run IV (green triangles). The Hall cases seem to slightly depart from the Sweet-Parker asymmetric expectation.

lected by the turbulence, at a given time, to display robust reconnection electric fields. We have seen that reconnection becomes an integral part of turbulence, as suggested previously (123; 155). In fact, results of the present type may shed light on possible scalings as Reynolds numbers are increased, even though direct computational scalings remain greatly challenging. In particular, we expect that the distribution of reconnection rates can be related to the issue of maintaining finite energy dissipation in the infinite Reynolds numbers. A detailed examination of this connection remains for future study.

From the freely decaying turbulence, time dependent study, it was found that the reconnection rate distribution evolves rapidly from a state that has essentially no fast reconnection sites, and develops a “hard” distribution that has a highly enhanced tail of strong rates, in a time of the order of the peak turbulence dissipation time scale. Subsequently, as the turbulence ages and begins to slow down, so also does the reconnection rate distribution soften, with the tail of strong rates diminishing in just a few non–linear times.

It was also provided a direct comparison of the statistics of reconnection rates obtained from simulations of MHD turbulence and Hall MHD turbulence for cases with increasing Hall parameter $\epsilon_H = d_i/L_0$. For small values of Hall parameter there is very little difference in distributions of electric current density or reconnection rates. However for stronger Hall parameter $\epsilon_H > 0.01$ one begins to see enhancements of reconnection. In particular while there is a modest increase in average reconnection rate, there is a more dramatic increase in the frequency of occurrence of large reconnection rates. Associated with this is the shortening and thinning of current sheets, and the appearance of bifurcated current sheets, all previously reported as properties of laminar reconnection with Hall effect.

Evidently the impact of Hall effect depends crucially on whether this term in Ohm's Law become significant at wavenumbers k_H lower than the reciprocal dissipation scale k_{diss}, so that it influences the upper inertial range, or if it becomes significant only at scales smaller than where dissipation becomes strong. Therefore in HMHD simulations with scalar resistivity and viscosity such as the ones I carried out, the simulator has complete control over the relationship of the relevant wavenumbers k_H and k_{diss}. What is less clear is how to estimate this relationship in a low collisonality plasma. Typically, as suggested in (156), in kinetic theory d_i is *near* the scale at which dissipative effects become significant, but it is not clear to us whether one can make general statements concernig the precise value of the ratio k_H/k_{diss}. If dissipation sets in at scales much smaller than d_i, e.g., through dominance of electron dissipation effects, the present work suggests that the Hall effect can be important in establishing the most robust reconnection rates that will be observed in turbulence. We have not however examined cases with very large Hall parameters $\epsilon_H \sim 1$, which become computationally prohibitive. I find that as the Hall parameter (ratio of ion inertial length to energy containing length) is increased from zero to $1/50$, the distribution of reconnection rates develops a more pronounced tail at the highest values. Meanwhile the median rate is increased by only a few tens of percent. This is consistent with the idea that Hall effect can influence the fastest rates of reconnection most effectively. However many "slow" reconnection rates sites are found both with and without Hall effect. Further study will be required to confirm and complete an understanding of how Hall effect influences reconnection rates in turbulence.

Conclusions

This thesis work concerns the study of turbulence in two physical system, i.e., the solar wind and the reconnection sites. In particular, we tried to emphasize the different way in which turbulence appears, manifests itself and evolves, sometimes representing the main physics in the dynamical evolution of the considered system. During the last years, a strong effort was spent by reserachers in the quest to understand turbulence. Indeed, the knowledge of this complex phenomenon has shown remarkable progress recently, thanks to the advancement in theoretical models, numerical simulations and to the various space missions available. For all these reasons, recognition of turbulence has matured; however, it still remains a "terra–incognita". Because of the complexity of turbulence, it was not easy to write down a simple overview that briefly describes the enormous theoretical background, trying to establish a link between the different representations and descriptions, but, finally, the goal was achieved.

In this thesis work, we approach the study of turbulence from two different perspectives. First of all, using a kinetic description, we start from an observational point of view to look at some non-linear phenomena, i.e, the ponderomotive effect and the dissipation in collisionless plasma, related with the presence and the growth of turbulence in plasma waves. Then, from the point of view of numerical simulations, using a magnetohydrodynamics description, we move our attenption on the process of magnetic reconnection.

In the first part of this work, we studied the electric signals, obtained by the instruments S/WAVES onboard the two spacecraft of the STEREO/NASA mission. We tried to understand the ponderomotive effect generated by an oscillating Langmuir wave on the density background of the solar wind and the possible generation of ion–bulk waves viewed as dissipation mechanism in collisionless plasmas. It was shown that the voltages, observed identically on the three STEREO antennas at frequencies $(10^2 - 10^3)$ Hz, are consistent with the variations observed in the spacecraft potential, due to small scale density fluctuations present in the solar wind. A calibration for such density fluctuations was provided too, using simultaneously measurements of Langmuir waves at high frequencies and density fluctuations observed in the low frequency component. This calibration enable us to retrieve a more precise value of the photoelectron current. It was given a direct observational evidence for non–linear coupling between solar wind density fluctuations and Langmuir waves, with an electric–to–kinetic energy ratio $W_L > 10^{-4}$. This is the first time that the ponderomotive effect is observed in natural plasma. The above frequency range corresponds to solar wind density fluctuations with typical wavelengths $\lambda \sim [500 - 5000]$ m. To the best of our knowledge, it was the first time that small–scale density fluctuations in the solar wind at such wavelength range are measured. These small scale density measurements provide a new opportunity to directly observe the physical processes occurring close to the dissipation range of solar wind turbulence. See Ref. (45) for more details.

In a more general context, we point our interest on the dissipation mechanisms in collisionless plasma, a step of crucial importance for understanding the origin and the nature of the solar wind and the problem of high–frequency turbulence in space plasmas. Recent kinetic numerical simulations simulated the dissipation mechanisms, acting in the solar wind at short spatial length scales. In this studies, the dispersion relation shows two branches of acoustic type electrostatic waves, the usual ion–acoustic waves and a new branch of electrostatic waves, identified as ion–bulk waves. The excitation of these waves is due to the generation, through resonant interaction between ions with ion–cyclotron waves, of diffusive plateaus in the longitudinal velocity distribution. As a result of this process, short wavelength packets are recovered in the electric field component parallel to the ambient magnetic field. It was observed that both electric signals, coming from the S/WAVES instruments in the frequency range from $[1-5]$ kHz, and the ion–bulk waves, obtained in hybrid–Vlasov simulations, present a high fluctuations level in the form of localized wavepackets. From a systematic comparison of the observed peaks at few kHz with those obtained in hybrid–Vlasov numerical simulations, it was hypothesized that the identified small–scale wavepackets are related to the ion–bulk electrostatic fluctuations. These fluctuations are associated with ions velocity distributions, that display marked plateaus in the vicinity of the thermal speed and represent one of the main dissipation mechanism in collisionless plasma. A publication, (84), on this subject was submitted to international physics journals.

In the last part of this thesis, we study the process of magnetic reconnection in two-dimensional, high resolution, MHD simulations, trying to extract the influence of turbulence on the entire phenomenology. It was shown that the presence of turbulence enhances the small–scales activity, producing a broad range of reconnection events with reconnection rates more similar to that observed in space plasmas. Magnetic reconnection is a spontaneous phenomenon, but locally driven by the fields and the boundary conditions provided by turbulence. Many potential reconnection sites are present, but, at a given time, only a few of them are selected by turbulence to display robust reconnection electric fields, $E_\times$. In addition, the strongest reconnection rates vary in proportion to the aspect ratio of the reconnection sites, ℓ/δ.

Recent results in this line of study, involving turbulent reconnection rates at different times, and a first look at how Hall effect influences reconnection in turbulence have also been highlighted. From a time dependent study, in which turbulence is freely decayed, we have found that the reconnection rate distribution evolves rapidly from a state that has essentially no fast reconnection sites and develops a "hard" distribution that has a highly enhanced tails of strong rates, in a time scale of the order of the peak turbulence dissipation time scale. Subsequently, as the turbulence ages and begins to slow down, so also does the reconnection rate distribution soften, with the tail of strong rates decreasing in just a few nonlinear times.

The results concernig the influence of the Hall effect in the Ohm's law on the distribution of reconnection rates in turbulence appear very intriguing. Indeed, we find that, as the Hall parameter (represented by between the ratio of the ion inertial length and the energy containing length) increases from zero to 1/50, the distribution of reconnection rates develops a more pronounced tail at the highest values. Meanwhile, the median rate increases by only a few tens of percent. This results are consistent with the idea that the Hall effect can influence the fastest rates of reconnection more effectively. However, many "slow" reconnection rates sites are found both with and without the presence of the Hall effect in our numerical simulations. Further, more study are required to confirm and complete our understanding of how the Hall effect can influence the reconnection rates in turbulence. See Ref. (122) for more details.

Appendices

Appendix A

Using the STEREO spacecraft as a density probe

In monopole mode, an antenna measure the difference of potential between the antenna potential and the spacecraft floating potential, where the last one is usually considered a ground to study electric field oscillations measured on the antenna. Therefore, the voltage waveforms are generally interpreted and calibrated in term of in–situ electric field waveforms. In contrast, we used explicitly in this calculations the spacecraft potential variations, taking advantage of the large difference in surface between the spacecraft and the antennas which makes their equilibrium time scales very different, so that there is a large frequency range in which the voltage fluctuations measured in monopole mode reveal the density fluctuations.

A.1 Floating potential of spacecraft and antennas

The spacecraft body emits and collects charged particles, and its electric potential permanently adjusts to the change of the ambient plasma parameters, to ensure the currents balance. The charging of the STEREO body is due to some physical processes (51): (1) incident energetic photons inducing photoelectron emission (50); (2) incident energetic electrons striking the surface, inducing secondary emission of electrons; and (3) ambient electrons and ions striking the surface and transferring their charge.
To be more detailed :

1. the impact of energetic photons induce the emission of photoelectrons from the spacecraft by solar ultraviolet radiation and the comparison of the photoelectron current I_{ph}. To have an estimation, we consider that the average solar ultraviolet radiation at 1 AU is $\sim 10^{-3}\ Wm^2$ that corresponds to an average flux of ionising photons $F_\odot \simeq 10^{14}\ m^{-2}s^{-1}$. On a surface at zero potential at 1 AU, the photoemission flux j_{ph} depends on the average surface photoemission efficiency:

$$j_{ph} = \delta 10^{14} m^{-2} s^{-1} \tag{A.1}$$

   per unit of projected sunlit surface, with $\delta \sim$ 1–4 for typical spacecraft covers (46; 47; 48; 49). Photoelectrons escape from the sunlit face of the spacecraft of surface $S_\perp$, so that $I_{ph} = j_{ph} S_\perp$.

2. The secondary emission of electrons caused by the impact of energetic electrons is important only for striking electrons with energy greater than 10eV, and is practically negligible for the two STEREO spacecrafts.

3. The third physical effect could be divided in two part, (i) the collection of solar wind electrons and (ii) protons (we neglected the very small contribution of the heavier ions). (i) Solar wind electrons have a thermal velocity ($v_{th,e} \simeq 1200$ $km\ s^{-1}$) larger than the solar wind speed ($v_{SW} \simeq 300$–$800\ km\ s^{-1}$), so that the associated incoming electron flux on a spacecraft at zero potential is the ambient electron random flux $j_e \simeq n_e\sqrt{k_B T_e/2\pi m_e} < 10^{13}\ m^{-2}s^{-1}$ (m_e , n_e and T_e are respectively the electron mass, density and temperature) and solar wind electron are collected on the total surface S_{tot} so that $I_e = j_e S_{tot}$. (ii) Solar wind protons have a thermal velocity ($v_{th,p} \simeq 50\ km\ s^{-1}$) much smaller than the solar wind speed, so that solar wind protons are collected on one face only and the associated attachment flux is better estimated from the mean proton flux $j_p \simeq n_p V_{SW} \sim 10^{12}\ m^{-2}s^{-1}$. With $S_{tot} \simeq 6S_{perp}$ (considering a cubic shape), the proton current is more than an order of magnitude lower than the proton current $I_p = j_p S_{perp} \ll j_e S_{tot} = I_e$. I recall that the values of the parameters are those typical for the free solar wind at 1 AU.

Summarizing, $I_{ph} \gg I_e \gg I_p$, so that we neglected the secondary emission and the protons attachment and we considered, as main charging processes, the photoelectron current and the ambient electron current. Because the escaping electrons are more than the attached ones, STEREO surfaces charge positively, until its positive electric potential Φ binds sufficiently the photoelectrons to make their net outward flux balance the inward flux of solar wind electrons, and this means that, to have the balance, the potential of the bodies (spacecraft and antennas) provide the photoelectrons with a potential energy that outweights their typical kinetic energy of a few eV. To obtain the current balance, we considered that both electron populations are Maxwellian with temperature T_e and T_{ph}, so that the expressions for ambient electrons and photoelectrons current, respectevely, are given by (52):

$$I_{ph} \simeq j_{ph} e S_{\perp} \left(1 + \frac{e\Phi}{k_B T_{ph}}\right)^{\alpha} exp\left(\frac{-e\Phi}{k_B T_{ph}}\right) \tag{A.2}$$

$$I_e \simeq n_e \left(\frac{k_B T_e}{2\pi m_e}\right) eS \left(1 + \frac{e\Phi}{k_B T_e}\right)^{\beta} \tag{A.3}$$

where e is the electron charge, α and β are both equal to 0, $1/2$ and 1 for respectively plane, cylindrical and spherical geometry of the considered charging process.

A.2 Equilibrium potential

Once we estabilished the charging processess and their expressions, we could show the spacecraft equilibrium potential. Before proceding in this way, it is useful to give some geometrical informations. The scale length of the spacecraft body L_{sc} is larger than the photoelectrons' Debye length (10 cm at 1 AU), the photoemission is consider to take place in plane geometry so that $\alpha_{sc} = 0$. On the other hand, since L_{sc} is smaller than the solar wind electron Debye length (10 m at 1 AU), plasma electrons are collected in 3D so that $\beta_{sc} = 1$. The current balance condition $I_{ph} = I_e$ applied to Eqs.(A.2)–(A.3) for the spacecraft body then gives its equilibrium potential Φ_{sc}:

$$\Phi_{sc} = -\frac{k_B T_{ph}}{e}\, log_n \left[\frac{n}{N_0} \left(1 + \frac{e\Phi_{sc}}{k_B T_e} \right) \right] \tag{A.4}$$

where $N_0 = j_{ph}(k_B T_e/2\pi m_e)^{-1/2} S_{\perp}{}^{sc}/S_{sc}$. The above calculations also hold for the equilibrium potential of the antenna Φ_A in cylindrical geometry so that $\alpha_A = \beta_A = 0.5$ in Eqs. (A.2)–(A.3), which gives:

$$\Phi_A \simeq -\frac{k_B T_{ph}}{e}\, log_n \left[\frac{n}{N_0^A} \left(\frac{1 + e\Phi_A/k_B T_e}{1 + e\Phi_A/k_B T_{ph}} \right)^{1/2} \right] \tag{A.5}$$

where $N_0^A = j_{ph}(k_B T_e/2\pi m_e)^{-1/2} S_{\perp}{}^{A}/S_A$. To solve Eqs. (A.4–A.5) we made use of STEREO spacecraft parameters (note that Eq. (A.5) is a rough approximation because the antenna length is of the order of the Debye length, but this does not significantly affect the final result). In detail, The dimensions of the spacecraft are $L_1 \times L_2 \times L_3 = 1.14 \times 1.22 \times 2.03$ meters, with a sunlit surface $S_{\perp}^{sc} = L_2 \times L_3 \simeq 2.5$ m^{-2}. The solar wind electrons are collected from all the spacecraft surface, except the face located in the wake, so that the surface $S_{sc} \simeq 9.9$ m^{-2}. The S/WAVES antennas are 6 m long, with an average diameter of 23.6 mm and inclination of 125° to the sun–spacecraft direction. This gives a sunlit projected surface of about $S_{\perp}^{A} = 0.12$ $m^{-}2$ and a total surface area of about $S_{tot}^{A} = 0.45$ m^{-2} per boom. To complete the calculations, we choosed, $T_{ph} = 3$ eV and typical solar wind densities $n = [1\text{–}10]$ cm^{-3} and temperature $T_e = 10$ eV. Eqs. (A.4–A.5) yield to $\Phi_{sc} = [3\text{–}8]$ Volts and $\Phi_A = [5\text{–}10]$ Volts.

A.3 Charging time scales

The above results are valid as long as the solar wind density fluctuates with frequencies lower than the typical charging frequency of the considered object, so that the equilibrium remains quasistatic. We concentrated on density fluctuations with frequencies $f_{\delta n}$ lower than the charging frequency of the spacecraft f_{sc}, but larger than the charging frequency of the antenna f_A. Indeed, for $\delta n/n$ to produce a signal on the monopole antenna voltage, the density fluctuation must modify the spacecraft potential without modifying the antenna potential, that is density fluctuations that have frequencies $f_{\delta n}$ such that $f_A < f_{\delta n} < f_{sc}$. To evaluate the two frequencies we calculated the charging e–folding time $\tau = RC$, where C is the capacitance and R the resistance of the considered object (and it was necessary to made other geometrical assumption). Since the dimension of the spacecraft L_{sc} and the antenna radius a are both much smaller than the ambient Debye length λ_D, the electric field surrounding them can be considered a Coulomb field locally, vanishing at distance λ_D. The spacecraft capacitance C_{sc} can be roughly evaluated as the capacitance of a spherical conductor of radius $L_{sc} \simeq 1$ m, finding $C_{sc} \simeq 4\pi\epsilon_0 L_{sc} \simeq 110$ pF. A better estimation using two cubes instead of a sphere actually gives $C_{sc} \simeq 200$ pF, that was the final choice. The antenna capacitance C_A is evaluated as the low frequency capacitance of a cylindrical conductor of length L and radius a in a plasma of Debye length λ_D (53). In the limit $L \gg \lambda_D$ the antenna capacitance is:

$$C_A \simeq \frac{2\pi\epsilon_0 L}{log_n(\lambda_D/a)} \simeq 47pF \tag{A.6}$$

while for $L \ll \lambda_D$ it reduces to the capacitance in vacuum:

$$C_A \simeq \frac{2\pi\epsilon_0 L}{log_n(L/a) - 1} \simeq 64pF. \tag{A.7}$$

To take in account the fact that STEREO antennas have lenght of the same order as the Debye lenght, we choosed an intermediate value, i.e. $C_A \simeq 60$ pF. The resistance could be calculated as the inverse of the variation of the current with respect the potential ($R = |dI/d\Phi|$), but since the photoelectron current is the fastest charging process we obtained $R \simeq |dI_{ph}/d\Phi| \simeq (e/k_B T_{ph})$. From the balance $I_{ph} = I_e$, it comes out for the resistance:

$$R_i^{-1} \simeq eS^i \frac{e}{k_B Tph} n \left(\frac{k_B T_e}{2\pi m_e}\right)^{1/2} \left(1 + \frac{e\Phi_i}{k_B T_e}\right)^{\beta_i} \tag{A.8}$$

with $i = sc$ or A, $\beta_{sc} = 1$, $\beta_A = 1/2$. The charging frequencies $f_i = 1/(2\pi R_i C_i)$ are solved numerically and shown in Fig. A.1 as a function of the plasma density, the electron temperature and the photoelectron temperature. They are nearly independent to the electron temperature in the range of solar wind parameters (central panel). The dotted line in the right panel indicates the photoelectron temperature around 3 eV. Summarizing, for typical solar wind parameters, density fluctuations with frequencies between ~ 100 Hz and a few kHz produce a change in spacecraft potential, but no change in antenna potential. Signals of much higher frequency vary too fast for changing the floating potential of the spacecraft and antennas. Signals of much smaller frequency similarly modify the floating potentials of the spacecraft and antennas, so that the voltage difference between them is too small to be observed. For density fluctuations signals, the antenna acts as a ground while the potential of the spacecraft varies with the density fluctuation; whereas electric field oscillations behave just opposite: spacecraft potential is a ground and the antenna potential oscillates with the electric field.

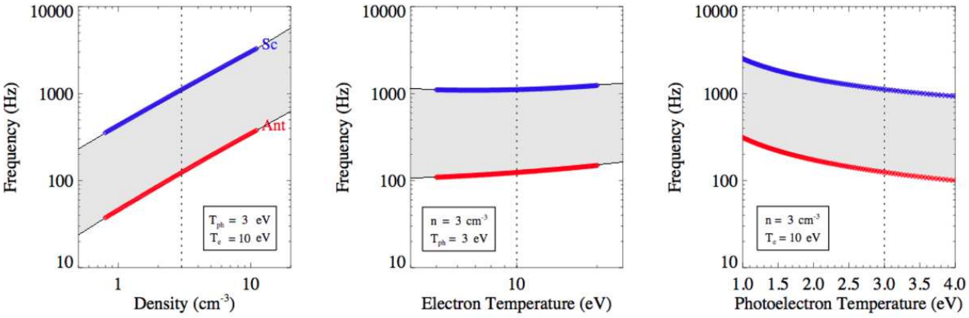

Figure A.1: Frequency range of detection of density fluctuations (in grey) between the spacecraft (blue line) and antenna (red line) charging frequencies as a function of density n (left panel), electron temperature T_e (central panel) and photoelectron temperature T_{ph} (right panel). The vertical dotted lines show typical solar wind parameters, in the third panel it shows the photoelectron temperature associated with the STEREO spacecraft $T_{ph} \simeq 3$ eV.

A.4 Variations of spacecraft potential associated to density fluctuations

At this point of the discussion, differentiating Eq. (A.4), we obtained an expression in which each small variation δn of the plasma density, in the above mentioned frequency range, produces a change in spacecraft potential $\delta\Phi_{sc}$:

$$\delta n/n \simeq -\left(\frac{e}{k_B T_{ph}} + \frac{e}{k_B T_e} + \frac{1}{1+\frac{e\Phi_{SC}}{k_B T_e}}\right)\delta\Phi_{sc} \tag{A.9}$$

Since $T_{ph} < T_e$, $\delta n/n$ is mainly determined by the first term in Eq. (A.9), thus it is roughly proportional to $\delta\Phi_{sc}$ with a proportionality factor set by T_{ph}. A relative variation in plasma density $\delta n/n$ thus induces a voltage $\delta\Phi \simeq -\delta\Phi_{sc}$ detected on all monopole antenna channels which can be roughly expressed as:

$$\delta n/n \simeq \frac{1}{T_{ph}[eV]}\delta\Phi[Volt] \tag{A.10}$$

that can be verified numerically using typical solar wind parameters. Numerical results of Eq. (A.9) (black line), and Eq. (A.10) (red line) are shown in Fig. A.2. The variation of the spacecraft potential induced by density fluctuations does not depend much on the plasma density and the electron temperature (two first panels), but mainly depends on the photoelectron temperature (third panel). [1]

---

[1] The approximation (red value) only underestimates the actual solution Eq. (A.9) by about 20%. It is thus not strictly necessary to know the actual value of the spacecraft potential Φ_{sc}, but only its variations, to have a good estimation of the associated density fluctuations.

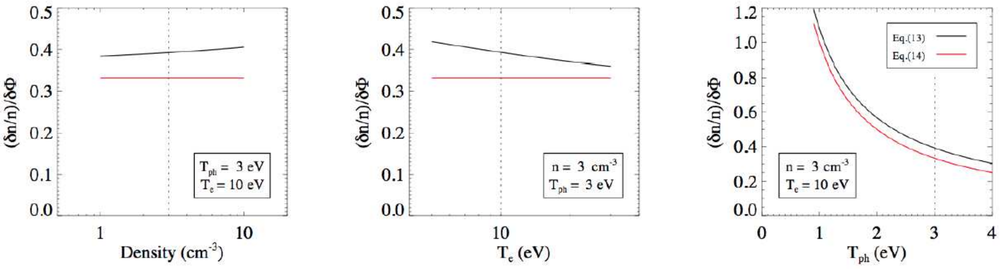

Figure A.2: Ratio of density fluctuations to spacecraft potential variations $(-(\delta n = n)/\delta\Phi)$ in function of plasma density, electron temperature and photoelectron temperature. Both the full expression Eq. (A.9), in black, and the approximation Eq. (A.10), in red, are shown. The vertical dotted lines show typical solar wind parameters, in the third panel it shows the photoelectron temperature associated with the STEREO spacecraft $T_{ph} \simeq 3$ eV.

APPENDIX B

A simple Van der Pol model

The waveforms observed in 2.4.2 should be different manifestations of ion-bulk waves, excited by a plasma instability as results from numerical simulations (78; 79). Following (88), a Van der Pol equation can be obtained from the two–fluid model of plasma in cartesian geometry, which can reproduce the observed waveforms. The electron equation of motion, neglecting the $\mathbf{v}_e \times \mathbf{B}$ term, is given by

$$m\frac{d\mathbf{v}_e}{dt} = -e\nabla\phi + \frac{T_e}{n}\nabla n \tag{B.1}$$

where $\mathbf{v}_e$ is the electron velocity, T_e the electron temperature, m the electron mass and $n = n_i + n_e$ the total plasma density. Assuming spatial variations of the form $\exp(ik_x x)$, where k_x is the axial wavenumber associated to disturbances which generate the burst, and introducing the density fluctuations through $n = n_0 + \delta n(x,t)$, where n_0 is a steady state average, in the low frequency approxiamtion neglecting electron inertia density fluctuations are proportional to potential fluctuations $\delta n \simeq (en_0/T_e)\delta\phi$. The dissipationless ion equation of motion, by ignoring pressure gradient term due to a strong temperature anisotropy, is given by

$$M\frac{d\mathbf{v}_i}{dt} = -e\nabla\phi \tag{B.2}$$

where M is the ion mass. The evolution equation for density is modeled through

$$\frac{\partial n}{\partial t} + \nabla\cdot(n\mathbf{v}_i) = S \tag{B.3}$$

where S is a source term due to the presence of fluctuations locally created by electron heating effects (88). By eliminating the velocities, and using the relation between plasma density and potential, we obtain a differential equation which describes the time behavior of the density

$$\frac{d^2n}{dt^2} - \left(\frac{dS}{dn}\right)\frac{dn}{dt} + \omega_0^2 n = 0 \tag{B.4}$$

where $\omega_0 = k_x c_s$ is the ion-sound frequency and $c_s = (T_e/M)^{1/2}$ is the ion sound velocity. The same equation can be derived for the electrical potential ϕ. From thermodynamics arguments it can be shown (88) that the function S is described as a power of density fluctuations $S = \alpha n - \beta n^2 - \gamma n^3 - \ldots$. Under the hypothesis that $\omega_0 \gg \alpha, \beta n$ and γn^2, equation (Eq. (B.4) reduces to a Van der Pol equation

(85). By adding an external forcing term oscillating at a frequency ω we obtain the forced equation in dimensionless form

$$\ddot{x} - \epsilon(1 - \xi x - \zeta x^2)\dot{x} + x = \Gamma \cos(\Omega\tau) \tag{B.5}$$

which will be used for numerical simulations. Here $\Omega = \omega/\omega_0$ is the ration between the external frequency and the internal frequency, ϵ is the ratio between the growth rate of perturbations and the nonlinear damping coefficient while $\tau = \omega_0 t$ and dots indicate derivative with respect to τ. In the following we will use the classical case where $\xi = 0$ and $\zeta = 1$. The Van der Pol equation, which describes a system with a noninear damping, has been widely used in plasmas. For example the equation describes the nonlinear mode-mode coupling mechanism through which an ion-sound plasma instability should saturate (87; 88), the feedback stabilization of a drift-type instability (89), the saturation of unstable modes in a beam-plasma system (91), mode loking and frequency pulling in a Q machines caused by fluctuations of a plasma column during the current-driven, ion acoustic instability in a collisionless plasma (90), and as a nonlinear mechanism describing the transition to turbulence in a bounded plasma characterized by weakly unstable modes, where the various modes are represented by an ensemble of Van-der-Pol oscillators (92). For a fixed value of Γ and ϵ, the dynamics is drived by the external frequency ω. As $\omega \ll \omega_0$, no interaction between oscillations takes place and both frequencies appears in the spectrum. On the contrary, when ω increases and $\omega = \omega_1 < \omega_0$, the internal frequency is suppressed by the external oscillation and a single frequency ω appears in the spectrum. When ω is further increased and $\omega = \omega_2 > \omega_0$, the internal frequency ω_0 reappers in the spectrum. The interval $\Delta\omega = \omega_2 - \omega_1$ is called the synchronization region because the oscillation syncronizes at a given frequency, while close to both ω_1 and ω_2 periodic pulling is observed. Solutions of Eq.B.5 are obtained as oscillations where both amplitude and phases are modulated in time, which can explain the modulations observed in space plasma. Numerical experiments have been carried out by keeping fixed all parameters but Ω in Eq. (B.5) to show qualitative agreements between the simple model and the observational results. In Fig. B.1 I show the results obtained for three different values of Ω and $\Gamma = 1.0$, $\epsilon = 0.5$, $\xi = 0.01$ and $\zeta = 0.1$ (changing the values of these fixed parameters don't change qualitatively the results). Looking at the different kind of behavior, it can be recognized the frequency synchronization, both frequencies outside the synchronization region and a kind of periodic pulling that look very similar what observed in STEREO/Waves data and hybrid–Vlasov simulations data (Fig. 2.12 and Fig. 2.15).

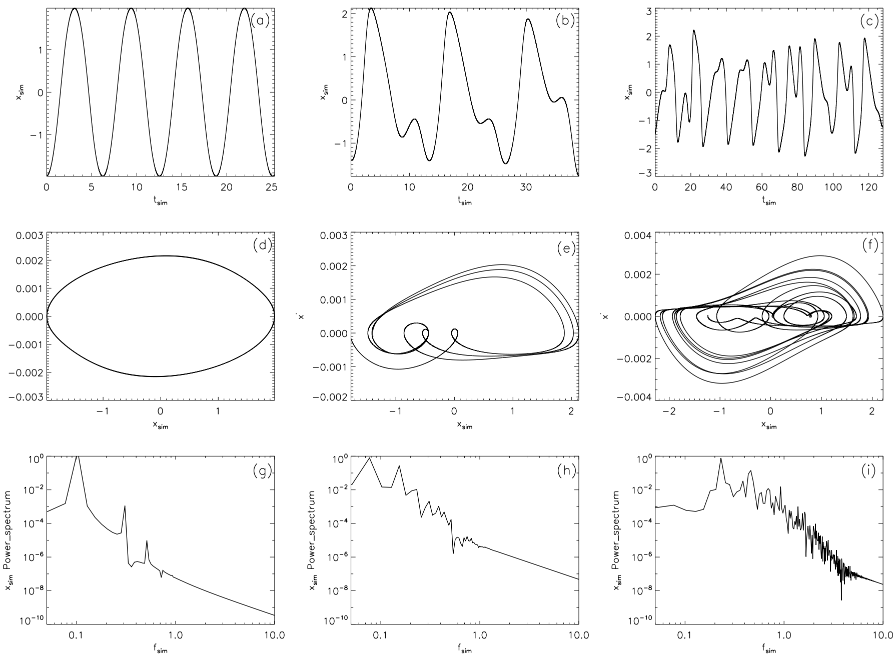

Figure B.1: Examples of oscillation regimes (upper panels) obtained from simulations of the Van der Pol equation, with their relative phase space (middle panels) and power spectrum (lower panels). The parameters used for the case a) are: $\epsilon = 0.5$, $\Gamma = 1.0$ and $\Omega = 3.0$, for case b) are: $\epsilon = 0.5$, $\Gamma = 1.0$ and $\Omega = 0.45$, while for the case c) are: $\epsilon = 0.5$, $\Gamma = 1.0$ and $\Omega = 0.45$.

Bibliography

[1] Tsinober A., Springer Dordrecht Heidelberg London New York, (2009)

[2] Davidson L., Chalmers University of Technology, Göteborg, Sweden, (2011).

[3] Krall N. A., and Trivelpiece A. W., Principles of Plasma Physics (San Francisco, CA: San Francisco Press), (1986).

[4] McDonough J. M., Departments of Mechanical Engineering and Mathematics University of Kentucky, (2004).

[5] Reynolds O., Philos. Trans. R. Soc. London,**174**, pg. 935, (1883)

[6] Ruelle D., Takens F., Commun. Math. Phys., **20**, pg. 167, (1971).

[7] Landau L.D., Lifshitz E.M., Editions MIR, Moscow, U.S.S.R, (1971).

[8] Lorenz E.N., J. Atmos. Sci., **20**, pg. 130, (1963).

[9] Bohr T., Jensen M.H., Paladin G., Vulpiani A., Cambridge University Press, Cambridge, U.K., (1998).

[10] Gollub J.P., and Swinney H.L., Phys. Rev. Lett., **35**, pg. 927, (1975).

[11] Frisch U., Cambridge University Press, Cambridge, U.K.; New York, U.S.A, (1995).

[12] Kolmogorov A.N., Dokl. Akad. Nauk. SSSR, **30**, pg. 301, (1941). Reprinted in Proc. R. Soc. London, Ser. A **434**, pg. 9âĂŞ13, (1991).

[13] Callen J.D., Fundamentals of Plasma Physics, (2003).

[14] Hiwatari R., Okano K., Asaoka Y., Shinya K., Ogawa Y., Nuclear Fusion, **45**, pg. 96, (2005).

[15] Wagner F. et al., Phys. Rev. Lett. 53, 1453 (1984)

[16] Batchelor G. K., Quart. Appl. Math., **6**, pg. 97, (1948).

[17] Burgers J. M., Adv. Appl. Mech., **1**, pg. 171, (1948).

[18] Heisenberg W., Proc. Roy. Soc. A, **195**, pg. 402, (1948).

[19] von Kàrmàn T., Proc. Nat. Acad. Sci., Wash., **34**, pg. 530, (1948).

[20] Yaglom A. M., Izv. Akad. Nauk. SSSR Ser. Geogr. i Geofiz., **12**, pg. 501, (1948).

[21] Corrsin S., J. Aero. Sci., **16**, pg. 757, (1949).

[22] Obukhov A. M., Doklady. Akad. Nauk. SSSR, **67**, pg. 643, (1949).

[23] Kraichnan R.H., Phys. Fluids, **8**, pg. 1385, (1965).

[24] Biskamp D., Cambridge University Press, Cambridge, U.K.; New York, U.S.A, (1993).

[25] Biskamp D., Cambridge University Press, Cambridge, U.K.; New York, U.S.A, (2003).

[26] Schekochihin A.A., and Cowley S.C., Springer, Dordrecht, The Netherlands, pg. 85, (2007).

[27] Tu C.Y., and Marsch E., Space Sci. Rev., **73**, (1995a).

[28] Tu C.Y., and Marsch E., J. Geophys. Res., **100**, pg. 12323, (1995b).

[29] Politano H., and Pouquet A., Phys. Rev. E , **52**, pg. 636, (1995).

[30] Elsässer, W.M., Phys. Rev., **79**, pg. 183, (1950).

[31] Kaiser M.L., Advances in Space Research **36**, pg. 1483 (2005).

[32] Kaiser M.L., Kucera T.A., Davila J.M., Cyr O.C., Guhathakurta M., and Christian E., Space Science Reviews, **198** (2007).

[33] Driesman A., Hynes S., and Cancro G., Space Science Reviews, **136**, pg. 17, (2008).

[34] Howard R.A. *et al.*, Space Science Reviews **136**, pg. 67, (2008).

[35] Bale S.D. *et al.*, Space Science Reviews, **136** , pg. 529, (2008).

[36] Bougeret J.L. *et al.*, Space Science Reviews, **136** , pg. 487, (2008).

[37] Luhmann J.G. *et al.*, Space Science Reviews, **136** , pg. 117, (2008).

[38] M. H. Acuña, Curtis D., Scheifele J. L., Russell C. T., Schroeder P., Szabo A., and Luhmann J. G., Space Science Reviews, **136**, pg. 208, (2007).

[39] Galvin A.B. *et al.*, Space Science Reviews, **136** , pg. 437, (2008).

[40] Kellogg P. J., Bale S.D., Mozer F.S., Horbury T.S., Reme H., Astrophys. J., **645**, pg. 704, (2006).

[41] Kellogg P. J., Goetz K., Monson S.J., Bale S.D., Reiner M.J., and Maksimovic M., J. Geophys. Res, **114**, (2009)

[42] Zakharov, V. E., Soviet Journal of Experimental and Theoretical Physics, **35** , pg. 908, (1972).

[43] Zakharov, V. E., S. L. Musher, and A. M. Rubenchik, **129** , pg. 285, (1985).

[44] Robinson, P. A., Rev. Mod. Phys., **69**, 2, (1997).

[45] Henri P., Meyer–Vernet N., Briand C., and Donato S., Phys. Plasma, **18**, 082308 (2011).

[46] Pedersen A., Annales Geophysicae, **13**, 118 (1995).

[47] Pedersen A., Lybekk P.B., Andrè M., Eriksson A., Masson A., Mozer F. S., Lindqvist P., Décréau P.M.E., Dandouras I., Sauvaud J., Fazakerley A., Taylor M., Paschmann G., Svenes K.R., Torkar K., and Whipple E., J. Geophys. Res., **113**, pg. 7, (2008)

[48] Escoubet C. P., Pedersen A., Schmidt R., and Lindqvist P.A., J. Geophys. Res., **102**, pg. 17595 (1997).

[49] Scudder J. D., Cao X., and Mozer F.S., J. Geophys. Res. **105**, pg. 21281 (2000).

[50] Grard R. J. L., J. Geophys Res., **78**, pg. 2885, (1973).

[51] Salem C., Bosqued J.M., Larson D.E., Mangeney A., Maksimovic M., Perche C., Lin R.P., Bougeret J.L. *et al.*, J. Geophys. Res., **106**, pg. 701, (2001).

[52] Meyer–Vernet N., Cambridge University Press, (2007).

[53] Meyer–Vernet N. and Perche C., J. Geophys. Res., **94**, pg. 2405, (1989).

[54] Matthaeus W. H., Oughton S., Pontius D. H., and Zhou Y., J. Geophys. Res., **99**, pg. 19267, (1994)

[55] Goldstein M. L., Roberts D. A., and Fitch C. A., J. Geophys. Res., **99**, pg. 11519, (1994).

[56] Goldstein M. L., Roberts D. A., and Matthaeus W. H. , ARA&A, **33**, pg. 283, 1995

[57] Smith C. W., Matthaeus W. H., and Ness N. F., in Proc. 21st Int. Cosmic Ray Conf., ed. R J Protheroe (Adeliade), pg. 280, (1990).

[58] Leamon R. J., Smith C. W., and Ness N. F., Matthaeus W.H., and Wong, H.K.J. Geophys. Res., **103**, pg. 4775, (1998).

[59] Bale S. D., Kellogg P. J., Mozer F. S., Horbury T. S., and Reme H., Phys. Rev. Lett., **94**, pg. 215002, (2005).

[60] Marsch E., Rev. Mod. Astron., **4**, pg. 145, (1991).

[61] Richardson J. D., Paularena K. I., Lazarus A. J., and Belcher J. W., Geophys. Res. Lett., **22**, pg. 1469, (1995).

[62] Dmitruk P., Matthaeus W. H., Milano L. J., Oughton S., Zank G. P., and Mullan D. J., Astrophys. J., **575**, pg. 57, (2002).

[63] Dmitruk, P., and Matthaeus, W. H. 2003, ApJ, **597**, pg. 1097, (2003).

[64] Vasquez B. J., Smith C. W., Hamilton K., McBride B. T., and Leamon R. J., J. Geophys. Res., **112**, pg. A07101, (2007).

[65] Sorriso–Valvo L., Marino R., Carbone V., Noullez A., Lepreti F., Veltri P., Bruno R., Bavassano B., Pietropaolo E., Phys. Rev. Lett., **99**, pg. 115001 (2007).

[66] McBride B.T., Smith C.W., and Forman M.A., Astrophys. J., **679**, pg. 1644, (2008).

[67] Marino R., Sorriso-Valvo L., Carbone V., Noullez A., Bruno R., and Bavassano B., Astrophys. J., **677**, pg. L71, (2008).

[68] Carbone V., Marino R., Sorriso-Valvo L., Noullez A., and Bruno R., Phys. Rev. Lett., **103**, pg. 061102, (2009).

[69] Gurnett D. A., and Frank L. A., J. Geophys. Res., **83**, pg. 58, (1978).

[70] Gurnett D. A., Neubauer F. M., and Schwenn R., J. Geophys. Res., **84**, pg. 541, (1979).

[71] Mangeney A., Salem C., Lacombe C., Bougeret J.L., Perche C., Manning R., Kellogg P.J., Goetz K., Monson S.J., and Bosqued J.M., Ann. Geophys., **17**, pg. 307, (1999).

[72] Howes G.G., Dorland W., Cowley S.C., Hammett G.W., Quataert E., Schekochihin A.A., and Tatsuno T., Phys. Rev. Lett., **100**, pg. 065004, (2008)

[73] Sahraoui F., Goldstein M.L., Robert P., and Khotyaintsev Y.âĂĽV., Phys. Rev. Lett., **102**, pg. 231102, (2009).

[74] Alexandrova O., Saur J., Lacombe C., Mangeney A., Mitchell J., Schwartz S.J., and Robert P., Phys. Rev. Lett., 103, pg. 165003, (2009).

[75] Perri S., Carbone V., Veltri P., Astrophys. J., **725**, pg. L52, (2010)

[76] Carbone V., Perri S., Yordanova E., Veltri P., Bruno R., Khotyaintsev Y., and AndrÃľ M., Phys. Rev. Lett., **104**, pg. 181101, (2010).

[77] Araneda J.A., Maneva Y., and Marsch E., Phys. Rev. Lett., **102**, pg. 175001, (2009).

[78] Valentini F., Travnicek P., Califano F., Hellinger P., and Mangeney A., J.Comput. Phys., **225**, 753, (2007).

[79] Valentini F., Veltri P., Califano F., and Mangeney A., Phys. Rev. Lett., **101**, pg. 025006, (2008).

[80] Valentini F., and Veltri P., Phys. Rev. Lett., **102**, pg. 225001, (2009).

[81] Valentini F., Califano F., and Veltri P. 2010, Phys. Rev. Lett., **104**, pg. 205002, (2010).

[82] Valentini F., Califano F., Perrone D., Pegoraro F., and Veltri P., Phys. Rev. Lett., **106**, pg. 165002, (2011).

[83] Valentini F., Perrone D., and Veltri P., Astrophys. J., **739**, pg. 54, (2011).

[84] Carbone V. , Donato S., Valentini F., Vecchio A., Veltri P., (2011) *in press.*

[85] Van der Pol B., Phil. Mag., **43**, pg. 700, (1922).

[86] Kennel C.F., and Engelmann F., Phys. Fluids, **9**, pg. 2377, (1966).

[87] Keen B.E., and Fletcher W.H.W., Phys. Rev. Lett., **23**, pg. 760, (1969).

[88] Keen B.E., and Fletcher W.H.W., J. Phys. D: Appl. Phys., **3**, pg. 1868, (1970).

[89] Keen B.E., Phys. Rev. Lett., **24**, pg. 259, (1970).

[90] Keen B.E., and Fletcher W.H.W., J. Phys. A: Gen. Phys., **5**, pg. 152, (1972).

[91] DeNeef P., and Lashinski H., Phys. Rev. Lett., **31**, pg. 1939, (1973).

[92] Abrams R.H. Jr., Yadlowsky E.S., and Lashinsky H., Phys. Rev. Lett., **22**, pg. 275, (1969).

[93] Matthaeus W. H., Servidio S., and Dmitruk P., Phys. Rev. Lett., **101**, pg. 149501, (2008).

[94] Servidio S., Matthaeus W.H., and Carbone V., Phys. Plasmas, **15**, pg. 042314, (2008).

[95] Sonnerup B. U. O., J. Plasma Phys., **4**, pg. 161, (1970).

[96] Sonnerup B. U. O. and Cahill L. J., J. Geophys. Res., **72**, pg. 171, (1981).

[97] Vasyliunas V. M., Geophys. Space Phys., **13**, pg. 303, (1975).

[98] Moffatt, H. K., Cambridge U. Press, Cambridge, England, (1978).

[99] Parker E. N., Astrophys. J., **62**, pg. 509, (1983)

[100] Gosling J. T., Skoug R. M., McComas D. J. and Smith C. W.. J. Geophys. Res., **110**, pg. A01107, (2005).

[101] Gosling J. T. and Szabo A., J. Geophys. Res., **113**, pg. A10103, (2008).

[102] Phan T. D., Gosling J. T., Davis M. S., Skoug R. M., Øieroset M., Lin R. P., Lepping R. P., McComas D. J., Smith C. W., Reme H. and Balogh A., Nature, **439**, pg. 175, (2006)

[103] Retinò A., Sundkvist D., Vaivads A., Mozer F., André, M., and Owen C. J., Nature Phys., **3**, pg. 235, (2007)

[104] Sundkvist D., Retinó A., Vaivads A., and Bale S. D., Phys. Rev. Lett., **99**, pg. 025004, (2007).

[105] Taylor J. B., Rev. Mod. Phys., **58**, pg. 741, (1986).

[106] Yamada M., Phys. Plasmas, **14**, pg. 058102, (2007).

[107] Yamada M., Rev. Mod. Phys., **82**, pg. 603, (2010).

[108] Brown M. R., Cothran C. D., and Fung J., Phys. Plasmas, **13**, pg. 056503, (2006).

[109] Bruno R. and Carbone V., Living Rev. Solar Phys., **2**, (2005).

[110] Giovanelli R., Nature, **158**, pg. 81, (1946).

[111] Hoyle, F., Cambridge University Press, Cambridge, (1949).

[112] Cowling T. G., University Chicago Press, Chicago, (1953).

[113] Dungey J. W., Phyl. Mag., **44**, pg. 725, (1953).

[114] Sweet P. A., Cambridge University Press, New York, (1958).

[115] Parker E. N., J. Geophys. Res., **62**, pg. 509, (1957).

[116] Petschek H. E., Physics of Solar Flares, ed. W.N. Hess, NASA, (1964)

[117] Priest E. and Forbes T., Cambridge University Press, (2000).

[118] Zweibel E. G., and Yamada M., Annu. Rev. Astron. Astrophys., pg. 291, (2009)

[119] Servidio S., Matthaeus W. H., and Dmitruk P., Phys. Rev. Lett., **100**, pg. 095005, (2008).

[120] Servidio S., Matthaeus W. H., Shay M. A., Cassak P. A., and Dmitruk, P., Phys. Rev. Lett., **102**, pg. 115003, (2009.).

[121] Servidio S., Matthaeus W. H., Shay M. A., Dmitruk P., Cassak P. A., and Wan M., Phys. Plasmas, **17**, pg. 032315, (2010).

[122] Servidio S., Dmitruk P., Greco A., Wan M., Donato S., Cassak P.A., Shay M. A., Carbone V., and Matthaeus W.H., Nonlin. Proc. Geophys., **18**, pg.675, (2011).

[123] Matthaeus W. H., and Montgomery D., Ann. N.Y. Acad. Sci., **357**, pg. 203 (1980).

[124] Matthaeus W. H. and Lamkin S. L., Phys. Fluids, **29**, pg. 2513, (1986).

[125] Cassak P. A., Drake J. F., and Eckhardt B., Phys. Rev. Lett., **98**, pg. 215001, (2007).

[126] Hughes, W., Cambridge University Press, London, (1995)

[127] Ghosh S., Hossain M., and Matthaeus W. H., Comput. Phys. Commun., **74**, pg. 18, (1993).

[128] Wan M., S. Oughton, Servidio S. and Matthaeus W. H., Phys. Plasmas, **16**, pg. 080703 (2009).

[129] Wan M., Oughton S., Servidio S., and Matthaeus W. H., Phys. Plasmas, **17**, pg. 082308, (2010).

[130] Sorriso-Valvo L., Carbone V., Veltri P., Consolini G., and Bruno R., Geoph. Res. Lett., **26**, (1999).

[131] Mininni P. D. and Pouquet A., Phys. Rev. E, **80**, pg. 025401, (2009).

[132] Smith D., Ghosh S., Dmitruk P., and Matthaeus W. H., Geophys. Res.Lett., **31**, pg. L02805, (2004).

[133] Dorelli J. C., and Birn J., J. Geophys. Res. **108**, pg. 1133, (2003).

[134] Servidio S., Carbone V., Primavera L., Veltri P., and Stasiewicz K., Planet. Space Sci., **55**, pg. 2239 (2007).

[135] Galtier S., and Buchlin E., Astrophys. J., **656**, pg. 560 (2007).

[136] Dmitruk P., and Matthaeus W. H., Phys. Plasmas, **13**, pg. 042307, (2006).

[137] Mininni P. D., Alexakis A., and Pouquet A., J. Plasma Phys, **73**, pg. 377, (2007).

[138] Alexandrova O., Carbone V., Veltri P., and Sorriso-Valvo L., Planet. Space Sci., **55**, pg. 2224, (2007).

[139] Matthaeus W. H., Dmitruk P., Smith D., Ghosh S., and Oughton S., Geophys. Res. Lett., **30**, pg. 2104, (2003).

[140] Balbus S.A., and Terquem C., Astrophys. J., **552**, pg. 235, (2001).

[141] Goldreich P., and Reisenegger A., Astrophys. J., **395**, pg. 250, (1992).

[142] Bhattacharjee A., and Ng C.S., Astrophys. J., **548**, pg. 318, (2001).

[143] Shay M. A., Drake J. F., Denton, R. E., and Biskamp D., J. Geophys. Res., **103**, pg. 9165 (1998).

[144] Birn J., Drake J.F., Shay M.A., Rogers B.N., Denton R.E., Hesse M., Kuznetsova M., Ma Z.W., Bhattacharjee A., Otto A., and Prichett P.L., J. Geophys. Res., **106**, pg. 3715, (2001).

[145] Ma Z. W., and Bhattacharjee A., J. Geophys. Res., **106**, pg. 3773, (2001).

[146] Smith D., Ghosh S., Dmitruk P., Matthaeus W. H., Geophys. Res. Lett., **31**, pg. L02805 (2004).

[147] Sonnerup B. U. O., in *Solar System Plasma Physics*, ed. by E. N. Parker, C. F. Kennel and L. J. Lanzerotti, North-Holland, pg. 47, (1979).

[148] Ren Y., Yamada M., Gerhardt S., Ji H., Kulsrud R., and Kuritsyn A., Phys. Rev. Lett., **95**, pg. 055003 (2005).

[149] Matthaeus W. H., Cothran C. D., Landreman M., and Brown M. R., Geophys. Res. Lett., **32**, pg. L23104 (2005).

[150] Cassak P. A., and Shay M. A., Phys. Plasmas, **14**, pg. 102114, (2007).

[151] Mozer F. S., and Hull A., Phys. Plasmas, **17**, pg. 102906, (2010).

[152] Mozer F. S., and Pritchett P. L., Geophys. Res. Lett., **36**, pg. L07102, (2009).

[153] Pritchett P. L., and Mozer F. S., J. Geophys. Res., **114**, pg. A11210, (2009).

[154] Orszag S.A., Fluid Dynamics, edited by R. Ballian and J.-L. Puebe, Gordon & Breach, N.Y., **235**, (1977).

[155] Carbone V., Veltri P., and Mageney A., Phys. Fluids A, **2**, pg. 1487, (1990).

[156] Gary S. P. and Borovsky J. E., J. Geophys. Res. **109**, pg. A06105 (2004).